CHARACTERIZATION AND CONTROL OF THE NONLINEAR OPTICAL PROPERTIES OF DENDRITIC SILVER NANOPARTICLE CLUSTERS

By

Jess M. Gunn

A DISSERTATION

Submitted to
Michigan State University
in partial fulfillment of the requirements
for the degree of

DOCTOR OF PHILOSOPHY

Chemistry

2011

ABSTRACT

CHARACTERIZATION AND CONTROL OF THE NONLINEAR OPTICAL PROPERTIES OF DENDRITIC SILVER NANOPARTICLE CLUSTERS

By

Jess M. Gunn

In this dissertation, the properties of the energy transport in thin films of silver nanoparticles on dielectric surfaces are explored. Specifically, this dissertation will present experiments in which an ultrafast laser (~ 13 fs) centered at 800 nm is focused at normal incidence on a thin film of polydisperse silver nanoparticles on a quartz substrate. Upon excitation, discrete regions of polarized emission are observed as far as 100 μm from the focal spot. The intensity of these regions of emission can be controlled by the polarization and spectral phase of the laser used for excitation.

Studies into the properties of emission show that the emission is a two-photon induced luminescence, enhanced by localization of the electric field by the silver nanoparticles. The spatial distribution of the nonlinear photoluminescence is found to have characteristics very distinct from that of normal scatter.

Further studies suggest that the excitation pulse propagates to the different remote regions by means of surface plasmon polariton (SPP) propagation. As the SPP propagates, it accumulates different amounts of quadratic and cubic dispersion depending on the path taken, explaining the dependence on spectral phase. The quadratic and cubic dispersion for a number of such pathways is measured, and evidence of negative dispersion is observed. Photoluminescence is observed at

locations where constructive interference and a localized resonance occurs, tens of micrometers from the incident laser pulse.

The results presented in this dissertation regarding the nature and control of energy transport has great implications in the field of “plasmonics,” which seeks to bridge the realms of electronics and photonics with specially designed waveguides. Such waveguides, which could potentially support both plasmon and electrical signals have been designed and experimentally tested by several groups, and work has been done to design nanoscale structures that act as mirrors and beamsplitters for SPPs. However, these groups continue to face reduced propagation lengths, restricting propagation to a few tens of micrometers. The approach presented here, in contrast, shows propagation and control over a 100 μm range.

In memory of Jan Gunn, who taught us that
"Girls can do anything."

ACKNOWLEDGMENTS

During my studies at Michigan State University, there have been many people who have been instrumental in helping me through this process, all of whom I am grateful for.

I first extend my thanks to my committee members, both past and present, including Professors Gary Blanchard, Robert Cukier, Jim McCusker and Chong-Yu Ruan. I also extend my thanks to members of the Dantus group, particularly Vadim Lozovoy for his help with theoretical issues, and Mindi Ogden (nee Ewald) and Scott High, two undergraduates who worked with me for more than a year each, and performed some of the experiments presented here.

I am grateful to Professors Virginia Ayres and Martin Crimp for acquisition of AFM and SEM/TEM images, respectively, and to CRi for loan of the SpecVis, which permitted the acquisition of color images.

I am indebted to my family, and to all of my friends and colleagues at Michigan State, Creighton University, and elsewhere, who cheered me on and encouraged me through the rough times, at times believing in me more than I believed in myself.

Most of all, I am grateful to Professor Marcos Dantus, my advisor. From the beginning, when we first observed the phenomena presented here in the course of what was supposed to be a straightforward background experiment, he allowed me to follow the data and observations where they led, allowing me to explore the beautiful, fascinating world of surface plasmons.

TABLE OF CONTENTS

LIST OF TABLES

LIST OF FIGURES

KEY TO SYMBOLS AND ABBREVIATIONS

α	in MIIPS, a parameter used to define the amplitude of the sine function
α	in the context of metals, the polarizability
AFM	atomic force microscopy
$\boldsymbol{B}$	magnetic induction
CARS	coherent anti-Stokes Raman Scattering
δ	in MIIPS, a parameter used to define the phase of the sine function
$\boldsymbol{D}$	dielectric displacement
ε	dielectric constant
$\boldsymbol{E}$	electric field
EDTA	ethylenediaminetetraaceticacid
EM	electromagnetic
EMCCD	electron-multiplying charge-coupled-device
$\phi(\omega)$	phase modulation (as a function of frequency)
FROG	frequency-resolved-optical-gating
FWHM	full-width-at-half-maximum
GA	genetic algorithm
GDD	group delay dispersion
GVD	group velocity dispersion
$\boldsymbol{H}$	magnetic field
HeNe	helium-neon
k_0	propagation vector
L	propagation length

LSP	localized surface plasmon
LSPR	localized surface plasmon resonance
μ	relative permeability
MIIPS	multiphoton intrapulse interference phase scan
ñ	complex index of refraction
NA	numerical aperture
OD	optical density
PSTM	photon scanning tunneling microscopy
PVA	poly(vinyl alcohol)
QE	quantum efficiency
R-590	rhodamine-590
SE	surface-enhanced
SEM	scanning electron microscopy
SERS	surface-enhanced Raman scattering
SH	second-harmonic
SHG	second-harmonic generation
SLM	spatial light modulator
SNOM	scanning near-field optical microscopy
SPIDER	spectral phase interferometry for direct electric-field reconstruction
SPP	surface plasmon polariton
SSHG	surface second-harmonic generation
STOM	scanning tunneling optical microscopy
TE	transverse electric

TEM	tunneling electron microscopy
Ti:sapphire	titanium:sapphire
TL	transform-limited
TM	transverse magnetic
UV	ultraviolet
ω	frequency

1. INTRODUCTION

1.1. Introduction

This dissertation is, as all are, the culmination of a long journey, one with many twists, turns and unexpected results. My first year was spent with Drs. Bingwei Xu and Johanna dela Cruz in exploring and quantifying the capability of multiphoton intrapulse interference phase scan (MIIPS), a method for measuring and compensating the phase distortions of the ultrafast laser pulses used for excitation in the experiments here, as outlined in Chapter 3 of this dissertation. As that project came to an end, it was time to take on my own, individual, dissertation project – to explore the potential coherent control of single molecule fluorescence. After many false starts and struggles to observe *any* fluorescence with the system that was being assembled, the decision was made to take advantage of the fact that metal nanoparticles have been shown capable of enhancing molecular fluorescence,[1-10] including that of single molecules.[11-13] Therefore, I prepared two films of rhodamine-590 (R590)-doped poly(vinyl alcohol) (PVA). The first was spin-coated directly onto an unadulterated coverslip. The second was spin-coated onto a coverslip onto which a thin layer of silver nanoparticles had been deposited. I then prepared two controls: a blank coverslip, and a coverslip of only the silver nanoparticles. As expected, very weak fluorescence was observed from the unadulterated coverslip with a film of R590-doped PVA, and much, much stronger fluorescence from the film over silver nanoparticles. The plain coverslip showed no fluorescence. All that was left was to show that the silvered coverslip showed no luminescence, either. Instead, the observed emission was as strong as the R590-PVA film over the silver nanoparticles!

This seemingly simple control experiment changed the entire course of my graduate career. What began as a subsequent side project to explore the observed emission, which is identified as two-photon-induced surface-plasmon enhanced fluorescence from the metal nanoparticles, became the topic of this entire dissertation when it was discovered that the emission from the nanoparticle film was not coming only from the focal spot of the laser. Instead, emission was observed remote from the focal spot of the laser, as shown in Figure 1.1. The 80 x 80 μm image shown in this figure was obtained as a single wide-field image of the sample, with no scanning of the laser or the sample. The ultrafast laser used for excitation was focused approximately at the center of the image; this means that there is some mechanism in the system for energy transport over a distances of tens of micrometers. Moreover, it was later found that the intensity of various regions of emission could be controlled, both by the polarization of the excitation beam, and by changing the spectral phase of the ultrafast laser used for excitation.[14] This dissertation, therefore, explores in detail the nature of the energy propagation, via surface plasmons, and its subsequent localization and control.

Figure 1.1. Wide-field image of a silver nanoparticle film collected without scanning either the laser or the sample. The entire image is 80 x 80 μm, and the laser was focused near the center. Rather than observing bright emission at the focus against a black background, discrete regions of luminescence remote from the focal spot are observed, indicating that some mechanism for energy transport exists in the nanoparticle network.

1.2. Plasmonics

The results presented in this dissertation are due to *surface plasmons,* which are the collective oscillations of electrons in a metal. On extended metal surfaces, surface plasmons can exist in the form of surface plasmon polaritons (SPPs), which can be described as a "wave" of electrons in the "sea of electrons" model. On an infinite surface, plasmons can propagate more than 100 μm. More control can be gained over the propagation of the plasmon by reducing the surface width to micrometers or even nanometers;[15-20] however, this reduces the propagation length of the SPP.

The ability to transport the energy over relatively long distances and localize it has great implications in the field of "plasmonics," which seeks to bridge the realms of

electronics and photonics[21] with specially designed waveguides.[22] Such waveguides, which could potentially support both plasmon and electrical signals[23] have been designed and experimentally tested by several groups,[22,24-26] and work has been done to design nanoscale structures that act as mirrors and beamsplitters for SPPs.[26,27] However, these groups continue to face the reduced propagation lengths, restricting propagation to a few tens of micrometers.

In addition to their existence as waves on extended structures, surface plasmons can also be excited on individual nanoparticles, and are a result of the confinement of surface plasmons to the nanoparticles, which, by definition, have dimensions from ten to a few hundred nanometers. If the plasmon is excited by light of an appropriate frequency, a localized surface plasmon resonance (LSPR) can be established, greatly amplifying the electromagnetic (EM) field around the nanoparticles. It is this property that causes the enhancement of fluorescence mentioned previously. It is also this property that leads to the well-studied technique of surface-enhanced-Raman-scattering (SERS),[28-32] including at the single-molecule level.[33-36] In addition, the sensitivity of the LSPR frequency to the index of refraction of the surrounding media has led to applications in high-sensitivity sensing.[37,38]

Similar enhancements to the electromagnetic field are also seen due to localization of the electromagnetic field on rough surfaces in regions called 'hot spots.'[39-44] Extensive theoretical work,[45,46] as well as direct observation of the localization has been made on roughened gold[47,48] and silver[49] films, silver colloid

fractals,[45] and films of nanoparticles near the percolation limit.[50] This localization has been observed directly via photon scanning tunneling microscopy (PSTM)[45,47] scanning near-field optical microscopy (SNOM)[48] and scanning tunneling optical microscopy (STOM)[49] techniques, and indirectly through the measurement of surface second-harmonic generation (SSHG).[51]

Energy can also be localized between nearly-touching pairs[52] or clusters[53] of particles, and has behaviors distinct from that of isolated metal nanoparticles, with shifted resonances and enhanced EM fields in the gap between particles.[54-56] In clusters, this has been shown to enhance both linear[57] and nonlinear[53] optical processes.

1.3. Conclusion

In this dissertation, Chapter 2 will explore the properties of surface plasmons in far more detail than presented here, while Chapter 3, in addition to an in-depth discussion of MIIPS, will present details on the experimental setup for the experiments presented. Chapter 4 will explore the properties of the emission observed, while Chapter 5 explores methods for controlling the emission, via both polarization of the excitation pulse, and the spectral phase of the ultrafast laser used for excitation. This work, when taken together, is the culmination of a fascinating study at the intersection of ultrafast optics and surface plasmons that presents an entirely new approach to the development of plasmonic waveguides capable of sustaining the propagation of plasmons over distances of at least 100 micrometers.

2. SURFACE PLASMONS

The phenomena observed and explored in this dissertation are all related to surface plasmons, which are the collective oscillation of electrons in a metal. This chapter will provide a framework for understanding surface plasmons; more detail can be found in many other references cited throughout this chapter; books by Raether[58] and Maier[59] are of particularly note for their comprehensiveness.

2.1. Types of Surface Plasmons

There are two types of surface plasmons. Surface plasmon polaritons (SPPs) are electron waves propagating at the interface between a metal and a dielectric, while localized surface plasmons (LSPs) are confined excitations of the conduction electrons of metal nanoparticles. Both of these will be explored in more detail in this section.

2.1.1. Surface Plasmon Polaritons (SPPs)

This section will focus on the unique behaviors of surface plasmons as they propagate on smooth surfaces in the form of surface plasmon polaritons. More specifically, it will be looking at a smooth interface between a metal with a uniform dielectic function, $\varepsilon_1(\omega)$, and a non-conducting dielectric with a real dielectric constant, ε_2 as shown in Figure 2.1.

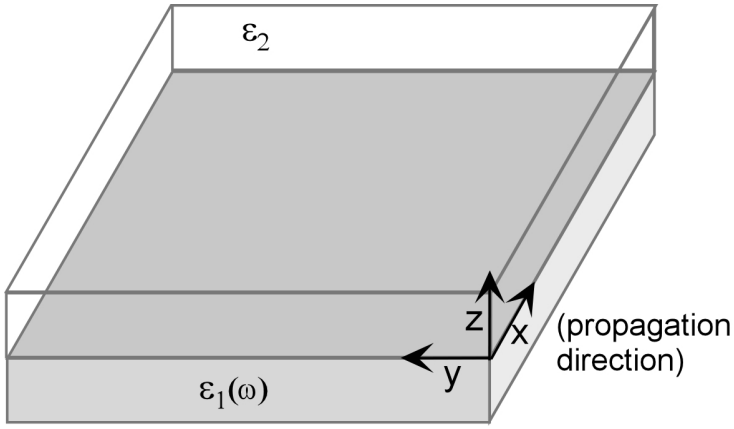

Figure 2.1. The model surface described in this section is a smooth interface between a metal with a dielectric function $\epsilon_1(\omega)$ for z<0 and a non-conducting dielectric with a real dielectric constant ϵ_2, for z>0 where the boundary plane is defined as z=0. Propagation is defined as being in the x-direction.

By using Maxwell's Laws:[59, 60]

$$\nabla \cdot \boldsymbol{D} = \rho_{ext} \tag{2-1}$$

$$\nabla \cdot \boldsymbol{B} = 0 \tag{2-2}$$

$$\nabla \times \boldsymbol{E} = \frac{-\partial \boldsymbol{B}}{\partial t} \tag{2-3}$$

$$\nabla \times \boldsymbol{H} = \boldsymbol{J_{ext}} + \frac{\partial \boldsymbol{D}}{\partial t} \tag{2-4}$$

where $\boldsymbol{D}$ is the dielectric displacement, ρ_{ext} is the external charge density, $\boldsymbol{B}$ is the magnetic induction, $\boldsymbol{E}$ is the electric field, $\boldsymbol{H}$ is the magnetic field, and $\boldsymbol{J_{ext}}$ is the current density, and is equal to 0 for the systems described here, and the following relations for linear, isotropic and nonmagnetic media:

$$\boldsymbol{D} = \epsilon_0 \epsilon(\omega) \boldsymbol{E} \tag{2-5}$$

$$\boldsymbol{B} = \mu_0 \mu(\omega) \boldsymbol{H} \tag{2-6}$$

where ε_0 is the electric permittivity, and μ_0 is the magnetic permeability of a vacuum, ε is the dielectric constant and μ is the relative permeability, and is equal to 1 for non-magnetic substances, and assuming a uniform dielectric profile and harmonic time dependence, the Helmholtz equation can be derived.

$$\nabla^2 \boldsymbol{E} + k_0^2 \epsilon \boldsymbol{E} = \boldsymbol{0} \tag{2-7}$$

Given this equation, where k_0 is the wave vector of the propagating wave in vacuum and is equal to $\tilde{n}(\omega/c)$, where $\tilde{n}$ is the complex index of refraction, and defining $\boldsymbol{E}(x, y, z) = \boldsymbol{E}(z) e^{i k_x x}$, where k_x represents the propagation constant, the wave equation can then be expressed as

$$\frac{\partial^2 \boldsymbol{E}(z)}{\partial z^2} + \left(k_0^2 \epsilon - {k_x}^2\right) \boldsymbol{E} = 0 \tag{2-8}$$

Given the complex nature of $\tilde{n}$, we can show that the intensity of the electromagnetic wave, a surface plasmon, decreases as $e^{-2k_x x}$; the propagation length, L, defined as the distance after which the intensity decreases to a factor of 1/e, can be defined as[58,59]

$$L = \frac{1}{2Im[k_x]} \tag{2-9}$$

To quantify k_x, we look at eqs (2-3) and (2-4). Again assuming a harmonic time dependence ($\frac{\partial}{\partial t} = -i\omega$) , as well as propagation along the x-direction ($\frac{\partial}{\partial x} = -ik_x$),

and homogeneity in the y-direction ($\frac{\boldsymbol{\partial}}{\boldsymbol{\partial y}} = \mathbf{0}$), the following equations relating ***E*** and ***H*** can be derived.

$$\frac{\partial E_y}{\partial z} = -i\omega\mu_0 H_x \tag{2-10}$$

$$\frac{\partial E_x}{\partial z} - ik_x E_z = i\omega\mu_0 H_y \tag{2-11}$$

$$ik_x E_y = i\omega\mu_0 H_z \tag{2-12}$$

$$\frac{\partial H_y}{\partial z} = i\omega\epsilon_0\epsilon E_x \tag{2-13}$$

$$\frac{\partial H_x}{\partial z} - ik_x H_z = -i\omega\epsilon_0\epsilon E_y \tag{2-14}$$

$$ik_x H_y = -i\omega\epsilon_0\epsilon E_z \tag{2-15}$$

If we first assume a transverse magnetic (TM) modes (H_X = 0), the equations simplify to:

$$E_x = -i\frac{1}{\omega\epsilon_0\epsilon}\frac{\partial H_y}{\partial z} \tag{2-16}$$

$$E_z = -\frac{\beta}{\omega\epsilon_0\epsilon}H_y \tag{2-17}$$

$$\frac{\partial^2 H_y}{\partial z^2} + \left(k_0^2\epsilon - {k_x}^2\right)H_y = 0 \tag{2-18}$$

Solving this system for both $z>0$ and $z<0$, and considering the boundary conditions, k_x can be expressed in terms of k_0 and the dielectric constants for both the metal (ε_1) and the surrounding material (ε_2):

$$k_x = k_0 \sqrt{\frac{\epsilon_1 \epsilon_2}{\epsilon_1 + \epsilon_2}} \tag{2-19}$$

A similar analysis for can be performed for transverse electric (TE) modes ($E_x = 0$); however, it turns out that the boundary conditions require $E_y=0$, $H_x=0$ and $H_z=0$. Therefore, SPP modes do not exist for TE polarization.

To further understand the propagation constant, we can look at the Drude model of the dielectric constant of a metal, from which many properties of substances can be explained and derived, which is

$$\epsilon(\omega) = 1 - \frac{\omega_p^2}{\omega^2 + i\gamma\omega} \tag{2-20}$$

where γ is the characteristic collision frequency, on the order of 100 THz, and ω_p is the plasma frequency and is given by

$$\omega_p^2 = \frac{ne^2}{\epsilon_0 m} \tag{2-21}$$

where n is the number density of electrons, while m is the effective optical mass of the electron.

To further examine and use the Drude model for the dielectric constant eq (2-20), it is useful to break it into its real and imaginary parts, and express it in the form $\varepsilon(\omega) = \varepsilon_r(\omega) + i\varepsilon_{im}(\omega)$, where

$$\epsilon_r(\omega)=1-\frac{\omega_p^2\tau^2}{1+\omega^2\tau^2} \tag{2-22}$$

and

$$\epsilon_{im}(\omega)=\frac{\omega_p^2\tau}{\omega(1+\omega^2\tau^2)} \tag{2-23}$$

From eq (2-23), it is clear that the imaginary component of the dielectric function, and therefore the propagation constant, decrease as the frequency of the electromagnetic field increases. As a result, the propagation length is substantially larger for lower frequency electromagnetic pulses. The identity of the metal will also control the propagation length; however, this is harder to quantify, as reported values for ω_p and τ vary widely depending on the source, making reliable approximations of propagation lengths using the Drude model difficult. Generally, however, propagation lengths are much greater in silver than in gold, two of the most common metals used to support surface plasmons.

Quantitatively, values for the complex dielectric constants can be calculated from other measured optical constants. Using data experimentally obtained by Johnson and Christy,[61] and eqs (2-9) and (2-19), propagation lengths can be calculated for various conditions. At 397 nm, the propagation length in silver is calculated to be 1.65 μm. At 632 nm, the propagation length would be about 30 μm. At 821 nm, close to the carrier

frequency of the ultrafast laser used for most experiments in this dissertation, that length is as great as 144 μm. For comparison, the propagation length of surface plasmons in gold are calculated to be 0.18 and 25 μm for 400 and 821 nm, respectively.

2.1.2. Confinement in Strips and Wires

The results presented in Section 2.1.1 assume an effectively infinite surface in the y-direction. By reducing the y-dimension to the order of microns ("stripes") or nanometers ("nanowires"), the direction of SPP propagation can be controlled, as shown in a large body of work.[15-20] A brief note should be made, however, that decreasing the width of the stripe decreases the propagation length of the SPP, as nicely illustrated in a systematic study by Lamprecht et al,[16] which experimentally shows that stripes with widths above 20 μm all had propagation distances approaching 60 μm after excitation with 633 nm light, while 1 μm wide stripes had propagation distances of only a few micrometers. In nanowires, propagation distances as great as 10-15 μm[19,20] have been observed.

Several approaches have been developed to overcome this reduced propagation length, including structured surfaces and modification of the geometries as well as using longer wavelengths of light for excitation. In the case of silver, for example, increasing the excitation wavelength from 633 nm to 785 nm increases the propagation length from 50 to 150 μm.[16] For wires, it has been shown that collections, or bundles, of wires can increase the propagation distance well beyond that of individual wires.[62,63]

2.1.3. Launching Surface Plasmons

SPPs in smooth, thin films cannot be launched by simple irradiation due to momentum mismatch; i.e. $k_X > k$ in air. Therefore, special techniques must be used to launch SPPs in films. One common approach is prism coupling using the Kretschmann configuration, where the film is deposited on the hypotenuse of a prism, and attenuated total internal reflection is used to excite the SPPs. However, a more recent approach[64] shows that high numerical objectives in contact (via index-matching oil) with the glass substrate can overcome this, as the wide angle of the focused beam includes angles greater than the critical angle for total internal reflection. This means that vectors are available for coupling into the system.

This same limitation can also be overcome by rough surfaces and/or individual nanoparticles, where the very shape of the particle or surface allows for the coupling of light in and out of the system. The ease of exciting surface plasmons in nanoparticles, as well as their ability to couple to adjacent structures is due to localized surface plasmon resonance, and is the topic of the next section.

2.2. Localized Surface Plasmons

As discussed in Section 1.2, exciting a metal nanoparticle with light of an appropriate frequency results in a localized surface plasmon resonance, greatly amplifying the electromagnetic (EM) field around the nanoparticles. This section will discuss the theory and implications of this amplification.

2.2.1. Electromagnetic Enhancement

One of the most common applications of surface plasmon resonance is in the enhancement of electromagnetic fields. The electromagnetic enhancement factor, $L(\nu)$ is given by[59]

$$L(\nu) = \frac{|\boldsymbol{E}_{\boldsymbol{loc}}(\nu)|}{|\boldsymbol{E}_0|} \tag{2-24}$$

where $\boldsymbol{E}_{loc}(\nu)$ is the local field amplitude. This electromagnetic enhancement factor has two components, and can be written as $L(\nu)=L_{SP}(\nu)L_{LR,}$ where L_{SP} is the enhancement due to the resonant excitation of LSPs, and L_{LR} is the enhancement due to what is called the lightning-rod effect.[65,66]

L_{LR} is due to the crowding of field lines around sharp metallic features in non-spherical metal nanoparticles, while L_{SP} is proportional to the polarizability, α, of the particle, and is likewise frequency-dependent. Overall, the increase in luminescence, due to both effects, scales as

$$P_{lum} \propto L(\omega_{ex})^2 L(\omega_{em})^2 \tag{2-25}$$

where ω_{ex} and ω_{em} are the frequency of excitation and emission, respectively. In this section, we will focus on understanding the contribution of polarizability to, and therefore the frequency-dependence of, the enhancement factors.

2.2.2. Polarizability

To explore the polarizability, we'll use an initial model of a small spherical nanoparticle with a radius *a* and complex dielectric constant ε_1 in an environment with a constant dielectic constant ε_2.

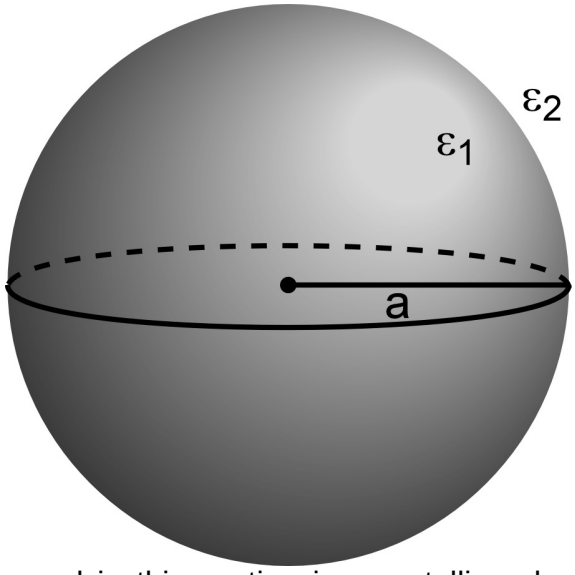

Figure 2.2. The model used in this section is a metallic sphere with a radius *a* and complex dielectric constant ε_1 in an environment with a constant dielectic constant ε_2.

Assuming $a << \lambda$, the polarizability of metal particles can be given by

$$\alpha = 4\pi a^3 \frac{\varepsilon_1(\omega) - \varepsilon_2}{\varepsilon_1(\omega) + 2\varepsilon_2} \tag{2-26}$$

It can be easily seen from this equation that a maximum in polarizability, and therefore in the dipole and electric fields is observed when

$$\omega_0 = Re[\varepsilon_1(\omega)] = -2\varepsilon_2 \tag{2-27}$$

which is known as the Fröhlich condition. For a metal in air, with a real dielectric coefficient given by eq (2-22), $\omega_0 = \omega_p/\sqrt{3}$.

An important implication of eq (2-27) is that the resonance frequency is strongly dependent upon the nature – specifically, the dielectric constant – of the surrounding material. This sensitivity is the source of many of the sensing applications that have been developed using the resonance frequency of a nanoparticle to explore changes in the local dielectric environment, due to, for example, the adsorption of a molecule to the surface.[37,38]

The approach presented so far is the "quasi-static" approach, and assumes that a<<λ. However, while this approach is useful to the first approximation, and in understanding the source of the resonance properties, it fails to adequately describe all experimental results. Most notably, it fails to account for the shift in resonance wavelength that occurs as particle size varies.[31,55,67,68] The most complete theory has been that developed by Mie, and published in 1908. For larger particles, the following expression, an expansion of the first mode of Mie theory, can be used.[69]

$$\alpha_{sphere} = \frac{1 - \left(\frac{1}{10}\right)(\epsilon_1 + \epsilon_2)x^2 + O(x^4)}{\left(\frac{1}{3} + \frac{\epsilon_2}{\epsilon_1 - \epsilon_2}\right) - \frac{1}{30}(\epsilon_1 + 10\epsilon_2)x^2 - i\frac{4}{3}\pi^2\epsilon_2^{3/2}\frac{V}{\lambda_0^3} + O(x^4)}V \quad (2\text{-}28)$$

where $x = \pi a/\lambda_0$.

While not immediately clear, the inclusion of terms that incorporate both ε and x has the effect of red-shifting the resonance frequency as the size of the nanoparticle increases. This makes sense, intuitively, as larger particles have a larger charge separation, which weakens the restoring force and lowers the resonant frequency.

A final experimental observation that is not accounted for, even by the Mie theory presented here, is the behavior of non-spherical particles.[55,67,68,70] For rod-shaped particles, for example, there exists two resonance frequencies: a higher frequency component corresponding to transverse resonance across the width of the rod, and a lower-frequency resonance corresponding to longitudinal resonance along the length of the rod. The excitation of these modes is sensitive to the polarization of the excitation pulse.

2.2.3. Coupling between particles

In addition to coupling energy in and out of smooth surfaces, as referenced in the previous section, the coupling between particles due to localized surface plasmon resonance has been used as an alternate approach to plasmon waveguiding. As early as 1998, it was predicted that such coupling could be exploited to develop waveguides in which particles were spaced an optimal distance apart,[71] such that propagation as far as 900 nm could be achieved.[72] Subsequent theory along the same lines supported this idea, and extended the theory to predict waveguiding around corners and through T-intersections,[73,74] as well as other geometries.[71] In 2003, the first waveguiding by a chain of nanoparticles over 'several hundred nanometers' was observed.[75] Following this, much work was done to refine the theoretical models used, as well as generalize the work to spheroidal nanoparticles.[76-86] Over this time, at least one model was developed that extended the predicted distance of waveguiding to hundreds of micrometers.[82]

2.2.4. Percolation

When samples are prepared in the manner discussed in Chapter 3 of this dissertation, the density of nanoparticles begins to approach the percolation limit. Interestingly, such an extended structure has been shown capable of supporting SPPs,[87,88] enabling the propagation of energy in our samples. The "bumpiness," or roughness, of the sample means that this energy can subsequently be localized, with the potential to manifest in many way, including promoting various surface-enhanced processes, prompting surface-second-harmonic-generation,[51] or even exciting the nanoparticles themselves, resulting in metal fluorescence, as it is concluded happens in the experiments presented in this dissertation.

2.3. Conclusion

This chapter has examined the origin and applications of surface plasmons. Of particular note for this dissertation are the results indicating that SPPs can propagate as far as 100 μm, and that aggregates of nanoparticles can support such SPPs. As well, it is important to note that individual nanoparticles can be used to couple energy in and out of the system, and that the resonances of these nanoparticles are dependent not only on the dielectric environment, but on the size, shape and orientation of the particle. As it will be shown in later chapters, it is the combination of these properties that make the remote observation of emission from a surface of silver nanoparticles possible.

3. EXPERIMENTAL

This chapter will cover all aspects of the experimental setup, from the excitation to detection systems. Much consideration will be given to the unique challenges presented by the use of an ultrafast (~10 fs) laser, including the introduction of spectral phase distortions as the laser propagates through media, and the chosen method for compensation, MIIPS, will be discussed and evaluated in detail. That evaluation, my first project in the Dantus group, was performed with Drs. Johanna dela Cruz and Bingwei Xu.

3.1. Ultrafast lasers

3.1.1. Background

Ultrafast lasers, i.e. lasers with pulse durations on the order of picoseconds (ps, 10^{-12} s) or femtoseconds (fs, 10^{-15} s), are increasingly being used in a wide range of applications, due to the short time duration of the pulses. Commonly, ultrafast lasers are used in time-resolved experiments, as the short time durations allow for exploration of molecular motions. Other applications take advantage of the high peak power associated with ultrashort pulses. For reference, a 100 mW ultrafast laser with a repetition rate of 87 MHz results in peak powers of 11.5 kW for a 100 fs pulse, and 115 kW for a 10 fs pulse. These high peak powers open the doors to nonlinear optics, with applications in fields ranging from biological imaging to high-harmonic generation. Other experimental work exploits the fact that femtosecond lasers are non-monochromatic. A 30 fs pulse with a carrier frequency of 800 nm will have a ~30 nm bandwidth, while a 10 fs pulse with a carrier frequency of 800 nm will have ~100 nm

bandwidth. As will be discussed more in the pulse shaping section, this provides avenues for selective excitation.

3.1.2. Phase

One of the critical aspects to optimally using ultrashort pulse lasers is controlling spectral-phase distortions introduced by the interaction of the pulses with an optical surface such as a dielectric mirror, or their transmission through a lens, an optical fiber, or a microscope objective. These distortions, which stem from the frequency-dependent index of refraction of materials, have a significant effect on the nonlinear properties of the pulse, leading to increased pulse duration, loss of peak intensity and, in some cases, loss of information. Acquired dispersion can not only result in discrepancies in laser properties between setups, but different lasers, with slightly different properties, traveling through the same setup may also end up with different properties.

The phase modulation as a function of frequency, $\phi(\omega)$, produced by all physical processes is typically a continuous function, and can therefore be written as a Taylor expansion:

$$\phi(\omega) = (\omega_0)\phi + (\omega - \omega_0)\phi' + \left(\frac{1}{2}\right)(\omega - \omega_0)^2\phi'' + \left(\frac{1}{6}\right)(\omega - \omega_0)^3\phi''' + \ ... \tag{3-1}$$

where ω_0 is the carrier frequency of the pulse.

The linear term, $(\omega - \omega_0)\phi'$, serves only to shift the pulse in time; it does not affect the components of the pulse relative to one another. The quadratic term,

$\left(\frac{1}{2}\right)(\omega-\omega_0)^2\phi''$ contributes to broadening of the pulse, and is known as group delay dispersion (GDD). The shorter the initial pulses, the more significant the broadening becomes, as shown in Figure 3.1. A substantial amount of GDD can be introduced by the optical setup, as quartz has a group velocity dispersion (GVD; a measure of GDD per unit length) of 36 fs^2/mm. In the experiments that form the basis for the results presented in this dissertation, the high-numerical aperture objective alone contains up to an inch of glass, contributing nearly 1000 fs^2. For a 10 fs pulse, such as used in the experiments presented here, this results in a pulse more than 100 fs in duration, clearly having the potential to severely hinder the optimal use of the laser. Finally, the cubic term, $\left(\frac{1}{6}\right)(\omega-\omega_0)^3\phi'''$, results in pulse trains. These, and even higher order-dispersions, lead to unwanted and/or inexplicable results when nonlinear processes are studied. Moreover, they lead to a lack of reproducibility between experimental systems. It is therefore necessary to measure and then compensate for these dispersions in order to both understand what is happening in a measured nonlinear process as well as to enable reproducibility of experimental results.

Compensation of dispersion becomes even more critical when pulse shaping, or controlling the time-domain characteristics of a pulse, is a part of the experiment. Without a defined and attainable “zero-phase,” or transform-limited (TL) pulse, the applied phase is meaningless, as it will be applied over unknown and potentially variable values. The actual spectral phase of the pulse will therefore be unknown and interpretation of results nearly impossible.

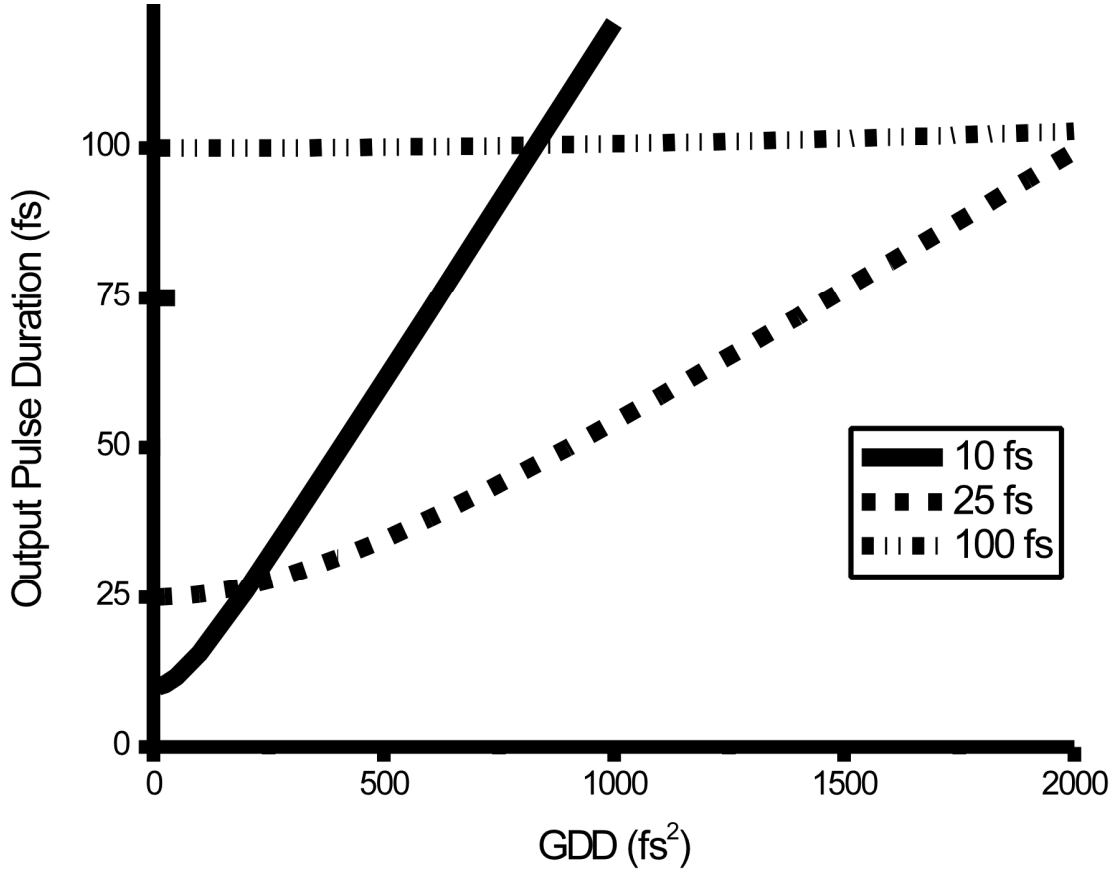

Figure 3.1. The effect of second-order-dispersion on pulse duration of ultrashort pulses. As a reference, 1 mm of quartz introduces 36 fs^2 GDD. High numerical-aperture microscope objectives, such as used for the experiments reported in this dissertation, contain as much as an inch (25.4 mm) of quartz.

3.1.3. Compensation

One approach to compensating for the dispersion experienced by a pulse as it travels through media is the use of a prism pair compressor, as shown in Figure 3.2. This approach has the advantage of simplicity; however, it is limited to compensation of quadratic dispersion only. While this is, indeed, the most significant dispersion component experienced by ultrashort pulses propagating through media, the higher order dispersions, including the cubic dispersion introduced by the glass of the prisms themselves, may still cause deleterious effects.

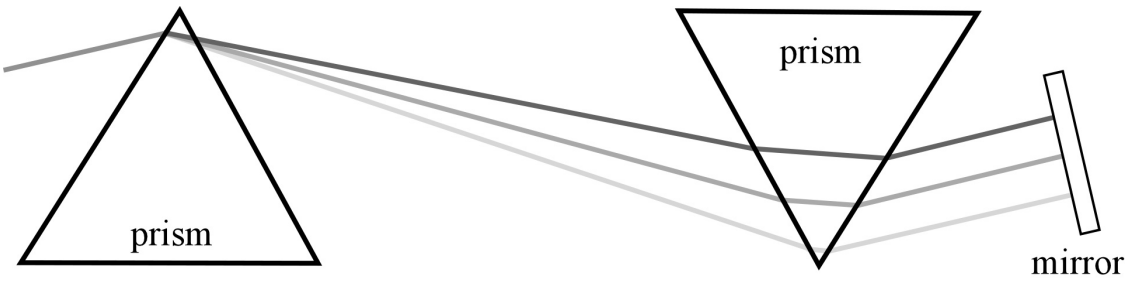

Figure 3.2. Prism pair compressor used to compensate for quadratic dispersion. The first prism disperses the beam, causing each frequency component of the pulse to travel through different amounts of the glass in the second prism. A mirror reflects the beam back along the same path for recombination.

Other disadvantages to the prism pair compressor approach are the facts that dispersions are not actually measured and that it is not possible to apply phases to the pulse. These limit the applications of such compression, when used alone. However, for setups in which high quadratic dispersion is present, such as when a high numerical-aperture objective is used, a prism pair compressor can be successfully used in conjunction with other measurement/compensation methods to optimize results.

In the early 2000's, the established phase measurement methods included frequency resolved optical gating (FROG)[89-95] and spectral phase interferometry for direct electric-field reconstruction (SPIDER).[96-99] These methods, and their variants, depend upon the measurement of autocorrelations or cross correlations between two pulses to characterize the spectral phase of a pulse. In FROG, the frequency and time-resolved signals are used to retrieve the spectral phase of the pulses. SPIDER requires that the laser pulse be split into two beams that are then upconverted by a heavily chirped pulse. The interference of the upconverted pulses in the spectral domain is used to reconstruct the spectral phase in the original pulse.

3.1.4. Pulse Shaping

The full power of ultrafast lasers can be exploited by the use of pulse shaping, or controlling the phase of each frequency of the pulse. In the spectral domain, this can be used for the selection of specific frequencies for selective multi-photon excitation. In this case, constructive interference between different components of the pulse is used to optimize the desired frequency, and destructive interference between other components to minimize the background. In the time domain, phase can be used to chirp the pulse, where red frequencies arrive before blue or vice versa, or to create pulse trains with very specific timing between pulses, a technique that has been shown to optimize CARS.[100-105] Other applications include optical communications,[106] control of chemical reactions,[107,108] nonlinear optical processes,[102,109] semiconductors,[110] quantum[111] and nonlinear optical computation,[112] and biomedical applications.[113] Ideally, characterization and pulse shaping can be used together to produce pulses with a precisely determined phase function, such as a TL pulse. Combining the characterization and shaping of pulses has been attempted through intricate methods that either utilize a genetic algorithm (GA)-controlled shaper to optimize a nonlinear optical signal,[114-138] or implement time-domain interferometry with an acousto-optic programmable filter.[139] These indirect methods are limited by the lack of sensitivity of the total nonlinear optical signal to phase deformations outside the FWHM of the spectrum.

The method presented in Section 3.3, MIIPS, takes advantage of the influence that phase modulation has on the probability of nonlinear optical processes at specific frequencies.[140-143] It is a single beam method that not only characterizes spectral phase but also compensates for unwanted phase distortions and can deliver accurate user-specified phase functions at the location of a sample. It does not require beam splitters, interferometry, autocorrelation, or global optimization, and is capable of analytically retrieving the spectral phase across the pulse. Consequently, this method has proven to be extremely powerful for the accurate and reproducible demonstration of selective microenvironment probing,[144] multiphoton microscopy[145-147] functional imaging,[148,149] chemical agent identification,[150] and encoding of information using ultrashort phase-shaped pulses.[151]

3.2. Experimental Setup

A schematic of the general experimental setup used for the experiments shown in the next two chapters is shown in Figure 3.3. Details of each component are described in the sections below. Briefly, an ultrashort (~10 fs) laser pulse was generated by a Ti:sapphire oscillator. The laser was then passed through a spatial light modulator (SLM)-based pulse shaper, which compensates for spectral phase distortions in a pulse, compressing it to its transform-limited pulse duration with MIIPS. Known phase functions can also be applied to the pulse as required for particular experiments. The beam was then passed into the rear port of an inverted microscope and focused onto the sample. A wide-field image of emitted light was collected by an electron-

multiplier charge-coupled-device (EMCCD) camera and passed to a computer for data processing.

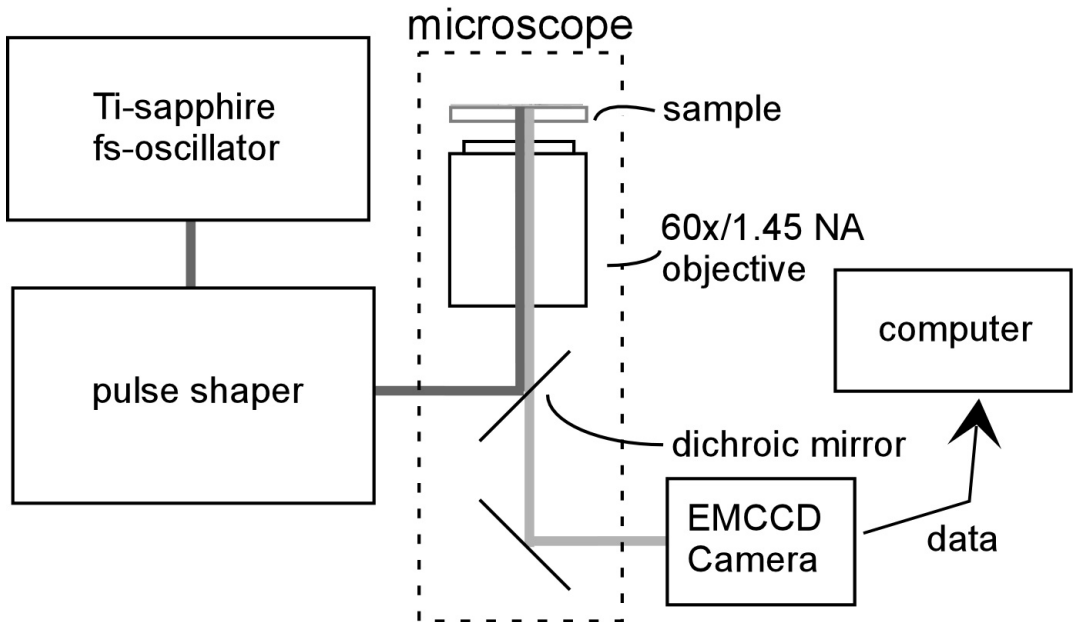

Figure 3.3. A schematic of the general experimental setup.

3.2.1. The laser

The excitation source used in all the experiments in this dissertation was a KM Laboratories Ti:sapphire femtosecond laser, pumped by a Spectra-Physics Millennia V solid state diode-pumped laser, which has a wavelength of 532 nm. The fs-laser is capable of producing sub-10 fs pulses (110 nm FWHM) centered around 800 nm. The average output power of the oscillator was 250 mW, with a repetition rate of 97 MHz. A typical spectrum of the laser pulses is shown in Figure 3.4.

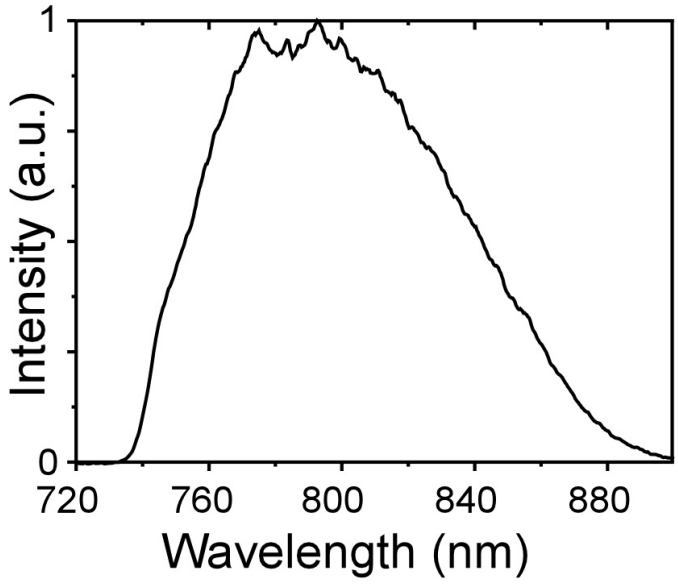

Figure 3.4. Typical spectrum of the 10-fs laser pulses generated by the KM Laboratories Ti:sapphire femtosecond laser used for the experiments presented in this dissertation.

3.2.2. Pulse Shaper

The pulse shaper is the means by which the phase of each spectral component of the laser pulse is controlled, and is an integral part of the experimental setup for both compensation purposes and for future experiments on surface plasmon polariton propagation. The design used here, based on the general 4-f design of Weiner,[152] is shown in Figure 3.5. It consists of two 600 grooves/mm gratings, two 200-mm focal

length cylindrical mirrors and a dual-mask SLM (CRi, Inc., SLM-256). In this design, the laser entering the pulse shaper first strikes the grating, which disperses the frequency components of the broadband laser pulse, while the cylindrical mirror focuses the spread beam onto the SLM. The beam is then recombined by a parallel set of optics. The SLM used in these experiments is dual-mask, with 128 liquid crystal pixels. Changing the potential applied to each pixel changes the index of refraction, retarding the light traveling through that pixel. As the spectrum is dispersed across the pixels, this allows the relative phase of individual frequency components to be independently controlled. To achieve accurate phase delays, each pixel of the SLM was carefully calibrated by measuring the polarization-dependent transmission of light through each pixel; pixel-by-pixel calibration is necessary because of the frequency dependence of index of refraction values.

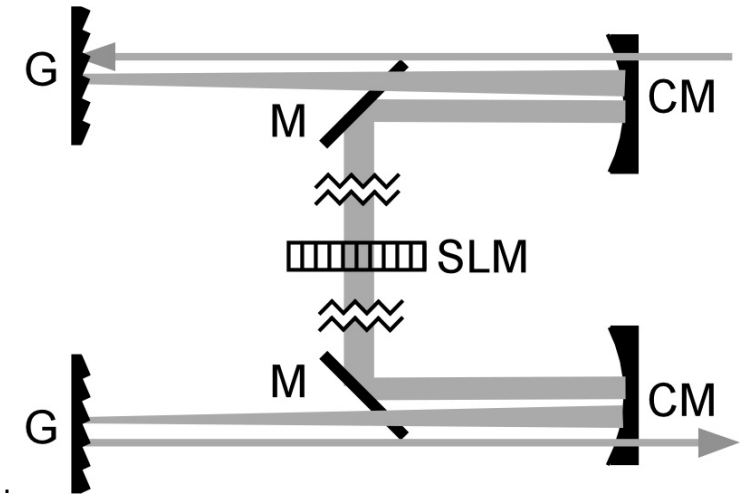

Figure 3.5. Schematic of the pulse shaper. G = grating, CM = cylindrical mirror, M = flat mirror, SLM = spatial light modulator. The beam enters the pulse shaper at the top-right of the schematic, and exits at the lower right. The offset shown for the beams is for clarity only. In the setup, a vertical offset is used, so that the incoming beam goes over both the cylindrical and flat mirrors, strikes the grating, goes over the flat mirror again, striking the cylindrical mirror, and finally striking the flat mirror, which directs it to the SLM.

3.2.3. Microscope

After leaving the pulse shaper, the beam was then steered towards the rear port of a Nikon TE-2000U inverted microscope. Neutral density filters were placed in the beam path after the shaper but before the microscope in order to moderate its power. Typically, a low optical density filter was used during compensation with MIIPS, and then a higher optical density filter of the same thickness was used during the experiments. This allowed for proper compensation of the dispersion introduced by the filter.

The beam out of the pulse shaper was smaller than the entrance aperture of the 60x/1.45 NA objective. Therefore, when this objective was used, a Galilean beam expander was used to expand the beam to overfill the microscope objective, and ensure the tightest focusing. While this did result in the loss of power, most of the experiments discussed in the next chapters of the dissertation required considerable reduction of power to the sample to prevent damage, and so this loss was not a problem.

Inside the microscope, a 650 nm shortpass dichroic mirror was used to direct the excitation beam up to the sample, where a Nikon 60x/1.45 NA objective tightly focused the beam at normal incidence onto the sample with a focal spot of ~1 μm. Emission was collected back through the same objective; however, the dichroic mirror allowed emitted light <650 nm to pass through, where it was then directed to the Andor iXon EMCCD camera for detection. A cover was used over the sample during experiments to eliminate the inadvertent collection of ambient light, not only substantially reducing the background but also preventing fluctuations due to shadows falling over the sample and collection optics.

The primary microscope objective used for the experiments reported in this dissertation was a Nikon Plan Apo TIRF oil immersion 60x/1.45 NA objective (Type NF immersion oil was used.) For some experiments, in which a wider field of view was desired, or in which the use of immersion oil would not be appropriate, a Nikon Plan Fluor ELWD 40x/0.60 NA objective, which will be referred to simply by its power and numerical aperture (40x/0.60 NA) was used. The resulting focal spot size for both of these objectives is less than 1 μm.

3.2.4. Detection

The detector used to image the emission is an Andor iXon back-illuminated EMCCD camera, thermoelectrically cooled to -64℃. This camera is highly sensitive, with a quantum efficiency (QE) >80% over the visible spectrum, from 450-750 nm, and 90% from 500-650 nm. It contains an array of 512x512 pixels, each 16x16 μm in size. With the 60x/1.45 NA objective typically used, this results in a field of view of approximately 135 μm in each dimension. For the 40x/0.60 NA objective occasionally used, imaging capabilities expand to 205 μm in both dimensions.

The sensitivity of the camera is a significant part of what makes the experiments presented in the next two chapters possible, as the excitation beam power must be kept low to prevent photodamage. Therefore, optimizing gain and integration time settings were important issues. A typical integration time was 200 ms, while gain settings between 100-150 were found to be ideal. Longer integration times increased the length of the experiments, therefore increasing the risk of photodamage to the sample, while shorter integration times did not appreciably shorten the duration of the experiment, due to data transfer times. Under these integration times, gain settings above 150 generally

led to an unsatisfactory amplification of noise, while the system was better served by reducing the power instead of reducing the gain below 100.

3.2.5. Integration of Systems

An essential component of the work presented in the next two chapters was the development of a program to coordinate the behavior of the computer controlled devices used. Specifically, the SLM and the camera had to be under full control of the user to ensure processes happened in the appropriate sequence. National Instruments' LabVIEW program was used to coordinate the instrumentation described here. Using drivers, and, in some cases, sub-routines, provided by the companies, as well as utilizing portions of programs for control over the SLM previously written by other members of the Dantus group, a program was written to permit full control over the various capabilities and to ensure the timing of various processes.

3.3. Multiphoton Intrapulse Interference Phase Scan (MIIPS)

The following section is adapted from Ref. 153, on which I am the 2nd author.

3.3.1. MIIPS Theory

MIIPS is an analytical method for retrieving and compensating the phase across the spectrum of the laser pulse. Unlike other approaches, it is a single-beam method and is capable of not only characterizing the spectral phase of the pulses, but

compensating for the measured distortions, and, when desired, using the same setup to apply user-defined phase functions.

In MIIPS, a known reference function, $f(\omega)$, is introduced by a pulse shaper to cancel, at least locally, distortions by the unknown spectral phase $\phi(\omega)$ of the pulse. The sum of the unknown phase and the reference phase is given by $\varphi(\omega) = \phi(\omega) + f(\omega)$. The second-harmonic-generation (SHG) spectrum resulting from the total phase $\varphi(\omega)$ can be used to retrieve $\phi(\omega)$ accurately.

Assuming the use of a thin nonlinear crystal with a pulse that is a few optical cycles long,[154, 155] the SHG intensity $S^{(2)}$ at frequency 2ω can be written as an integral over the spectral amplitude $|E(\omega)|$ and phase $\varphi(\omega)$ of the pulse:

$$S^{(2)}(2\omega) \propto \left| \int |E(\omega+\Omega)||E(\omega-\Omega)| e^{\{i[\varphi(\omega+\Omega)+\varphi(\omega-\Omega)]\}} d\,\Omega \right|^2 \qquad (3\text{-}2)$$

According to this equation, the signal is proportional to the integral of the product of a real positive kernel, $|E(\omega+\Omega)||E(\omega-\Omega)|$, with the complex exponent of phase $\varphi(\omega+\Omega)+\varphi(\omega-\Omega)$. TL pulses ($\varphi = 0$) generate the maximum intensity for a SHG spectrum because the oscillatory component of the integral is zero.

According to eq (3-2), the SHG spectrum is maximized when $\varphi(\omega+\Omega)+\varphi(\omega-\Omega)$ is zero. Based on the Taylor expansion of this expression:

$$\varphi(\omega+\Omega) + \varphi(\omega-\Omega) = 2\varphi(\omega) + \varphi''(\omega)\Omega^2 + \cdots + \left(\frac{2}{(2n)!}\right)\varphi^{2n'}(\omega)\Omega^{2n} \qquad (3\text{-}3)$$

where $\varphi^{n'}(\omega) \equiv d^n\varphi(\omega)/d\omega^n$, the SHG spectrum has a local maximum, to first approximation, at ω when the quadratic phase term, φ''(ω) equals zero, i.e., when

$$\varphi''(\omega) = \phi''(\omega) + f''(\omega) \rightarrow 0. \tag{3-4}$$

At this frequency, $f''(\omega)$ compensates $\phi''(\omega)$, and the unknown function $\phi''(\omega)$ can be retrieved; this concept is illustrated in Figure 3.6(a).

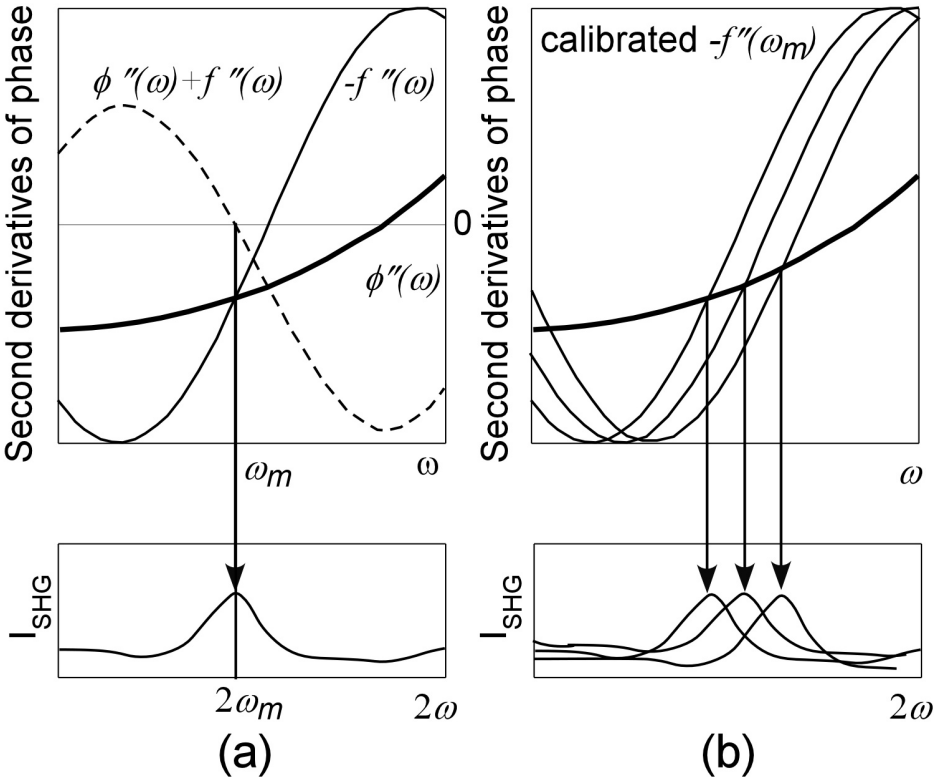

Figure 3.6. Schematic of MIIPS concept. (a) The thicker line shows the second derivative of the unknown phase distortion, $\phi''(\omega)$, the thinner line is the negative of the second derivative of the well-known reference function, $-f''(\omega)$, and the dashed line is the sum of the two, $\phi''(\omega)+f''(\omega)$. The SHG signal will have a local maximum when the sum of $\phi''(\omega)$ and $f''(\omega)$ is zero (i.e., when $-f''(\omega)$ intersects with $\phi''(\omega)$). (b) When the well-known reference function, $f(\delta,\omega)$ scans across the spectrum, SHG signals are maximized at different frequencies, as the intersection of $-f''(\omega)$ and $\phi''(\omega)$ changes.

To measure the phase distortion across the spectrum, the reference function, $f(\omega)$, is parameterized as $f(\delta,\omega)$, where δ is a parameter that is scanned, so that the

reference function samples all frequencies in the bandwidth. The resulting SHG spectrum, $SHG(\delta,2\omega)$, reaches a maximum when

$$\varphi''(\delta_m(\omega),\omega) = \phi''(\omega) + f''(\delta_m(\omega),\omega) \to 0 \qquad (3\text{-}5)$$

where $\delta_m(\omega)$ denotes the δ value of the SHG maximum for each frequency. Graphically (see Figure 3.6(b)), this condition can be represented as an intersection of the second derivative of the unknown, and the negative of the calibrated scanned function, i.e. $\phi''(\omega) = -f''(\delta_m(\omega),\omega)$.

Based on eq (2)(3-4), the resulting SHG spectrum, $SHG(\delta,2\omega)$ reaches a maximum when $\varphi''[\delta_m(\omega),\omega]=\phi''(\omega)+f''(\delta_m(\omega),\omega] \to 0$ or $\phi''(\omega)=-f''[\delta_m(\omega),\omega]$, where $\delta_m(\omega)$ denotes the δ value of the SHG maximum for each frequency. The phase of the pulse across the whole spectrum $\phi(\omega)$ can be analytically retrieved by double integration of $\phi''(\omega)$ in the frequency domain. SHG and MIIPS are not affected by the choice of integration constants, the relative phase ϕ^0 and linear term ϕ'.

3.3.2. Implementation of MIIPS

For the MIIPS measurements made in this dissertation, a sine function was utilized as the reference:

$$f(\delta,\omega) = \alpha \sin(\gamma\omega - \delta) \qquad (3\text{-}6)$$

where α and γ are fixed parameters with values equal to 1.5π and the duration of the pulse, respectively; the phase shift, δ, is a parameter typically scanned from zero to 4π, as shown in Figure 3.6(b). By acquiring an SHG spectrum for each step over this range, two replicas of the MIIPS trace are obtained, as shown in Figure 3.7. The value

of $\delta_m(\omega)$ for each frequency is found, and from these values, the second derivative of the unknown phase is calculated by

$$\phi''(\omega) = \alpha\gamma^2 \sin\left(\gamma\omega - \delta_m(\omega)\right) \tag{3-7}$$

By substituting $\phi'' = 0$ into the above equation, it can be shown that, for TL pulses,

$$\delta_m^n(\omega) = \gamma(\omega - \omega_0) + n\pi, n = 0, \pm 1, \pm 2 \ldots \tag{3-8}$$

In a MIIPS trace, this results in TL pulses having parallel lines separated by π.

The phase of non-TL pulses are measured by finding the values for $\delta_m(\omega)$ for each of two regions, as shown in Figure 3.7, and the average is used to calculate the second derivative of the unknown phase distortions:

$$\phi''(\omega) = -\frac{1}{2}\alpha\gamma^2\left[\sin\left(\gamma\omega - \delta_m^1(\omega)\right) + \sin\left(\gamma\omega - \delta_m^2(\omega)\right)\right] \tag{3-9}$$

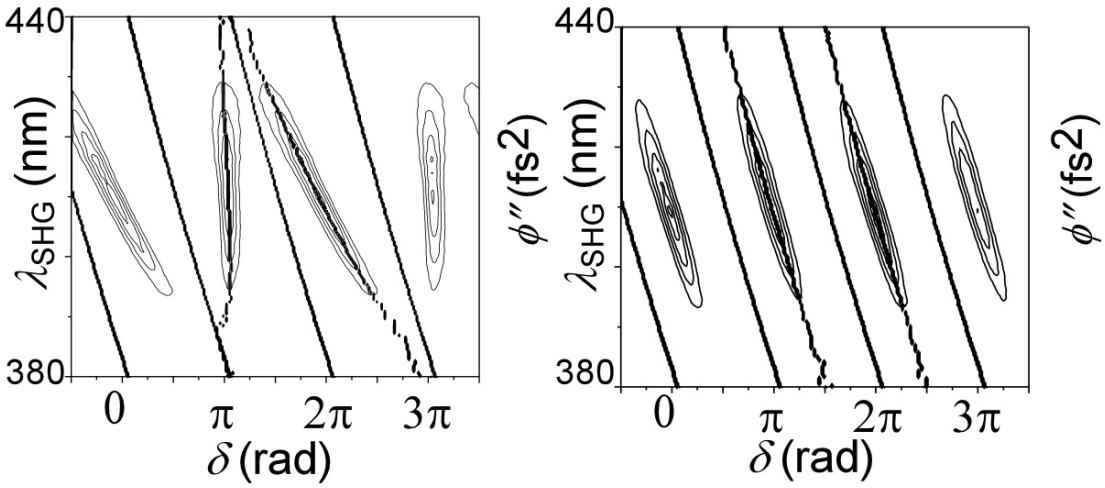

Figure 3.7. Experimental results for MIIPS. The panels are SHG spectra as the δ parameter of the reference function is scanned. Each vertical line corresponds to a separate SHG spectrum obtained at a given value for δ. The black lines which separate the MIIPS traces are used to define the region for searching $\delta_m(\omega)$. The dots within those boundaries show $\delta_m(\omega)$. The panel on the left is the MIIPS trace for a typical uncompensated pulse. After several iterations, the traces on the right, which correspond to TL pulses, are seen.

To optimize the accuracy of MIIPS, an iterative procedure of measurement and compensation is used. The experiment begins as described above, and the phase is retrieved. To compensate this distortion, the measured phase of the first iteration, $-\phi^{I}(\omega)$ is added to the applied phase using the pulse shaper, the process is repeated, and the next order of phase correction, $\phi^{II}(\omega)$ is measured. The sum $-(\phi^{I}(\omega)+\phi^{II}(\omega))$ is used as the correction function. The convergence towards an accurate result is exponentially fast. By using this iterative approach, large dispersions, e.g., dispersions larger than the range of the shaper, can be quantified and compensated.

3.3.3. Validation of Method

The basic experimental setup for MIIPS necessitates only a thin SHG crystal, a spectrometer, and a pulse shaper capable of accurately introducing spectral phase modulation (Figure 3.8). It is worth noting that there are no beams to overlap in space and time, and there are no moving parts. Using this setup, a series of experiments were performed to quantify the capabilities, as well as validate the accuracy and precision of MIIPS as it compares to other methods of compensating the phase distortions in pulses.

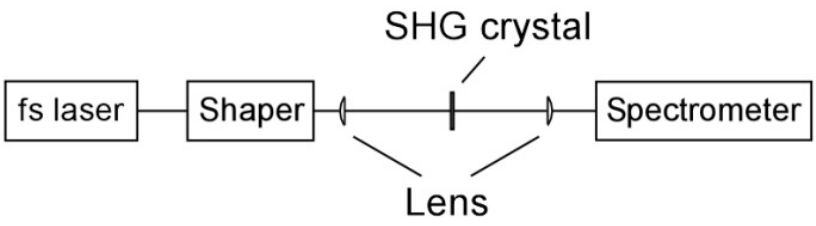

Figure 3.8. Experimental setup for MIIPS

The ability of MIIPS to accurately retrieve the spectral phase of a pulse was tested by first compensating the pulse to make it TL, and then applying known phases and using several iterations of MIIPS to retrieve those phases. Two phase functions were applied: a double Gaussian function and four periods of a sinusoidal function. These functions are shown by the solid lines in Figure 3.9. The phase retrieved by MIIPS is shown by the dots. It can be seen that MIIPS is capable of retrieving these synthetic phases quite accurately.

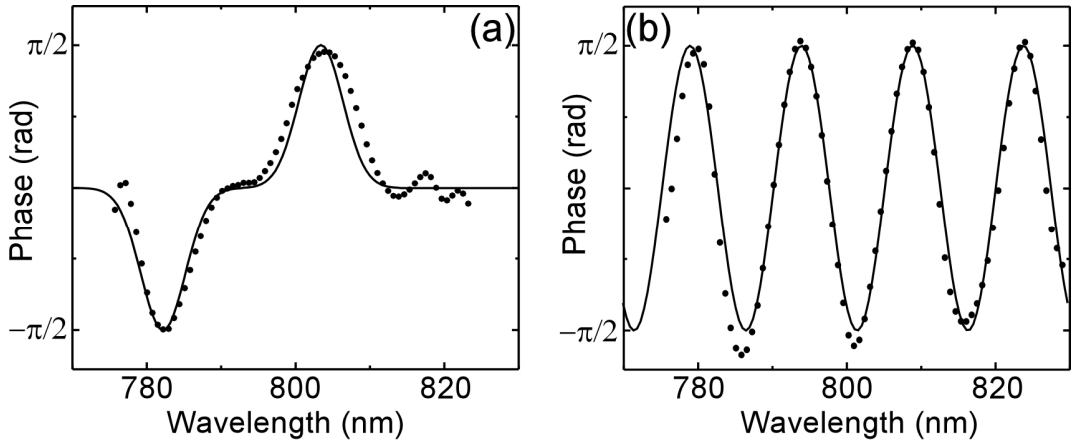

Figure 3.9. Ability of MIIPS to retrieve arbitrary phase functions. (a) The result for an applied double Gaussian function. (b) The result for an applied sine function. The dotted curves show the retrieved phase, and the solid curves are the applied phase.

Another test was performed to ensure that MIIPS is capable of not just retrieving the phase, but accurately compensating for the phase measured. To do this, MIIPS was used to compensate for the dispersion of the pulse. Two known phases, a square wave and a sinusoidal wave, were then applied to the pulse, and the resulting SHG spectrum compared to that predicted by theory. The results are shown in Figure 3.10, with the spectrum and applied phases shown above each of the results. In panels (a) and (c), it is seen that theory (solid lines) and experiment (dots) agree well, indicating that the use of MIIPS results in well-behaved TL pulses. As a comparison, the bottom

panels show the SHG spectra obtained when the phases are applied, but the laser is not compensated. It is clear that without compensation, the dispersions in the system have significant deleterious effects on nonlinear processes. This reiterates both the necessity for a method such as MIIPS as well as the effectiveness of MIIPS in compensating for these dispersions.

Another test of MIIPS' performance was the reproducibility. For this experiment, several iterations of MIIPS were run to acquire a compensation mask (the negative of the measured phase). This compensation mask was applied, and a single iteration of MIIPS was run ten times successively (each time starting from the compensation mask). The results for the retrieved phase are shown in Figure 3.11. The lower panel shows the average retrieved phase across the entire spectrum of the pulse, with error bars denoting ± 1 standard deviation for every fifth point. The upper panel shows the same results, focused in on the portion of the spectrum over which MIIPS can compensate. As the figure shows, MIIPS is highly reproducible over a very broad portion of the spectrum (essentially the portion where the red spectrum is more than 10% of the maximum value).

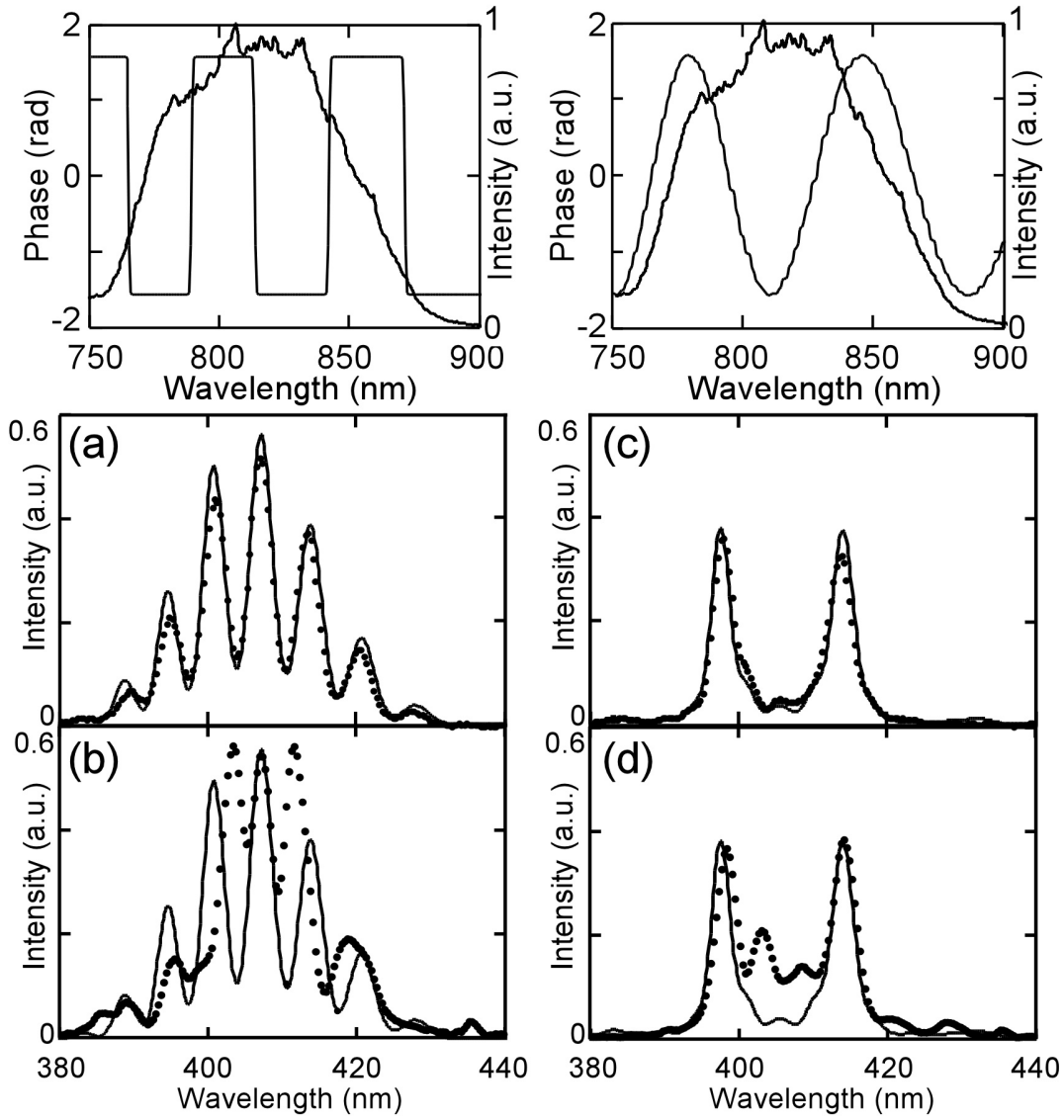

Figure 3.10. Comparison between experimental data and theoretical simulation. The solid curve in each panel shows the theoretical spectrum predicted for the application of a particular binary phase (a) and (b) or a particular sine function (c) and (d). The dotted curves correspond to the experimentally measured SHG spectrum for each case. (a) The experimental result of the application of a binary phase mask (inset) to a pulse compensated by MIIPS. (b) The result of the application of the same phase mask to an uncompensated pulse. (c) and (d) The corresponding information using a sine function (inset).

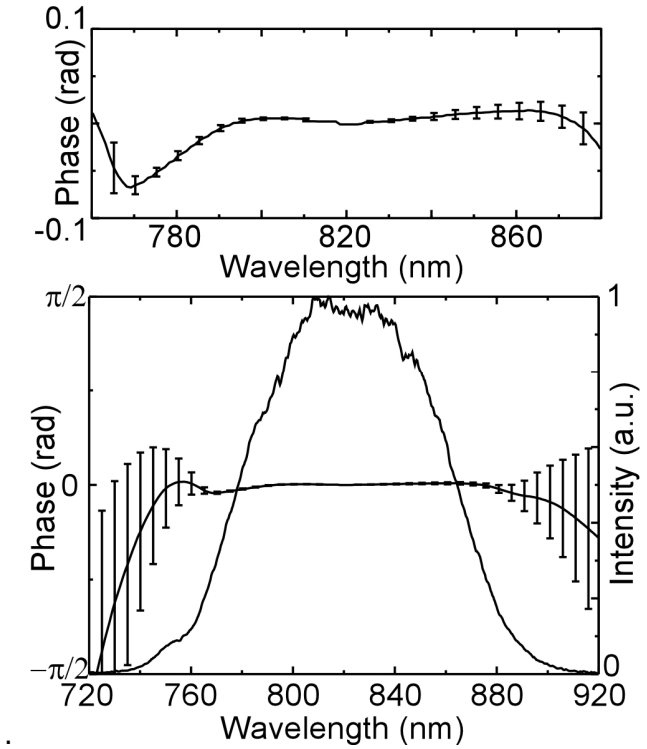

Figure 3.11. Reproducibility of MIIPS. In both panels, the solid curve shows the average of ten independently retrieved phases, while the error bars show ±1 standard deviation for every fifth point. The lower panel shows the full range of collected data. The upper panel shows a closer view of the region over which MIIPS can compensate (760–880 nm).

To quantify the reproducibility, and compare MIIPS to other, published, methods of compensation, the statistical phase error was calculated by averaging the standard deviation at each point, using the power spectrum as a weighting function. Over the entire range of the spectrum, analyzing the full set of data, the statistical phase error was calculated to be 0.013. Using a reduced set of the first five scans, the statistical phase error is reduced to 0.011. These results, as well as a comparison with FROG and SPIDER, are shown in Table 1, below. Also of interest is the great reduction of the statistical phase error when the range of data analyzed was reduced to that in which the retrieved phase was flat (i.e. MIIPS had successfully compensated). For this range, the

statistical phase error was reduced to just 0.004 rad. Over the FWHM of the pulse, the statistical phase error is further reduced to 0.0028 rad.

Table 1. Comparison of Reproducibility of MIIPS with FROG and SPIDER: Statistical Phase Error (in rad)

Method	Full Data Set	Reduced Data Set	Full Data Set (FWHM)
MIIPS	0.013	0.011	0.0028
FROG[156]	0.122	0.048	
SPIDER[156]	0.044	0.017	

A different study, performed by Schlup and Bartels,[157] compared how robust these methods are to noise in the retrieved spectral phase of the pulse; MIIPS was shown to perform substantially better than FROG.

To further quantitatively test the accuracy of the phases retrieved by MIIPS, the GVD of quartz, a well-characterized material, was determined. In this experiment, MIIPS was used to measure the phase of the setup alone (0 mm quartz) and when quartz windows with thicknesses of 3.25, 4.92, 6.53 and 9.58 mm were placed in the path of the beam prior to its incidence on the SHG crystal. MIIPS was used to retrieve the second derivatives of the spectral phases of those pulses, and the spectral phase was quantified, with the results from MIIPS performed on the setup alone as a reference.

The second derivative of the phase for the different thicknesses of quartz. are shown in the top panel of Figure 3.12, and the GDD at 800 nm for each window is shown in the lower panel. It is important to note that the curves are both parallel and spaced proportionally to the thickness of the quartz. The GVD (GDD per unit length) introduced by the quartz windows was measured to be 36.2 ± 0.5 fs^2/mm at 800 nm.

For comparison, the “gold standard” experimental method of determining GVD is white light interferometry, which has determined the GVD of quartz to be 35.92 fs^2/mm.[158] For further comparison, the GVD of quartz at 800 nm was calculated using the Sellmeir formula and the constants found from Maltison[159] and was found to be 36.162 fs^2/mm, which is in excellent agreement with these measured results.

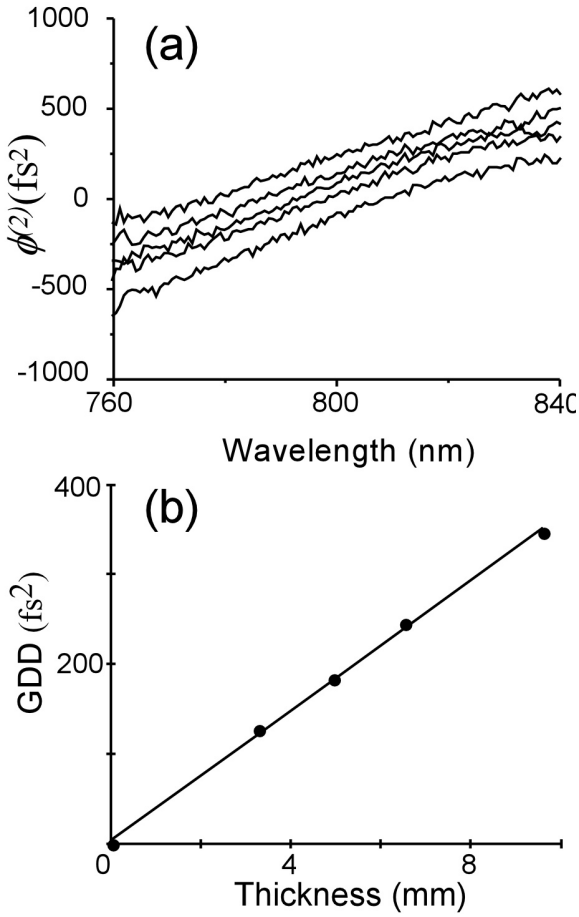

Figure 3.12. GVD measurement of quartz using MIIPS. (a) The retrieved second derivative of the spectral phases (from bottom to top: 0, 3.25, 4.92, 6.53, and 9.58 mm quartz windows). (b) The GDD at 800 nm as a function of thickness.

The measurement was then repeated with increasing numbers of glass microscope slides (crown glass, Fisher Scientific, 1 mm thick) sandwiched with Nujol oil, an index-matching fluid. As the thickness of the slides is uniform, reliable measurements will show a linear plot of GDD versus the number of slides used. The results are shown in Figure 3.13. The top panel shows the retrieved second derivatives of the spectra phase for every other slide addition, while the lower panels shows the GDD as a function of thickness, which can be successfully fitted by a line. The GVD introduced by the microscope slides was measured to be 50.7±0.5 fs^2/mm at 800 nm. Assuming the crown glass used in the microscope slides corresponds to Ohara glass S-NSL 5 (equivalent to Schott glass K5), the measured GVD can be compared with the value calculated using the Sellmeier formula with constants available from Ohara.[160] The GVD was calculated to be 50.13 fs^2/mm at 800 nm, which is in good agreement with the experiment.

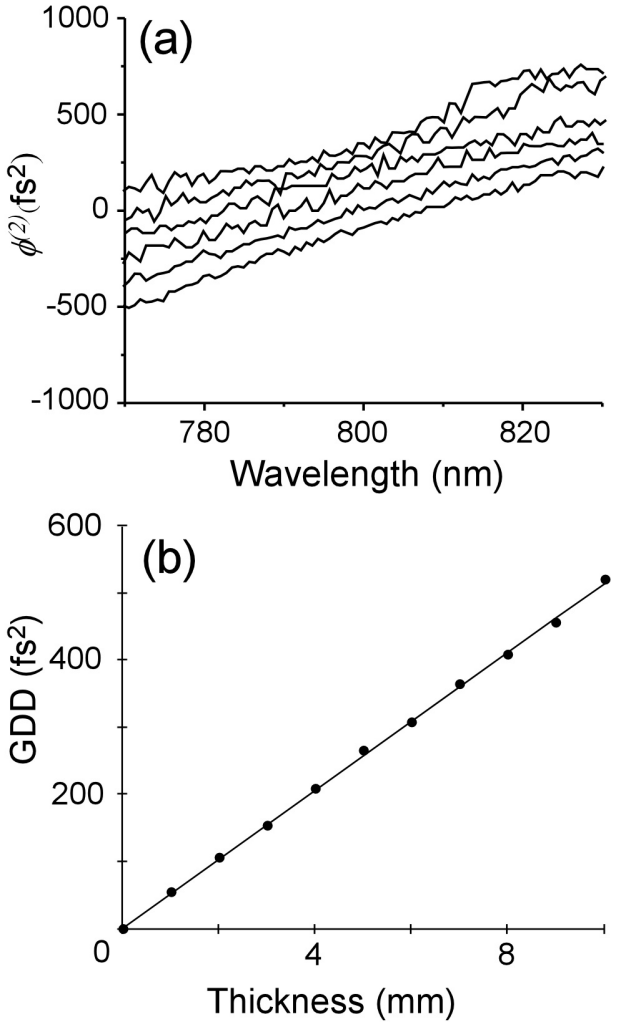

Figure 3.13. GVD measurement of microscope slides using MIIPS. (a) The retrieved second derivative of the spectral phases (from bottom to top: 0, 2, 4, 6, 8, and 10 mm microscope slides). Note that for clarity the odd number of slides (odd thicknesses) were omitted from this graph, but not from the calculation. (b) The GDD at 800 nm as a function of thickness.

3.3.4. Use of MIIPS in a high-NA Microscope Objective

Before MIIPS, the characterization of the spectral phase distortions of sub-10 fs pulses was limited to objectives with a NA up to 0.85.[161] For longer pulses, objectives with an NA up to 1.30 could be compensated.[162-165] This limitation to the most effective use of high-NA microscope objectives was one of the greatest obstacles to fully developing the potential of multiphoton imaging and other techniques that utilize

high focusing of ultrashort pulses, such as the results presented in this dissertation. It was therefore critical to demonstrate that MIIPS could compensate for these objectives. As the MIIPS method requires that second-harmonic (SH) be measured at the location of the sample, the same microscope setup discussed in Figure 3.3 was used, with detection optics mounted on a tower above the microscope objective for forward collection.

The three objectives that have specifically been tested were a Nikon Plan Fluor ELWD 20x/0.45 NA objective, a Nikon Plan Fluor ELWD 40x/0.60 NA objective, and a Nikon Plan Apo TIRF oil immersion 60x/1.45 NA objective. MIIPS alone compensated for the phase distortions introduced by the 20x/0.45 NA and 40x/0.60 NA microscope objectives (results not shown). To best compensate for all orders of phase distortion in the 60x/1.45 NA objective, however, a prism pair compressor utilizing SF10 prisms, was used to pre-compensate the quadratic phase contributions, which were on the order of 10^4 fs^2).

Figure 3.14 shows the residual phase after MIIPS is used to compensate for the dispersions in a typical microscopy setup utilizing the 60x/1.45 NA objective. The solid line, in both panels, shows the average phase residue from five independent measurements, while the error bars show ±1 standard deviation for every fifth point. The lower panel shows the full data set across the entire spectrum (shown by the dashed line), while the upper panel shows the data over the FWHM of the pulse. Note that the distortions are reduced to 0.1 rad over that range, indicating that MIIPS is compensating well. It is also important to note the extremely small standard deviations over this range, showing that MIIPS can very reproducibly compensate for the

distortions of even highly dispersive materials. The statistical phase error was calculated to be just 0.026 over the full range of data, where the uncompensated phase distortion was ~100 rad.

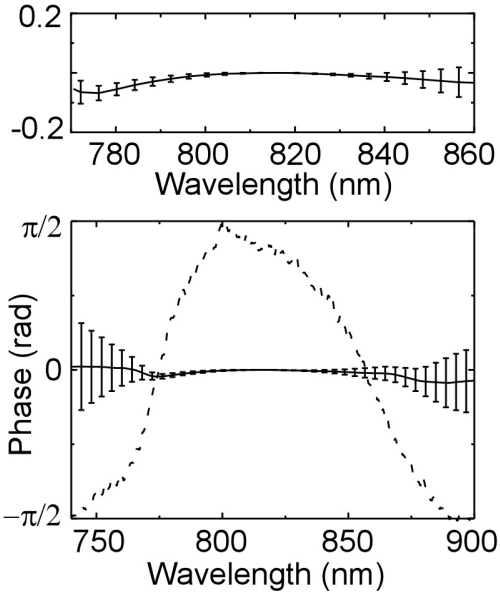

Figure 3.14. Compensation of spectral phase distortions caused by a 60x/1.45 NA objective. The error bars indicate ±1 standard deviation. The lower panel shows the full range of data, while the upper panel shows the same data over the FWHM of the pulse, on a reduced scale.

3.4. Conclusion

This chapter has presented the experimental setup used for the experiments presented in this dissertation. To summarize, the experimental setup is based around a ~12 fs laser coupled into an inverted microscope via a 650 nm short-pass filter and focused down to ~1 micrometer onto the sample. Wide-field emission is collected back through the objective and allowed to pass through the short-pass filter and to the highly-sensitive EMCCD camera.

To compensate for the phase distortions introduced by the propagation of the ultrafast laser through media, including the 60x/1.45 NA microscope objective used to

focus the beam, a prism pair compressor and 4-f pulse shaper were used in conjunction with MIIPS. A detailed documentation of MIIPS' accuracy and reproducibility is presented, confirming that the results presented in Chapter 5, in which information about the mechanisms of energy transfer in the system is obtained via studies of the effect of applied phases on emission intensity, are reliable and reproducible.

4. THE SAMPLE: PREPARATION AND CHARACTERIZATION OF LUMINESCENCE

This chapter and the following outline the results of the experiments performed to explore and understand the propagation of energy through the silver nanoparticle films. These chapters are adapted from Refs. 14 and 166, both articles on which I am the first author. They are reproduced in part with permission from Gunn, J. M.; Ewald, M.; Dantus, M., Polarization and phase control of remote surface-plasmon-mediated two-photon-induced emission and waveguiding. *Nano Letters* **2006,** 6, (12), 2804-2809. Copyright 2006, American Chemical Society, and from Gunn, J. M.; High, S. H.; Lozovoy, V. V.; Dantus, M., Measurement and Control of Ultrashort Optical Pulse Propagation in Metal Nanoparticle-Covered Dielectric Surfaces. *Journal of Physical Chemistry C* **2010,** 114, (29), 12375-12381. Copyright 2010, American Chemical Society.

4.1. Preparation of Sample

4.1.1. Synthesis

Silver nanoparticles were synthesized using the method utilized by Wensellers, et al.[3] In this method, a citrate synthesis,[41,167,168] 90 mg of $AgNO_3$ is dissolved in 500 mL of H_2O. The solution is brought to a boil, and 10 mL of 1% sodium citrate is added. The solution is boiled for an hour, resulting in a green-gray suspension. After cooling to room temperature, cluster formation is induced by adding 15 mL of 0.026 M fumaric acid,[169] and the solution is allowed to precipitate onto the substrates, typically for 48 to 72 hours. The effect of different precipitation times is discussed in more detail in Section 4.4.2. In this reaction, the citrate plays two roles, acting as both a reducing

agent, promoting the growth of the silver nanoparticles, and a capping agent which stabilizes the nanoparticles. While citrate is the most commonly used reducing agent for the synthesis of silver nanoparticles,[168] others can be used,[170] including EDTA[42] and Eriochrome Black T.[171] The choice of reducing agent and its concentration has been shown to affect the size, shape and dispersity of the synthesized nanoparticles.[42,168]

The primary substrates used were 0.15 mm-thick quartz coverslips, although a few experiments were performed using atomically flat mica as a control. As no differences in the optical behavior were observed, quartz was used for all optical experiments presented in this dissertation due to ease of use.

4.1.2. Microscopy of the Sample

Electron microscopy images were obtained in order to characterize the nanoparticle samples. Panels A-C of Figure 3 show transmission electron microscopy (TEM) images obtained of the samples, while panel D shows a scanning electron microscopy (SEM) image obtained. The TEM images indicate that the nanoparticles form primarily as roughly spherical structures (Figure 3A), with a small quantity as rods (Figure 3B), with dimensions on the order of 50 nm, while the SEM image shows the dendritic nature of the nanoparticle aggregate film.

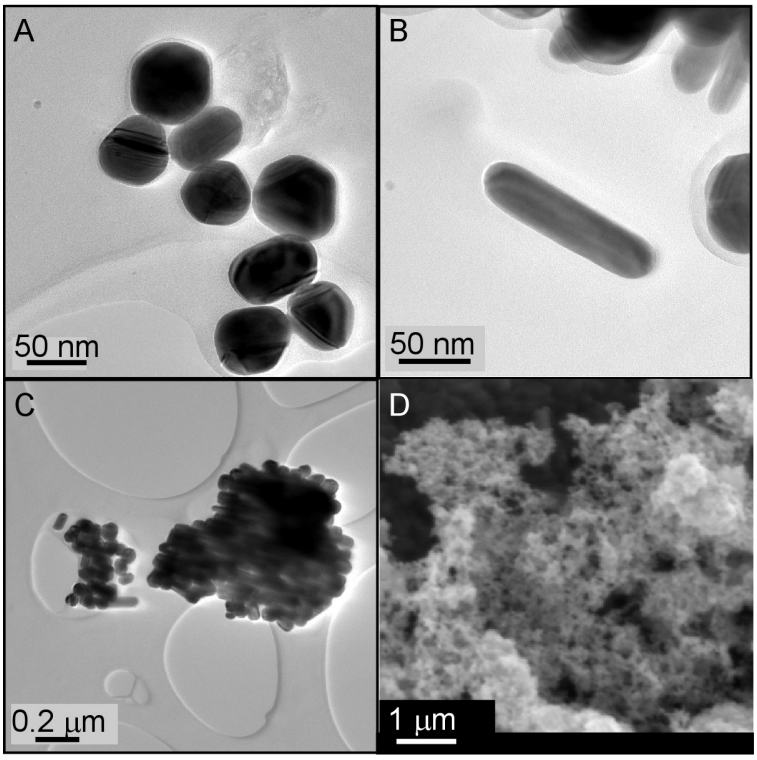

Figure 4.1. Panels A-C show TEM images of individual silver nanoparticles, which form both as roughly spherical structures and as rods. Panel D shows an SEM image of the structure of the aggregates formed. Electron microscopy images were obtained by Professor Martin Crimp, Michigan State University.

Further characterization of the samples was done via atomic force microscopy (AFM). Images of a typical sample are shown in Figure 4.2. As shown in Figure 4.2A and B, the dielectric surface is only partially covered. There are a few large (micrometer-sized) agglomerations of nanoparticles (seen prominently in Figure 4.2A), as well as interconnections among islands, observed in the form of regions with nanoparticles at distances shorter than the incident laser wavelength, shown in Figure 4.2B.

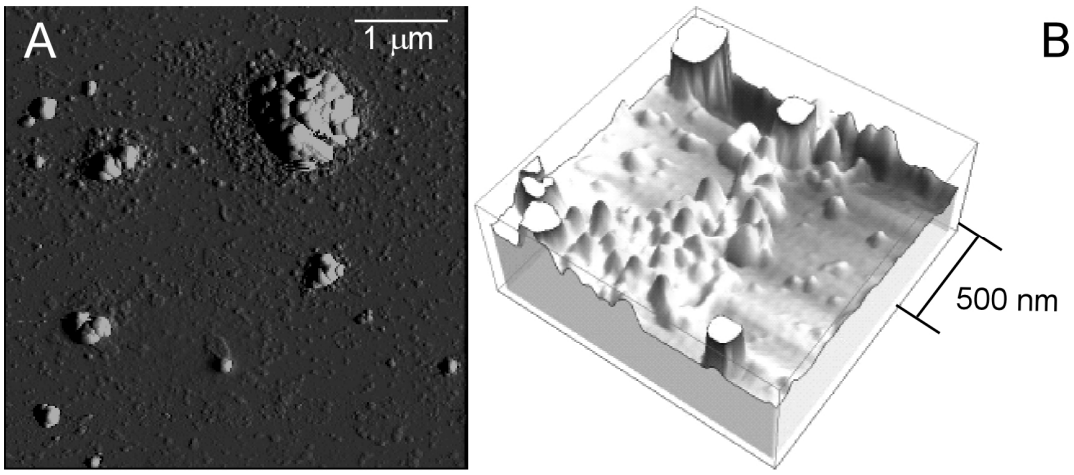

Figure 4.2. Panel A, AFM image of typical sample, illustrating the larger features of the sample. Panel B, AFM image of typical sample, with an emphasis on the smaller, more connected features that lie in between the larger features. Figure 4A was obtained by Professor Virginia Ayres, Michigan State University.

4.1.3. Control Experiments

Several control experiments were performed to determine if ambient oxygen or humidity affected the optical properties of the samples. In one set of experiments, samples were prepared with either nitrogen or air continuously bubbling through the solution during synthesis, and over it during precipitation. In another, samples spin-coated with a protective polymer layer were compared to those left exposed. In each of these experiments, there was no difference observed in the optical properties.

Another consideration is that irradiation has been shown to change the shape (and therefore the optical properties) of metallic nanoparticles.[172-178] To assure that ambient radiation was not altering the samples, a final control experiment was performed in which every stage of the process, from the synthesis to the experiments themselves, were performed in complete darkness. Some of the samples were then irradiated with light from a mercury lamp for eight hours. No difference in optical

properties was observed between the samples synthesized and used under normal, ambient conditions and those produced under darkness, with or without subsequent UV irradiation.

Due to these results, all subsequent synthesis was performed under ambient conditions. While samples were typically stored in a dark cabinet, and experiments performed in the dark (to minimize background), no special care was taken to protect the samples from ambient light during transfer and preparation of the experiment. However, there was no visible degradation of the samples, and they could be used regularly over a period of months with no change in their optical properties.

4.2. Hypothesis

As briefly mentioned in Chapter 1, emission is observed from these samples when excited with the laser system discussed in Chapter 3. The rest of this chapter will seek to characterize and identify the nature of this emission, while the following chapter will investigate the energy transport leading to emission so remote from the focal spot.

There are several possible sources of emission from metallic nanoparticles structures. One initial hypothesis is that the detected photons are from scattered laser light (~800 nm). However, a compelling case for the absence of simple scatter can be made by an examination of the experimental setup. As explained in detail in Section 3.2.3, there is a short-pass dichroic mirror (cut-off=650 nm) in the microscope setup to separate the excitation and emission signals. When a Schott glass BG39 filter, which has essentially zero transmittance above 750 nm, was placed in the emission beam path, there was no change in the intensity. If the detected light were trace remnants of

the fundamental pulse, a reduction or complete elimination of the signal would have been observed.

In addition to scattering of the fundamental excitation beam, rough surfaces can result in SHG[179-183] which could then also be scattered. Another possible source of emission is luminescent emission after two-photon excitation. This luminescence process is from the excitation of electrons from the d to the sp conduction band,[184,185] resulting in a broad, visible emission. Luminescence was first observed in bulk gold and copper in 1969, although with an extremely low quantum efficiency,[186] and has since been observed with several orders of magnitude higher efficiency in gold nanoclusters,[187-190] nanoparticles[185,191,192] and colloid films.[193] In silver, luminescence has been observed in nanoclusters,[194] silver oxide films (via production of Ag nanocrystals),[195-198] island[199] and colloid[199-201] films, as well as fractal[199] and patterned[202] films. This substantial increase in efficiency is possible due to the amplified local electromagnetic fields, as discussed in Section 2.2.1, which has been shown to readily provide an enhancement in the two-photon excitation or hyper-Raman excitation of molecules.[5,33,39,180,203-208]

4.3. Characterization of Solution

4.3.1. Spectrum

Initial characterization of the spectral properties of the silver nanoparticles was done by studying the properties of the solution after aggregation, but before precipitation. Most significantly, we were interested in the emission spectrum of the

aqueous sample upon excitation with an ultrafast laser. To most closely mimic the microscope setup that was to be used in future experiments, collection of emission was done along the z-axis, with the filter cube used in the microscope used to separate the excitation and emission beams, as shown in Figure 4.3. The resulting spectrum, collected with an excitation power of 25.1 mW and shown over the entire range of the spectrometer, is shown in Figure 4.4.

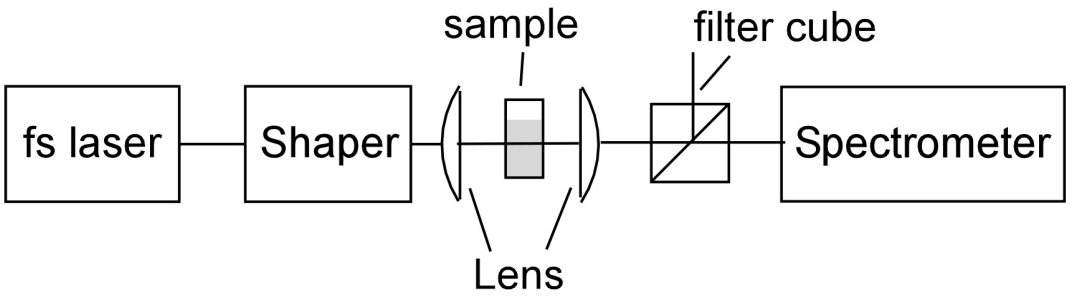

Figure 4.3. Setup for acquiring the emission spectrum of the silver nanoparticle aggregates in solution. The filter cube from the microscope is used to minimize excitation light reaching the detector.

The structure observed in the spectrum is most likely due to interference in the filter, possibly from the dichroic mirror used to separate the excitation and emission beams. The exact position of the structure can be shifted a small amount by slightly adjusting the position of the filter. The sharp cut-off at 650 nm is due to the cut-off filter in the cube. It can be seen that this filter has an extremely sharp cut-off, and is capable of suppressing the detection of light with wavelengths higher than 650 nm. Significantly, there is no evidence that any of the fundamental light (750-850 nm) passes through. This is further evidence that the light detected in future experiments on the microscope is not scattered fundamental. It is also significant that there is no emission centered around 400 nm, indicating that the detected light is also not the result of second-harmonic generation from the surface.[179, 180]

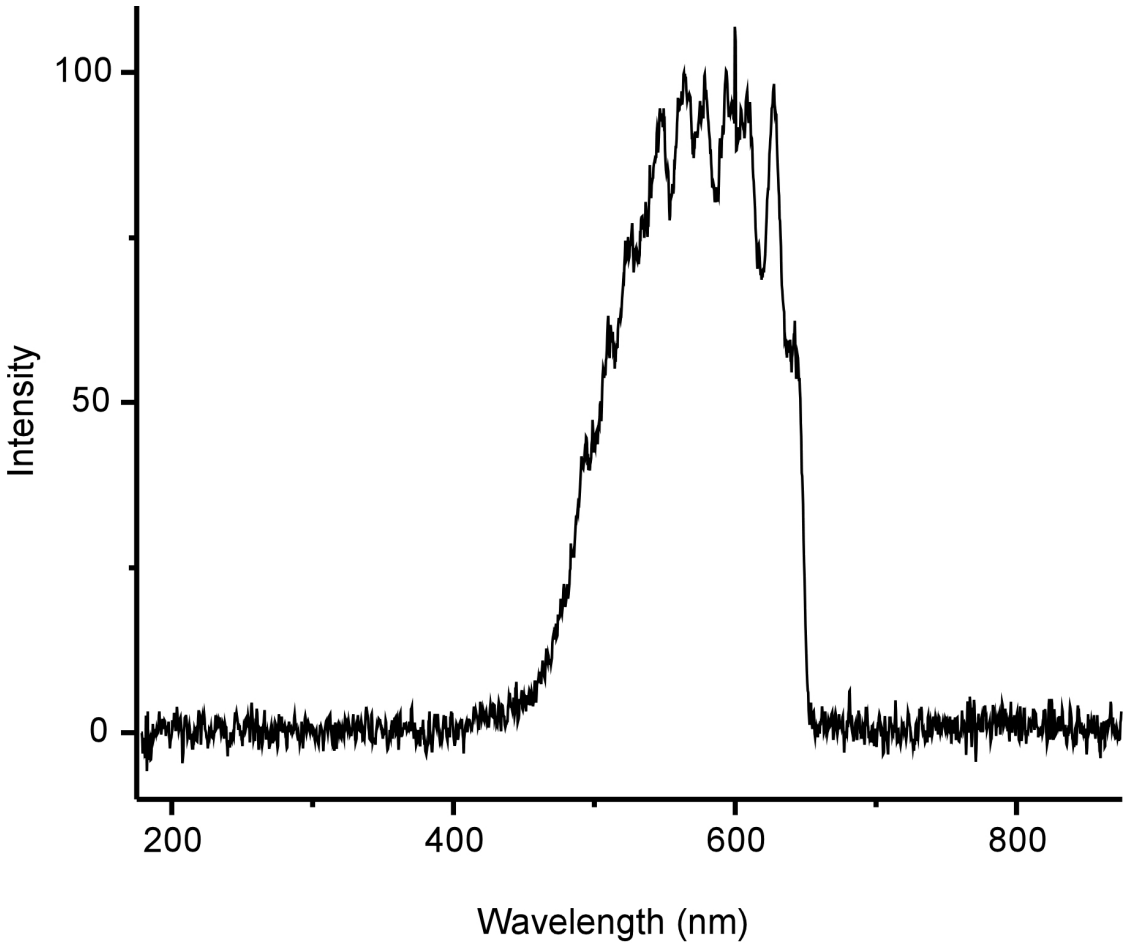

Figure 4.4. Full emission spectrum of silver nanoparticles aggregated in solution after excitation with a 13-fs Ti:sapphire laser. The spectrum is shown over the full range of the spectrometer; note that there is no evidence of either fundamental light (800 nm) or second-harmonic (400 nm). The observed structure is likely due to interference in the dichroic mirror.

4.3.2. Multiphoton Behavior

As discussed in detail previously, ultrafast lasers are capable of inducing nonlinear optical processes due to their high peak intensities. This has been observed in metallic nanoparticles: luminescence via a nonlinear absorption process was first noted in 1981, as a broad background beneath a strong surface-enhanced second-harmonic generation signal,[180] and was explored in more detail by Boyd, et al. in 1986.[209] It has since been observed and studied as third-harmonic generation in Au nanoparticles,[210] as two-photon-induced luminescence in gold nanoparticle colloids and aggregates,[211] nanostructured films,[179] as well as nanoparticles.[212-218] More recently, the two-photon-induced luminescence of Ag films[219] and nanoparticles,[220] have been studied, as well. The efficiency of two-photon excitation on metallic nanoparticles is high enough that it has been detected for continuous wave laser excitation.[221]

As excitation of the silver solution shown above takes place in the IR regime, but emission is in the visible, a multiphoton absorption process is immediately suspected. To test this hypothesis, the emission spectrum was collected at a series of excitation powers, in which neutral density filters of known optical densities (OD) (0, 0.04, 0.38, 0.50 and 0.70 OD, resulting in excitation powers of 27.5, 25.1, 11.5, 8.7 and 5.5 mW, respectively) were placed in the excitation beam path. The resulting emission spectra are shown in Figure 4.5. It is clear that there is a non-linear decrease in intensity as the excitation power is decreased. To quantify this trend, the integrated intensity over the

entire spectrum was plotted against excitation power. OriginPro was used to obtain a best fit line of the form ax^b. The data and best fit line ($y = 14.889x^{2.115}$) are shown in Figure 4.6. With an exponent (b) of 2.115 (±0.096), it is clear that the excitation process is two-photon in nature.

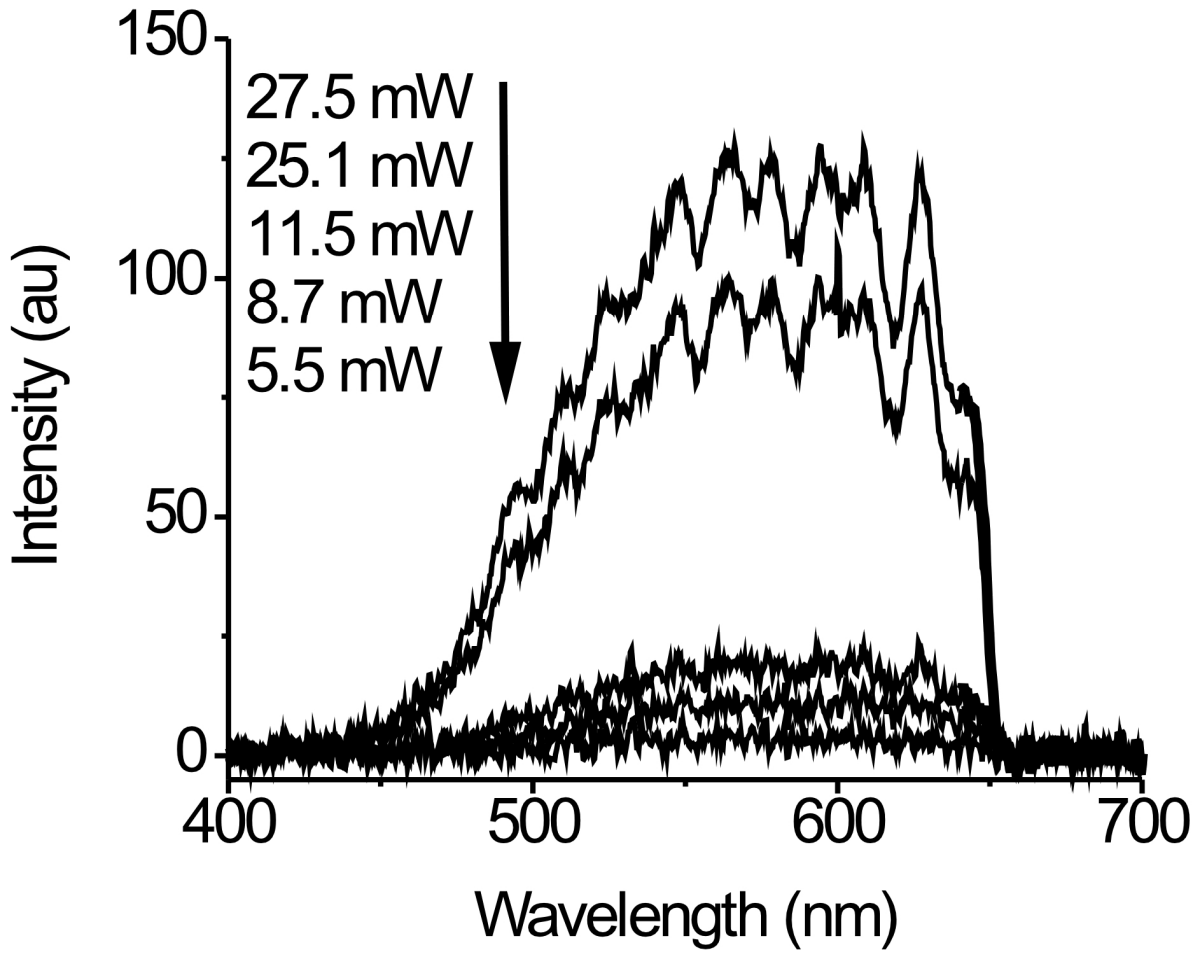

Figure 4.5. Two-photon induced luminescence of silver nanoparticle aggregates in solution. The emission spectra shown here were collected after a sample of aggregated silver nanoparticles in solution were excited by a Ti:sapphire laser at varying powers: 27.5, 25.1, 11.5, 8.7, and 5.5 mW (top to bottom).

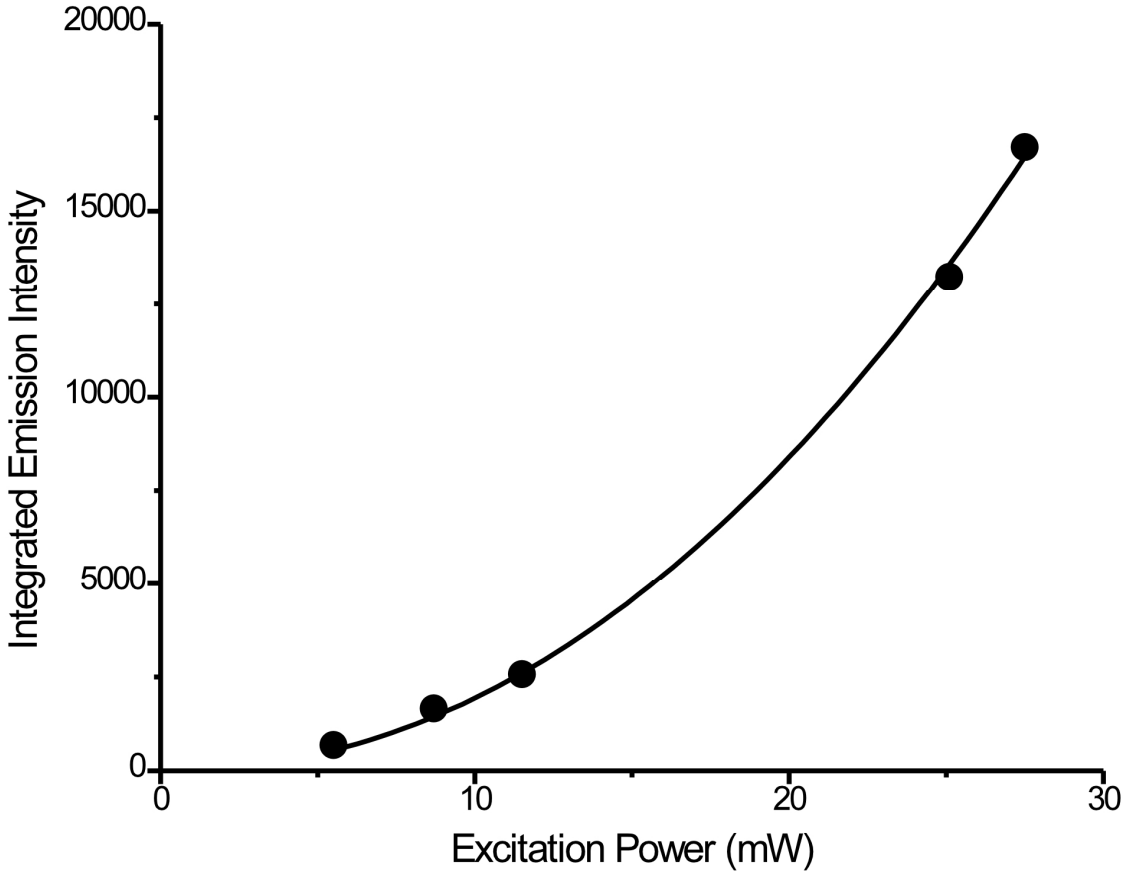

Figure 4.6. Integrated intensity of the spectra shown in Figure 4.5 plotted as a function of excitation power. Clearly not linear, a best-fit line (in the form of a power function, $y=ax^b$) was found to be $y = 14.889x^{2.115}$, indicating that the excitation process is, or is largely dominated by, a two-photon process.

To confirm this analysis, the data was then fit to a linear ($y=ax^1$, dashed line), quadratic ($y=ax^2$, solid line) and cubic ($y=ax^3$, dotted line) curves. The results are shown in Figure 4.7. With R^2 values of 0.8627, 0.9984, and 0.9842 for the linear, quadratic, and cubic fits, respectively, it is again clear that the relationship is quadratic, and the excitation process two-photon.

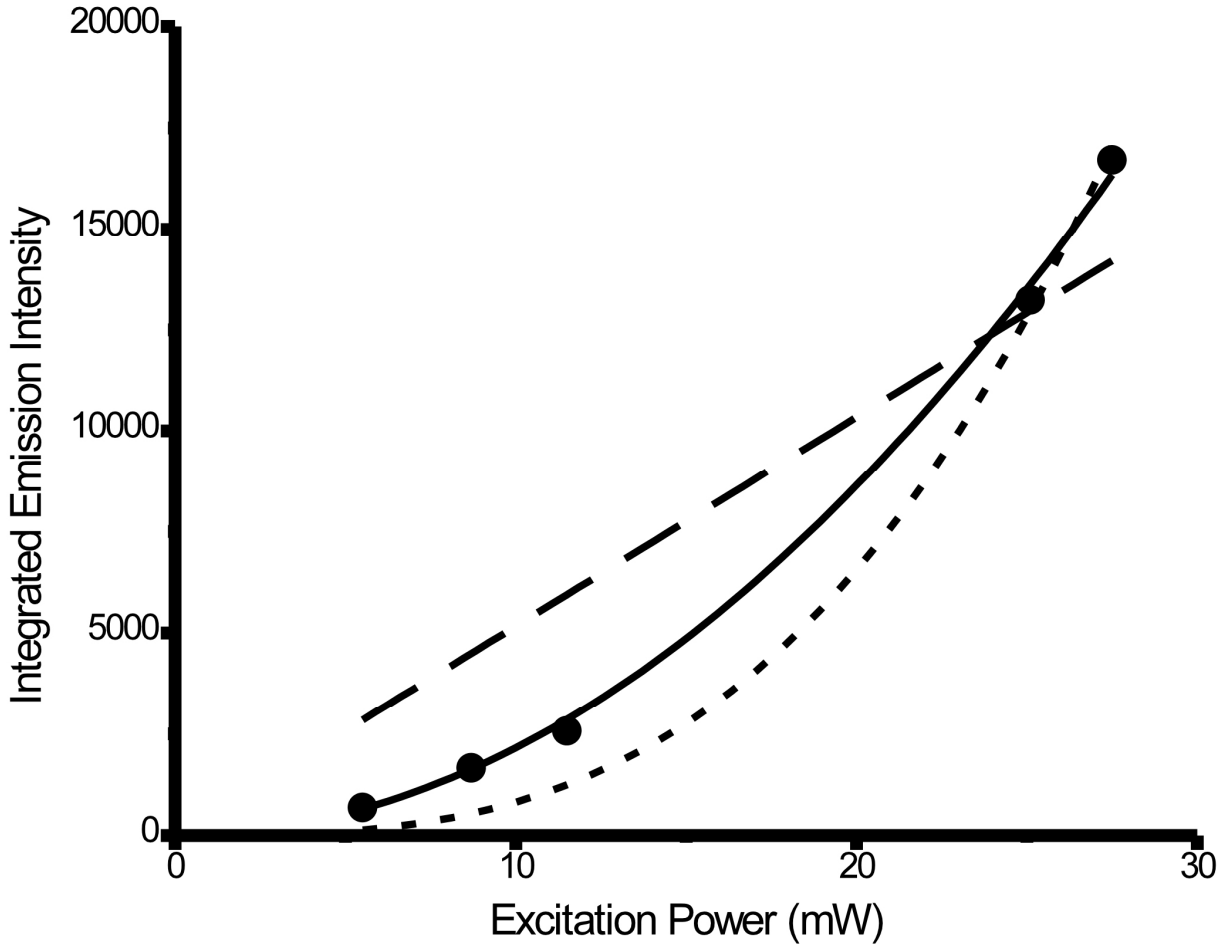

Figure 4.7. Integrated intensity of the spectra shown in Figure 4.5 plotted as a function of excitation power. Data is fit to linear ($y=ax^1$, dashed line, $R^2=0.8627$), quadratic ($y=ax^2$, solid line, $R^2=0.9984$) and cubic ($y=ax^3$, dotted line, $R^2=0.9842$) curves. From these results, it is again clear that the relationship is quadratic, and the excitation process two-photon.

4.4. Emission from Samples on the Substrate

4.4.1. Observation

When the Ti:sapphire laser discussed in Section 3.2.1 is focused at normal incidence onto the sample, emission from the nanoparticles at the focal spot is observed. This emission, which is solely from the focal spot, is referred to as "local emission." On certain samples, or regions of a sample, focusing of the Ti:sapphire laser results in minimal emission at or near the focal spot, but significant emission from a number of regions tens of micrometers away from the focal spot. It is this emission that is referred to as “remote” emission, and is the focus of the studies in this dissertation. A comparison of these two phenomena is shown in Figure 4.8.

In this figure, two samples were illuminated with a femtosecond laser under identical conditions. The panel on the right shows intense local emission with no remote emission, while the panel on the left shows emission about 30 times less intense, with visible regions of remote emission.

Discrete regions of emission have been observed and recorded as far as 99 μm from the focal spot, as shown in Figure 4.9. Under typical excitation conditions, stable, remote emission is routinely observed up to 20-40 μm from the focal spot. Under higher excitation powers, distances that are estimated to be greater can be observed by eye through the microscope objective, but are not stable, and cannot be documented due to the limited field of view of the collection camera.

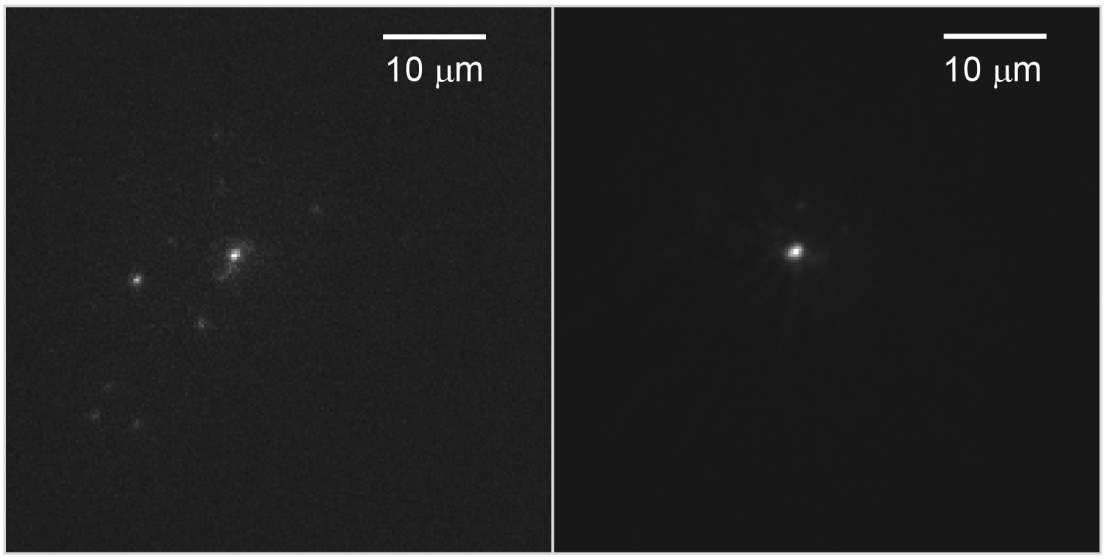

Figure 4.8. Comparison of two silver samples illuminated with a femtosecond laser under the same conditions. The sample on the left, which has a maximum intensity of 536 counts, shows distinct regions of remote emission. The sample on the right, which has a maximum intensity of 14,568 counts (nearly saturation) shows no evidence of remote emission.

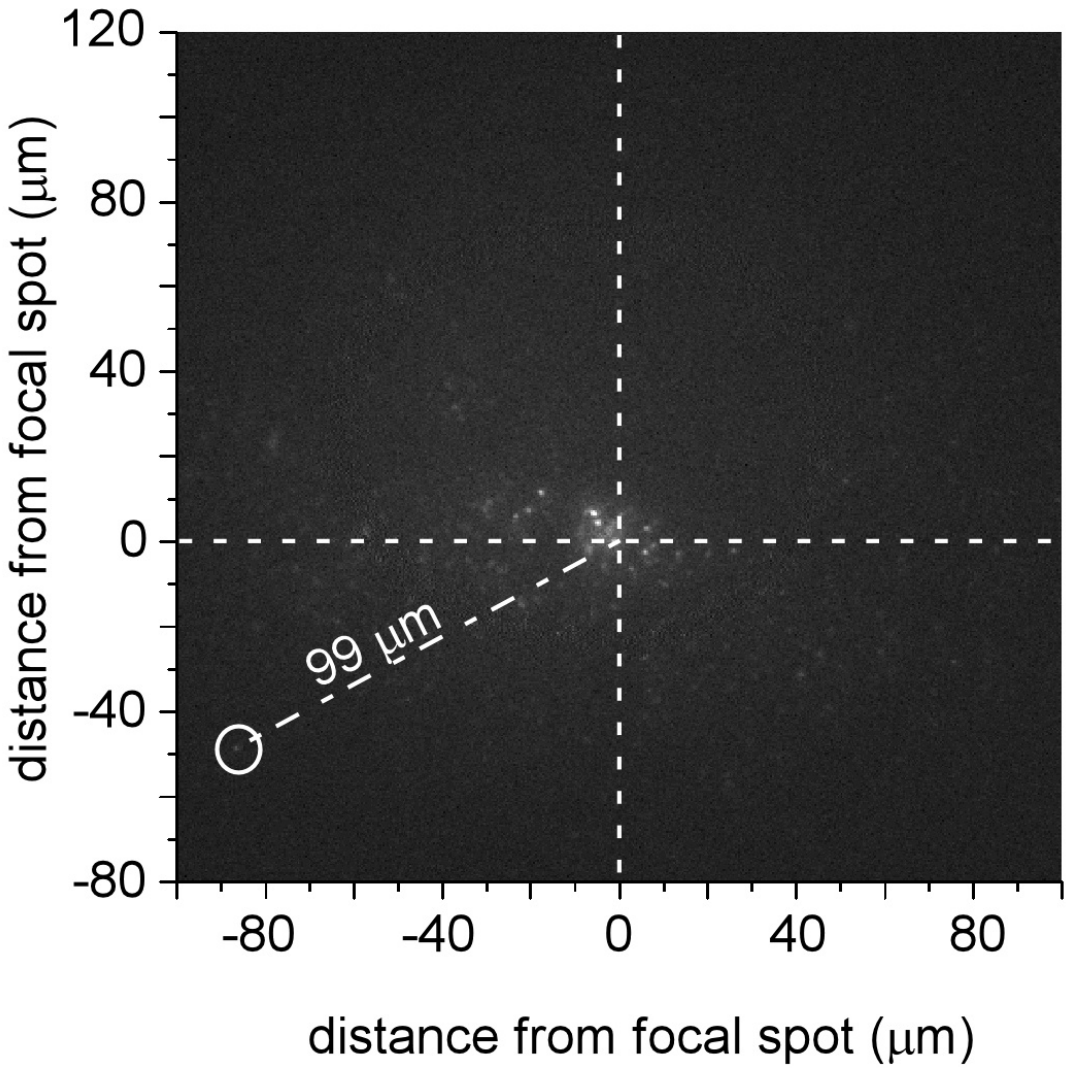

Figure 4.9. Emission that is up to 100 μm from the focal spot (denoted by cross-hairs) is observed when a dielectric substrate with silver nanoparticles is excited by a femtosecond laser at normal incidence. A 40x/0.60 NA objective was used in this experiment.

When excited at sufficiently low powers, the observed emission is stable for tens of minutes, allowing time to study its various properties as well as methods of control, as discussed in the following chapter. The definition of "sufficiently low" varies from sample to sample, but is typically ~1 mW. Focused down to a 1 μm spot size, typical for the 60x/1.45 NA objective, this results in a power of 11 pJ/pulse and peak intensities of

1.12×10^{11} W/cm^2. At lower powers, the signal to noise ratio significantly deteriorates, while at higher powers, the emission tends to be unstable.

4.4.2. Density of Particles

While the effect has not been quantified, a correlation between distance of remote emission and what defines a "sufficiently low power" for a sample, or section of a sample, has been observed. That is to say, a sample that shows extensive emission far from the focal spot will be more stable at higher powers than a sample that emits only in the region at the focal spot; in fact, it is nearly impossible to study emission that is confined to the focal spot due to the instability of the intense emission observed, even at very low (μW) excitation powers. This observation can be readily explained by the hypothesis that at least some of the instability is due to melting, or other permanent changes to the structure of the particle that affect its ability to resonate with the given frequency of excitation.[172-174,176-178] Samples that show remote emission have an additional mechanism to dissipate energy, and are therefore less likely to experience structural changes due to melting from high heat deposition.

When looking at samples, it is possible to visually gauge which sample, or regions on a sample, are more likely to show strong local or strong remote emission. Empirically, "darker," or more opaque samples or regions, in which there is heavier deposition of nanoparticles, tend to show localized emission, while "lighter," more transparent samples or regions are more likely to have extended regions of remote emission that are stable over long periods of time.

To systematically explore this phenomenon, a study was performed in which the amount of time a substrate remained in the precipitation chamber was varied, from a

quick dip (1 sec) to 48 hours. This allowed a more developed determination of the conditions under which different types of emission are observed. The results are shown in Figure 4.10. It should be noted that for this experiment, as for all experiments reported in this dissertation, the sample position must be fine-tuned using the stage to minimize local emission, even in a region of good “remote” emission.

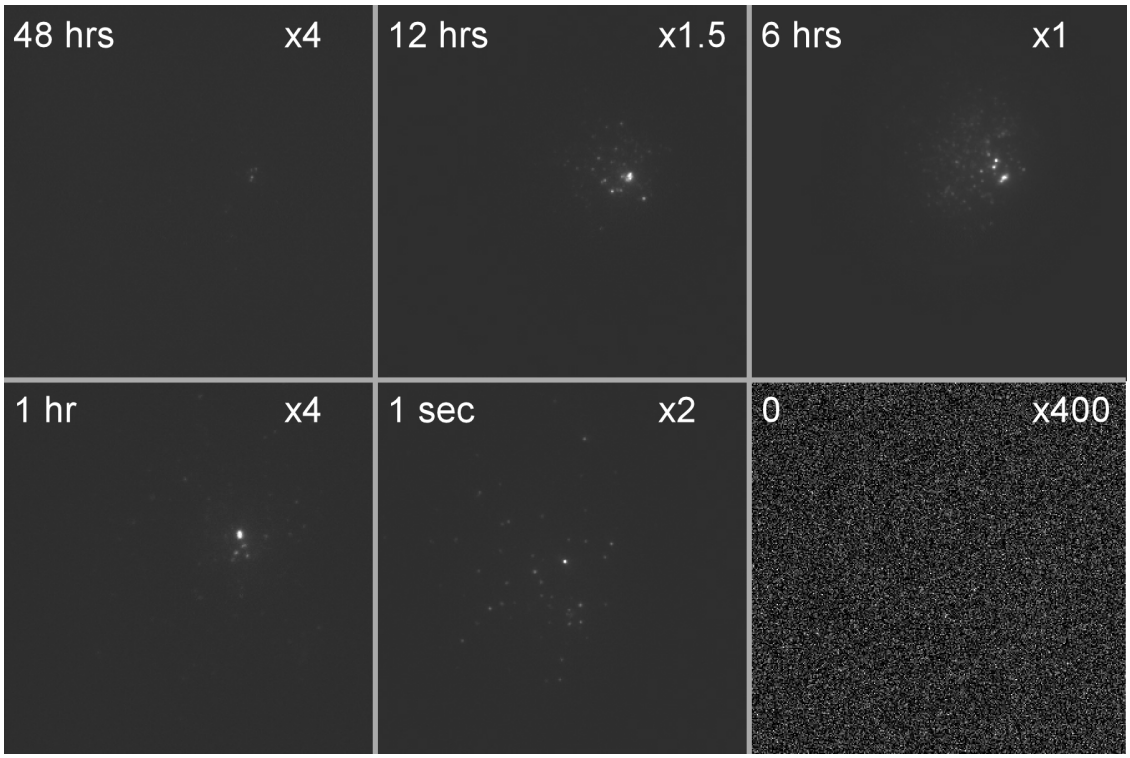

Figure 4.10. Effect of deposition time (and therefore particle density) on remote emission. Exposure time was 0.5 sec, average laser power was 2.95 mW, and the gain was set to 200.

At the highest deposition times (and presumably the highest particle density), the remote emission was relatively limited. At lower deposition times, the scope of the remote emission increases. At 1 hr, optimal remote emission is observed, although it is overshadowed in this image by emission near the focal spot. After just dipping the sample into the sample (1 sec), the most remote emission was observed. However, this

emission was less consistent; excitation of many areas of the sample did not result in emission strong enough to capture on the camera.

To explain these results, we have to consider that increasing density will result in an increased number of paths for energy to transfer through. After a very short deposition time, there will be very few nanoparticles on the surface, and therefore few paths for the energy to transfer through. As the density of nanoparticles increases with increased deposition time, there will be more connectivity within the sample, and therefore a greater likelihood of remote emission taking place. As the density continues to increase, the paths will become less distinct. The entire surface will more closely resemble a rough surface, with the energy localizing at the focal spot.

It should be noted that this study is limited only to identifying the deposition times leading to the best emission for this "batch" of samples. In general, batch-to-batch comparisons lead to as wide of range as results as shown within this batch, a phenomenon that has been seen elsewhere, as well.[42] This is likely due to the wide range of environmental factors that affect nucleation and aggregation in the growth of the nanoparticles. A retrospective view of the data suggests that better remote emission tends to come from samples prepared in the summer, when the laboratories are cooler and much more humid, versus the winter, when the laboratories are warmer and much more dry. Other factors, such as the amount of water evaporated during boiling, rate of cooling, etc. make the effect of humidity and temperature difficult to isolate, however.

4.5. Characterization of Sample on Substrate

4.5.1. Multiphoton Behavior

To confirm that the luminescence observed on the substrate is due to a multiphoton absorption, as was shown in solution, a variable filter with a linear optical density gradient was placed in the laser beam path after it was collimated but before it was expanded. The experiment was performed by moving the variable filter along the gradient, collecting an image and then collecting the spectrum of the laser. This was repeated 100 times, with every tenth data point (5, 15, 25, etc.) an image collected with the beam blocked to check for drift in the background, and every tenth data point on the tens (0, 10, 20, etc.) collected at full laser power. While this did increase the possibility of damaging the sample, it also allowed for a check of drift in laser intensity, as well as in response of the sample. The results presented here are for a sample that showed no evidence of damage or drift of either sort.

To aid in analysis, both the laser spectrum and the power were collected at several different laser intensities, and the linear relationship between the integrated intensity of the spectrum and the laser power quantified. This relationship was then used to transform the integrated intensity of the collected spectra to the power of the excitation beam.

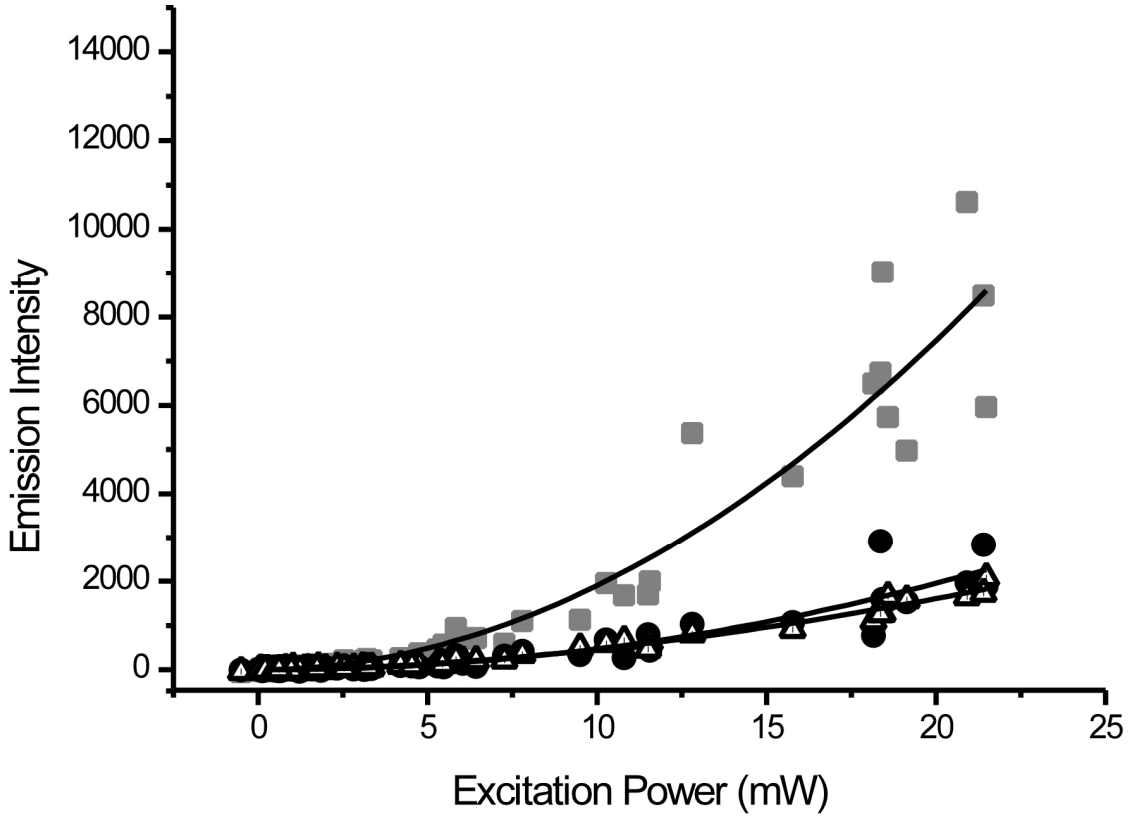

Figure 4.11. Integrated intensity of individual data points plotted as a function of excitation power. The lines of best fit were found to be $y=20.4x^{1.970}$ (gray squares), $y=4.16x^{2.054}$ (solid circles) and $y=7.53x^{1.790}$ (open triangles).

After discarding images collected with a fully blocked beam, or in which any pixel was saturated, the remaining data was used to analyze the power dependence of individual points of emission. The intensity of individual regions of emission was plotted versus the excitation power, and the data fit to a power function, as it was for the

solution data. A plot of the power dependency of three representative data points is shown in Figure 4.11. Using OriginPro for data fitting, exponents of 1.970±0.085 (gray squares), 2.054±0.344 (solid circles) and 1.790±0.340 (open triangles) were found, indicating that, as with the solution, the emission process is due to a two-photon absorption.

To further confirm these results, particularly given the noisiness inherent to the data, an analysis similar to that presented in Section 4.3.2 (and Figure 4.7, in particular) was performed, and the data from each region of emission was fit to linear, quadratic and cubic curves. The R^2 values for each of these fits is shown in the table below.

Table 2. Comparison of R^2 Values for Linear, Quadratic, and Cubic Fits of Data in Figure 4.11.

Data Set	Linear	Quadratic	Cubic
gray squares	0.8132	0.9250	0.8919
solid circles	0.7777	0.8892	0.8667
open triangles	0.8911	0.9783	0.9330

4.5.2. Spectral Information

To further characterize the emission from the particles when on the substrate, red, green and blue-pass (>600 nm, 500-575 nm, and <500 nm) filters were placed between the microscope and the detector. A composite image is shown in Figure 4.12. It can be seen that a substantial component of the emission is in the 500-575 nm range, with some emission >600 nm, and virtually no emission below 500 nm. This is consistent with the aggregate solution spectra shown in Figure 4.5.

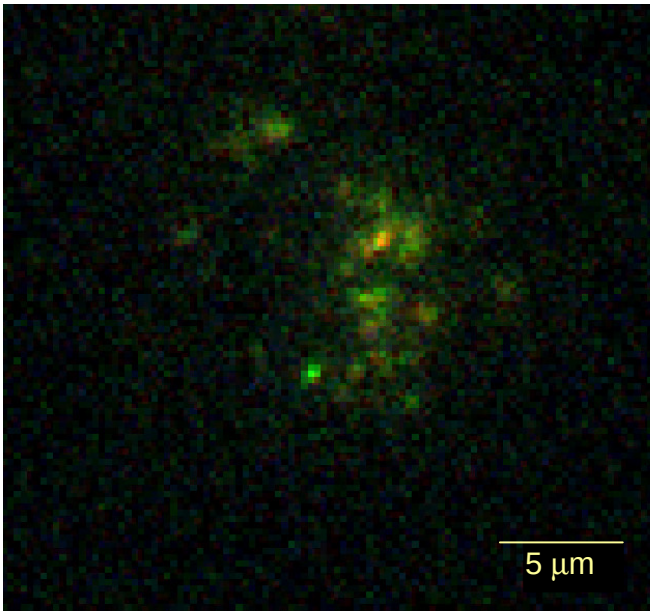

Figure 4.12. Composite image of remote emission collected with colored filters. Signal having wavelengths between 600 and 650 nm, wavelengths between 500 and 575 nm, and wavelengths less than 500 nm are false colored red, green and blue, respectively. For interpretation of the references to color in this and all other figures, the reader is referred to the electronic version of this dissertation.

More refined insight into the spectral properties of the sample was gained by placing an electronically controlled variable color filter (VariSpec Filter 51010, CRi) immediately before the camera. This device allows only a narrow band of wavelengths (10 nm FWHM) to pass. By scanning the transmission wavelength, a spectrum of the emission can be acquired. A false color composite image is shown in Figure 4.13, left. Emission from 450-525 nm is colored blue, 525-600 nm green, and 600-675 nm red. It is clear that different regions have distinct wavelengths of emission. Figure 4.13, right, shows the spectra of the three circled regions of emission. From these spectra, several properties of the emission can be determined. First, there is no emission below 450 nm, so the observed emission cannot be second-harmonic generation of the fundamental excitation beam. Second, there is no emission above 650 nm, showing

that the dichroic mirror used to separate the excitation from the emission is effective, and that the observed emission cannot be attributed to direct scatter of the fundamental of the excitation laser beam. Third, the spectra illustrate that the particles have emissions with different line shapes and line widths. Region A (red, circles) has a narrow band of emission around 610 nm, region B (blue, crosses), has a strong, slightly broader emission around 510 nm, while region C (green, squares) has a very broad emission. The spectrum of region A has been multiplied by 5 to make it clearly visible on the same axes as B and C. Figure 4.14 is another false color spectrally resolved image of nanoparticle emission, over a wider field of view. Emission from 440-510 nm was colored blue, 520-590 nm green, and 600-670 nm red. It is again clear that different regions of emission have distinct wavelengths of emission across the entire visible spectrum.

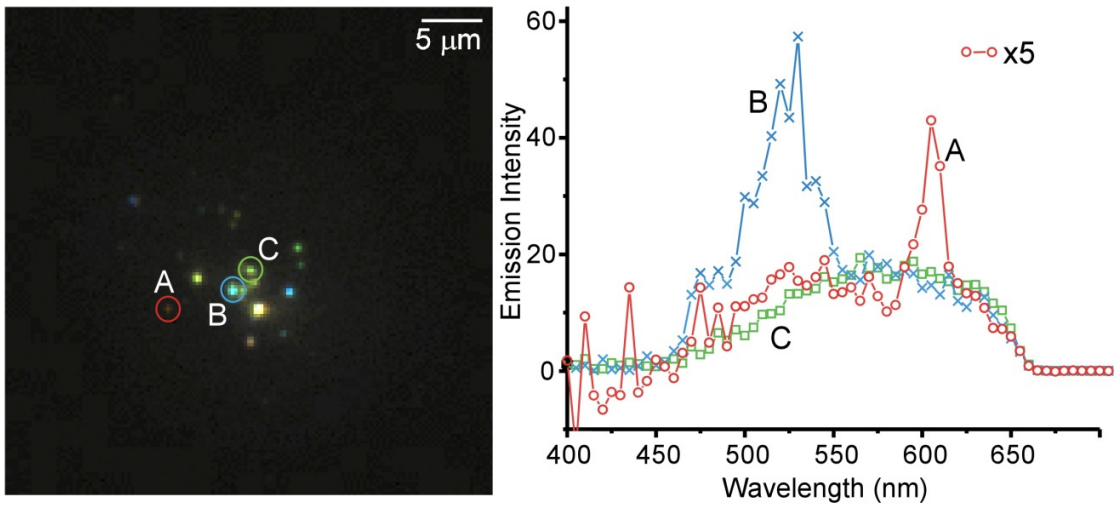

Figure 4.13. Left. False color composite image of spectrally resolved silver nanoparticle emission. Emission from 450-525 nm is colored blue, 525-600 nm green, and 600-675 nm red. Right. Spectra from the three circled regions in the left panel are shown. The signal from region A (red, circles) has been multiplied by 5 to make it visible on the same set of axes as regions B (blue, crosses) and C (green, squares). Note that there is no emission detected about 650 nm, consistent with the filters used, nor is there emission below about 450 nm, again showing that the emission is not second-harmonic generation.

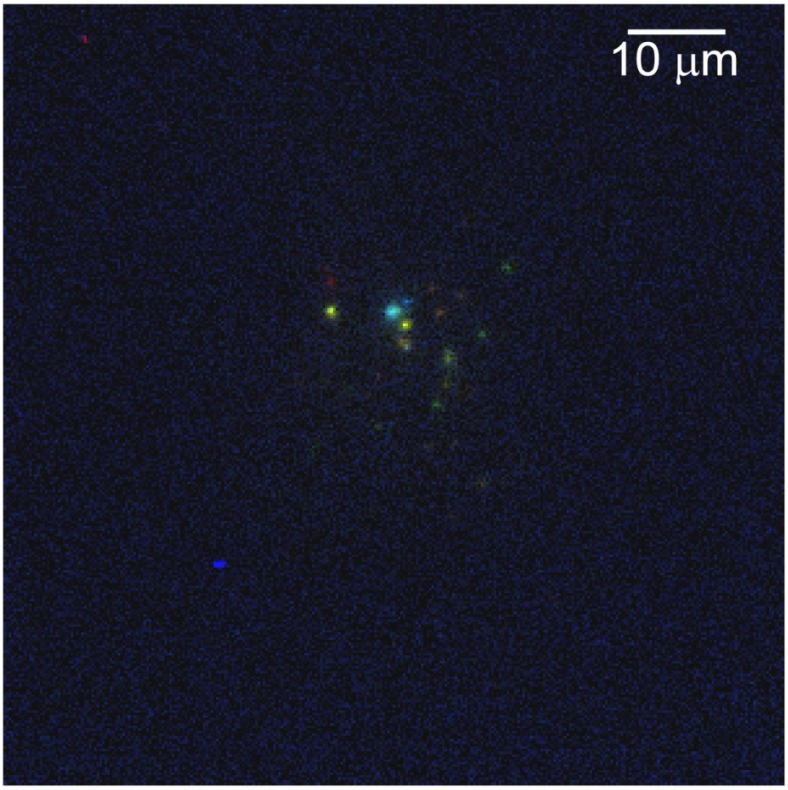

Figure 4.14. False color spectrally resolved image of nanoparticle emission. Emission from 440-510 nm was colored blue, 520-590 nm green, and 600-670 nm red. It is again clear that different particles have distinct wavelengths of emission across at least the entire visible spectrum.

4.6. Polarization

The propagation of electromagnetic fields as SPPs is known to be polarization-dependent, and the resulting localized and amplified electromagnetic field polarized, both on rough surfaces[51,222] and on individual non-spherical nanoparticles.[215] Additionally, the intensity of luminescence and second-harmonic generation from irregular surfaces[52,213,223-225] is sensitive to the polarization of excitation. Therefore, we examined both the polarization of emitted light, as well as the ability to change which regions emit based on the polarization of the excitation beam.

To control the polarization of the excitation beam, a Berek compensator, configured to act as a half-wave plate, was placed in the laser beam path after the shaper, but before the telescope. A thin linear polarizer was placed immediately before the camera so that only light of a particular polarization is recorded.

The results of this experiment are shown in Figure 4.15. Each panel of Figure 4.15 is a wide-field image of the same area under different polarization conditions for excitation and emission. The top panels were excited with a beam of 45º polarized light, while the bottom panels were excited with a beam of 135º polarized light. Horizontally polarized emission was detected in the left panels, and vertically polarized emission was detected in the right panels. It can be seen from this figure that the emission is polarized, with the regions not all having the same emission polarization. For example, the area in region A emits distinctly vertically polarized light for both excitation polarizations, while the area in region C only emits horizontally polarized light. Additionally, polarization of the excitation beam can be used to control the presence or absence of emission in certain spots. This is clearly illustrated by the areas in regions D

and E, which only emit upon excitation with 135º polarized light, but not under excitation with 45º polarized light. Region C clearly shows that the excitation and emission polarizations are separated, as emission is only seen upon excitation with 135º polarized light, but that emission is clearly vertically polarized, with no horizontally polarized emission seen. Were the emission polarization to match the excitation polarization, we would expect to see approximately equal intensities for detected vertical and horizontal polarization.

4.7. Conclusions on Luminescence

The luminescent phenomena observed in this chapter is consistent with two-photon-induced luminescence of the silver nanoparticles, enhanced by the LSPR effect. Based on spectral information, the emission is clearly not scattered fundamental or second-harmonic generation, as no 800 nm or 400 nm emission is observed. Additionally, it is observed that regions of emission as close as 1 μm can display different spectral and polarization properties, suggesting that energy transfer to each region of emission, which will be discussed in the next chapter, is an independent process.

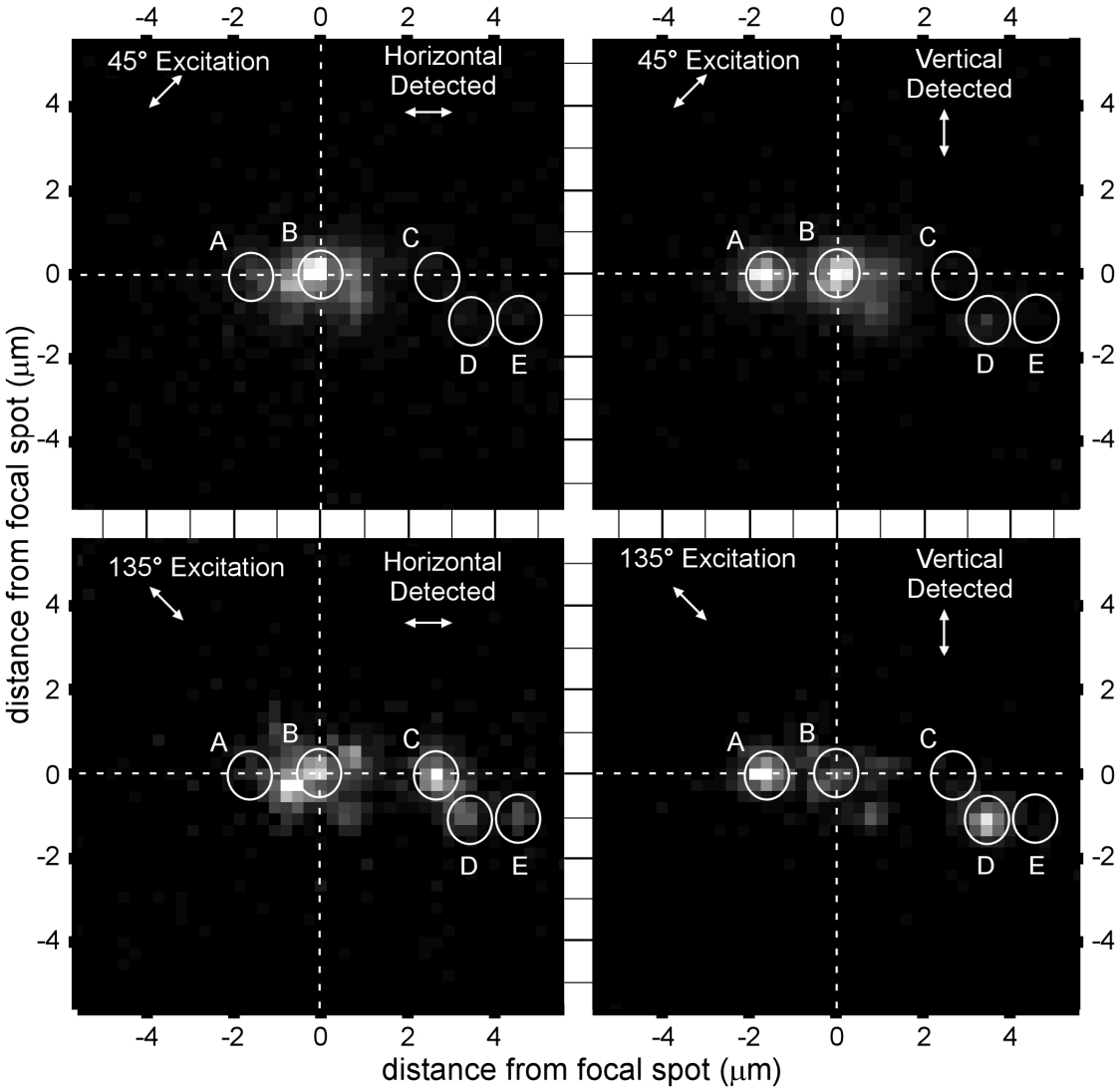

Figure 4.15. Polarization characteristics of the silver samples. Each panel is of the same area under different excitation and detection conditions. The top panels are excited with 45° polarized light, and the bottom panels with 135° polarized light. Horizontally polarized light was collected in the left panels, and vertically polarized light was collected in the right panels. This figure illustrates that the observed two-photon induced luminescence is polarized, as the area in the Ring A shows, and that emission can be controlled by the incoming polarization, as shown by the area in Rings C and D.

5. CHARACTERIZATION OF ENERGY PROPAGATION

While the previous chapter discussed the characteristics of the emission observed, this chapter takes the observation a step further and seeks to understand the nature of the propagation of energy, as well as how the intensity of the luminescence can be controlled. This information serves two purposes. First, it provides further insight into the physics behind the observed phenomena. Secondly, being able to control the propagation and subsequent enhancement of the electromagnetic field is critical for the development of future applications.

5.1. Further Discussion of Scattering

In the previous chapter, it was discussed that the spectral properties of the samples were consistent with two-photon-induced luminescence, and not scattered fundamental or SHG. Here, the comparison with scatter is explored further detail, with an emphasis on the transport, as opposed to the emissive, properties.

In this experiment, a sample was alternately illuminated by the femtosecond laser and a HeNe laser at 632 nm, which was configured to propagate collinearly through the same optics, and thus focus at the same point. This wavelength is short enough (<650 nm) that it is not blocked by the dichroic mirrors and filters that prevent the observation of scattered light from the fs-laser, and allows characterization of the behavior of such light in this sample.

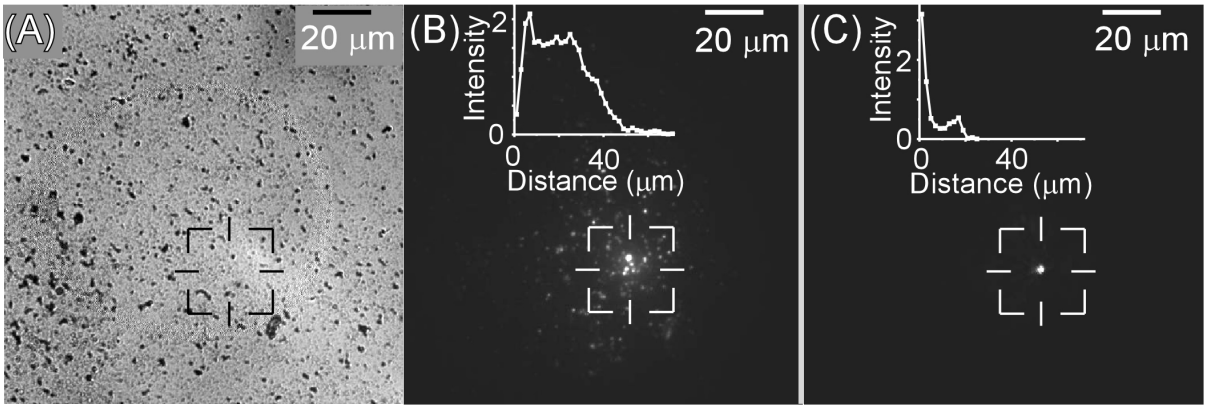

Figure 5.1. Images of a single sample under different types of illumination. Panel A shows a sample under white-light illumination. Panel B shows the same sample excited at the crosshairs by a 13-fs Ti:sapphire laser, while Panel C shows the sample excited at the crosshairs by a HeNe laser. The insets in Panels B and C show the total intensity of all pixels with signal above the noise level as a function of distance from the focal spot. It is clear that the behavior observed upon excitation with a fs-laser is not consistent with the behavior of scatter observed upon excitation with a HeNe laser.

An image of the sample collected under white light illumination is shown in Figure 5.1A. The image shown in Figure 5.1B corresponds to the same sample shown in Panel A when it is excited by ultrashort laser pulses focused down to 1 μm spot size located at the cross-hairs, while the image shown in Panel C shows the sample when excited with the 632 nm HeNe laser. The inset in each shows the total luminescence from the sample as a function of distance from the excitation point, in 2 μm increments. It is clear that the remote regions of luminescence observed upon excitation by the fs-laser (B) are not consistent with the scattering behavior observed upon excitation with the HeNe laser (C).

To further characterize the behavior of the emitted light, and compare what is observed upon excitation with a fs-laser to the scatter observed upon excitation with a HeNe laser, the intensity of 2 μm-wide cross-sections running horizontally and vertically through the focal spot are plotted in Figure 5.2. From this figure, it is strikingly clear that

the behavior observed upon excitation with the fs-laser is not scatter. The overall spatial profile of the photoluminescence is much broader, with clearly discrete regions of emission (shown by sharp spikes). When scatter is detected, no such discrete regions are observed. Another significant observation is that the maximum intensity for the fs-laser excited sample is not found immediately at the focal spot. This is consistent with numerous observations, in which very strong emission at the focal spot correlated with a lack of discrete regions of remote luminescence; i.e., strong emission at the focal spot is indicative of poor energy transport, a phenomenon discussed in detail in Section 4.4.

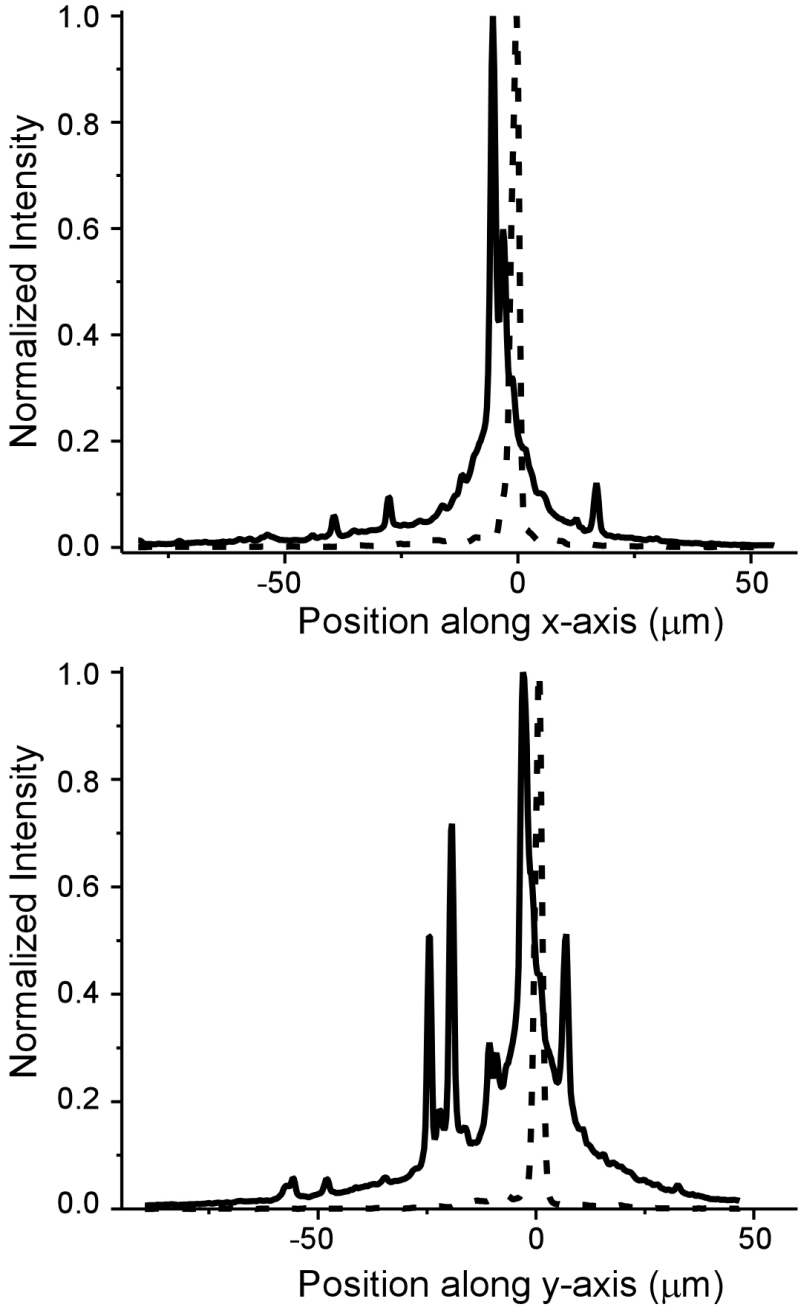

Figure 5.2. Intensity profiles for a 2μm-wide section of data running horizontally (top) and vertically (bottom) through the focal spot for a sample excited by a HeNe laser (dashed line), and a fs-laser (solid line).

5.2. Autocorrelation

In order to investigate the nature of energy transport in these samples, the pulse shaper (described in detail in Section 3.2.2) was programmed to produce a pair of pulses and to scan the delay between them.[226,227] Although similar types of experiments have been reported in the literature,[228-232] the experiments presented here are different from those, as our excitation is in the near-IR, which then propagates, and the measured signal corresponds to localized two-photon-induced photoluminescence and not to photoelectrons, as, for example, in Ref. 233.

Figure 5.3 shows the intensity of photoluminescence from individual regions of the thin film as a function of time delay between the two pulses. Because the two pulses are collinear, they interfere with each other. The top panel shows the signal obtained from a frequency doubling crystal for reference. The 2.67 fs oscillations correspond to the optical period of the fundamental laser wavelength. A representative image is shown at left, and the intensities of the three circled points, as a function of the delay between pulses, are shown to the right.

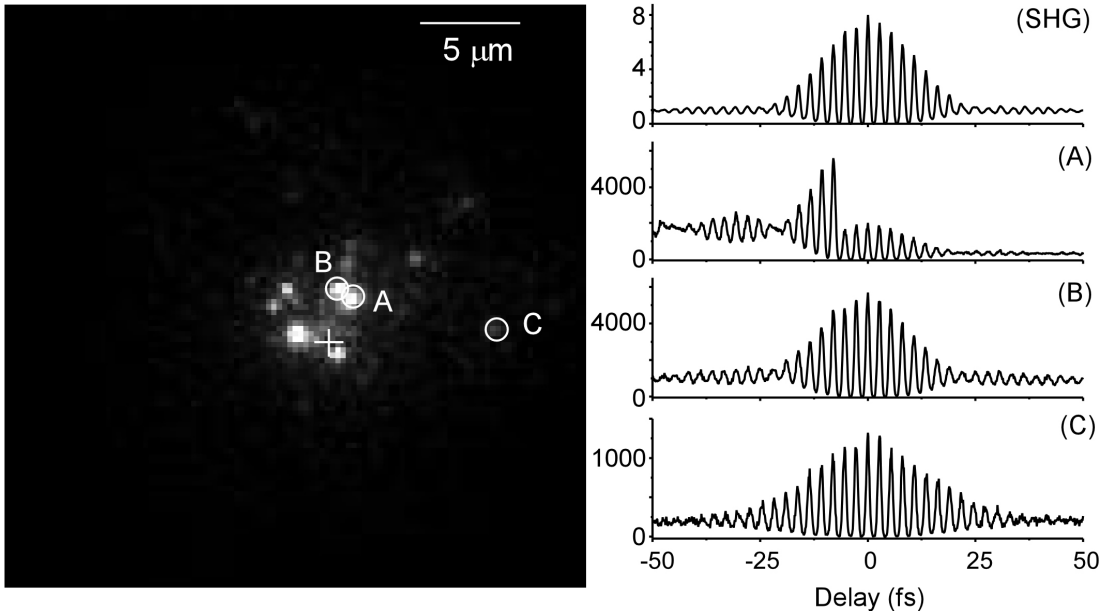

Figure 5.3. Photoluminescence from several discrete regions is shown as a pulse shaper is used to produce a pair of pulses and scan the delay between them. The top panel shows the optical response of a frequency doubling crystal as a function of delay between pulses. Panels A, B, and C show the optical response from different regions. Some regions show broadening, as shown in region C. Others show wings (visible in panel B), or erratic behavior, likely due to melting or other irreversible change to the sample, as shown in panel A. The behaviors are independent of distance from the excitation point, as well as the behavior of neighboring regions (compare regions A and B, which are only separated by approximately 1 μm).

Of first note is that the period and overall shape of the photoluminescence from the various regions, particularly region B, correspond well with the second-harmonic signal, which is further evidence that the behavior observed is two-photon in nature. Further insight can be gained by examining the behavior of each individual region. Over the course of the autocorrelation, it has been observed that some regions will spontaneously stop emitting. Of these, some will later be observed to emit with the same properties observed before, in a blinking phenomenon. Others will remain “off.” The behavior of those regions, and others that exhibit an irreversible change in behavior, such as region A, are attributed to structural changes to the sample upon

irradiation, with melting of the sample[174,177,178] a likely cause. It is also significant to note that adjacent regions, such as A and B, which are separated by approximately 1 μm, can exhibit very different behaviors. In this case, region A exhibits an abrupt change in intensity, while region B exhibits no such change. This indicates that the regions respond independently to the laser used for illumination, and further indicate that no sequential scattering is taking place.

Other behaviors are also observed in the optical response, including broadening (region C) of the pulse, which indicates that quadratic dispersion has been acquired as the SPP propagates. Side-peaks, visible in the signal from region B and more pronounced in other regions, suggest that cubic dispersion is also acquired by the excitation pulse as it propagates to the regions where localized two-photon-induced luminescence occurs.

Clearly, there are significant differences in the luminescent properties of different regions of the sample while an autocorrelation is performed at the focus. While the implications of some of these observations are not immediately clear, the observed broadening and presence of side-peaks in the traces are consistent with the behavior expected if the pulse experienced dispersion as it propagated through the sample. As each region of photoluminescence results from energy traveling along a different path, it would be expected to find evidence for pulse broadening due to dispersion (chirp). Pulse broadening in our measurements indicate that the propagating SPP experiences different amounts of dispersion as it travels to the region where it induces two-photon photoluminescence, a concept we explore further below.

5.3. Dispersion

As a control strategy, a series of measurements using shaped laser pulses were performed. The Dantus group has developed a number of strategies to control nonlinear optical excitation based on phase-shaped femtosecond laser pulses.[141,142,144,234,235] Here we explore the influence of phase-shaped pulses on the intensity of the two-photon-induced luminescence from the silver.

5.3.1. Sensitivity to Phase: Sine Function

Figure 5.4 shows three wide-field images of a region (bottom panels) obtained using different sinusoidal phase functions of the form $1.5\pi \sin(12\omega - \delta)$ (top panels) applied across the spectrum of a laser pulse that has been compensated for previously existing phase distortions by MIIPS. The frequency, ω, is in fs^{-1}. In these images, only the value of δ (in rad) is varied from panel to panel. It can be seen by the bottom images that the intensity of emission of different regions is, indeed, sensitive to the spectral phase applied to the pulse; see, for example, the three circled regions of emission, each of which exhibit a maximum intensity under different phase conditions.

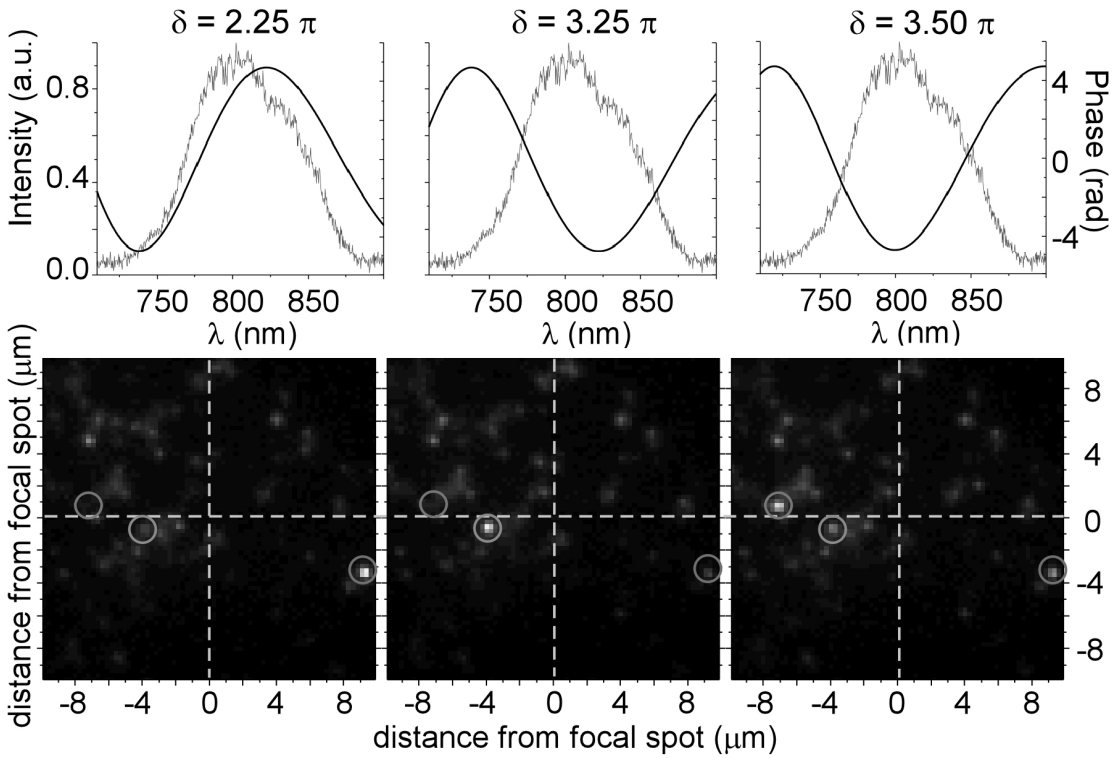

Figure 5.4. Phase control of remote emission. Each lower panel is a wide-field image of the same region of the sample, with the focal spot at (0, 0). The phases (black line) applied across the spectrum of the pulse are shown above each image. The circles highlight regions of interest and are at the same position in each panel.

To further explore the spectral phase dependence of emission, the intensity of individual regions of emission were plotted as a function of δ as it was scanned from 0 to 4π. The results for three different regions of emission are shown in Figure 5.5. As suggested by Figure 5.4, the dependence of the intensity of emission on applied spectral phase is different for different regions. However, not only do the locations of the intensity maxima vary, but the overall profile of the intensity dependence on phase varies as well.

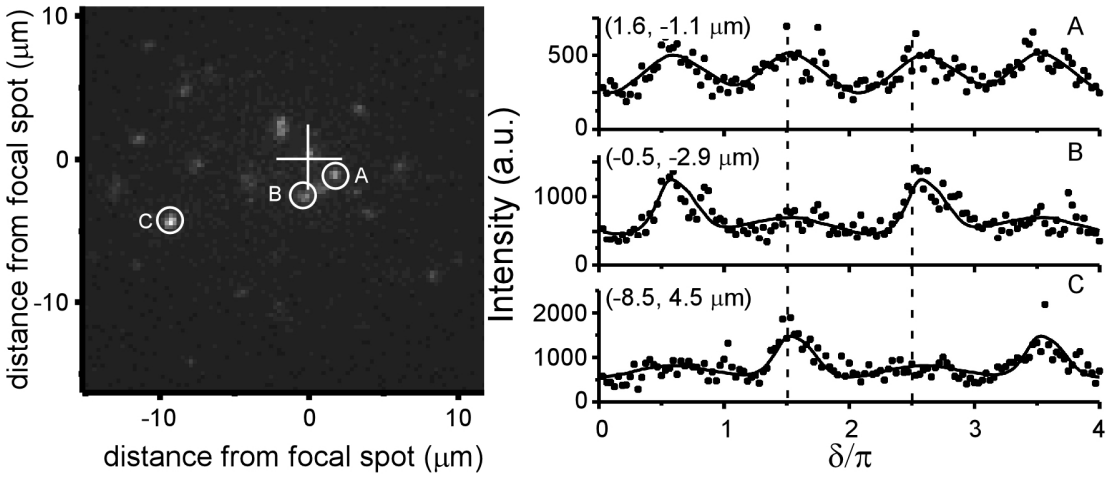

Figure 5.5. Control of emission intensity by spectral phase. The dots in panels A, B and C show the experimental intensity of the three labeled regions as a function of δ, when the applied phase is $1.5\pi \sin(12(\omega-\omega_0) - \delta)$. The solid line shows the simulated second-harmonic generation intensity optimized to fit the data by adjusting the second- and third-order dispersion of the pulse.

Given the use of a sinusoidal phase function of the same form utilized in MIIPS, it is not surprising to note that the intensity profiles resemble the integrated intensity of MIIPS traces of uncompensated pulses, and further suggesting that the profiles could be due to dispersion acquired by the SPP as it propagates through the sample. In order to explore this idea, simulations of the integrated intensity of second-harmonic generation as a function of sinusoidal phases of the form $1.5\pi \sin(12(\omega-\omega_0) - \delta)$ were performed, and shown in Figure 5.6. For an ideal pulse with no phase dispersion, the SHG intensity results in four evenly spaced peaks of equal height, located at $\delta = \pi/2$, $3\pi/2$, etc. as the value of δ is scanned from 0 to 4π, very similar to the behavior shown in region A in Figure 5.5.

The first hypothesis as to the source of the alternate behaviors of regions B and C was that the effective carrier frequency, ω_0, had changed, either by loss of the red or

blue component of the spectrum during propagation, or by varying absorption spectra in the regions of emission. However, simulations show that a shift in ω_0 results only in a shift of the intensity profiles, with no change in spacing or relative peak heights, as shown in Figure 5.6, top, in which the dotted line shows a simulation in which λ_0 = 825 nm, instead of 800 nm. This is not consistent with the observed behaviors. A second hypothesis is that the SPP acquires dispersions as it propagates, and that this dispersion affects the phase-dependent behavior of the luminescence. As each region of emission results from energy traveling along a different path, it would be expected that different regions would reflect the acquisition of different dispersion (chirp). Panel B shows the integrated intensity of simulated SHG spectra with 100 fs^2 of quadratic dispersion (broken line) and 1000 fs^3 of cubic dispersion (dashed line). It can be seen that quadratic dispersion affects the spacing of the peaks, while cubic dispersion affects the relative peak heights, and, less noticeably, peak spacing. If both quadratic and cubic dispersions are present, arbitrary profiles of spacing and peak height are seen, as shown in Panel C.

With this in mind, simulations of SH generated by a pulse with a sinusoidal phase function and quadratic and cubic dispersion were fit to the raw data in Figure 5.5, and the best-fits are shown as solid lines. It is found that region A experiences -70 fs^2 quadratic dispersion and -150 fs^3 cubic dispersion, region B experiences -150 fs^2 quadratic dispersion and +3500 fs^3 cubic dispersion, and region C experiences +20 fs^2 quadratic dispersion and -3500 fs^3 cubic dispersion.

The data shown in Figure 5.5 was collected over a period of several minutes, necessitating low excitation powers to ensure the sample is not damaged. This low excitation power, while permitting longer-term data collection, reduces the signal of the detected emission, resulting in noisy data and introducing error, estimated at ±50 fs^2 and ±1000 fs^3 for the data with the lowest signal-to-noise ratio, into the fits. However, it is important to consider that there is no ambiguity as to the sign of the quadratic and cubic dispersion. That is, there is a clear difference in the shape of curves when comparing, for example, +100 fs^2 and -100 fs^2 of quadratic dispersion and/or +5000 fs^3 and -5000 fs^3.

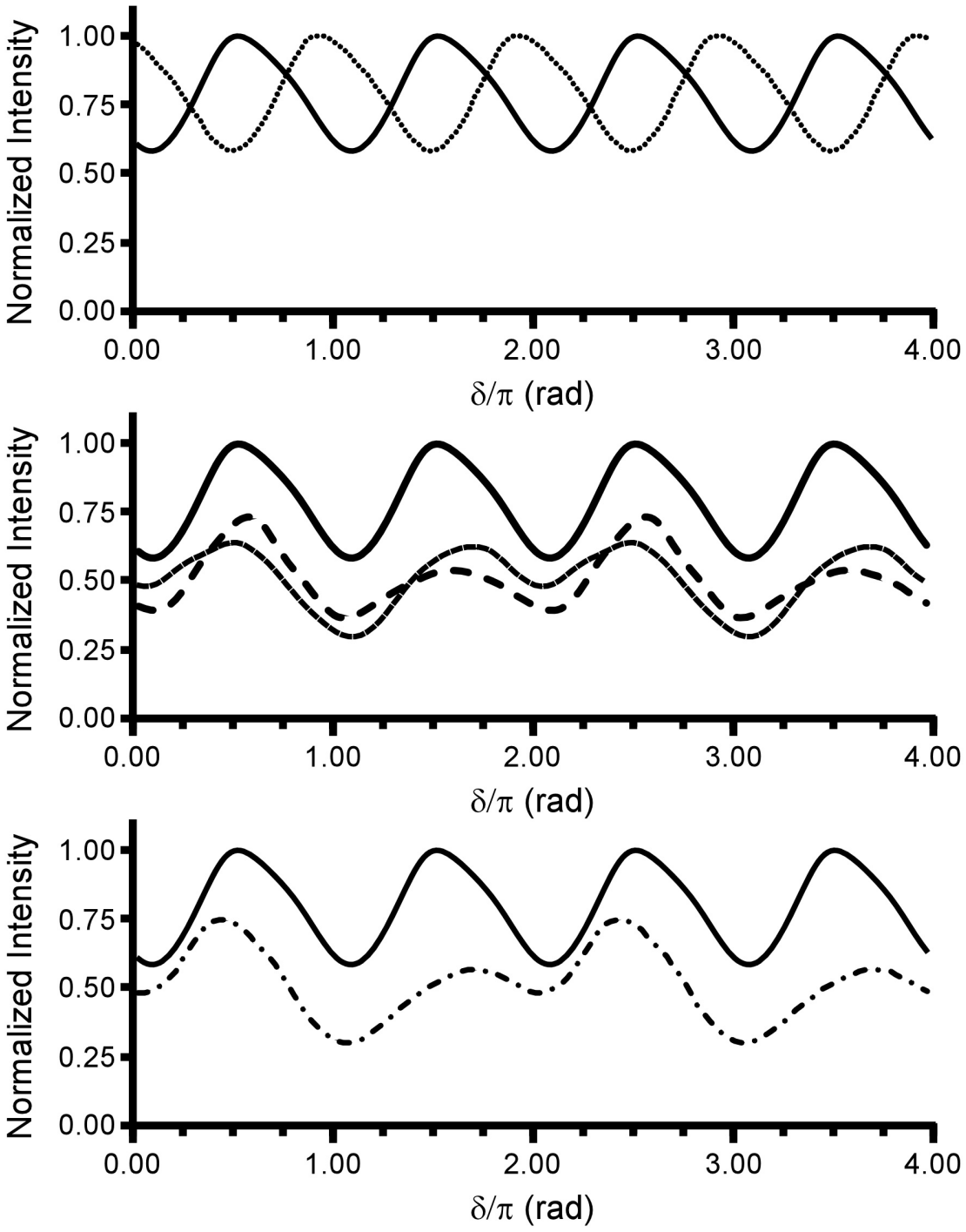

Figure 5.6. Simulations of the intensity of SH generation as a sinusoidal phase of the form $1.5\pi \sin(12(\omega-\omega_0) - \delta)$, is applied across the spectrum of the pulse.

Figure 5.6, con't.
In all panels, the solid line shows the intensity as the phase is applied to a TL pulse with a carrier frequency, $\omega_{0,}$ that corresponds to the carrier frequency, λ_0=800 nm. Panel A shows how the intensity profile changes with a shift in effective carrier frequency; the dotted line shows the intensity if the carrier frequency corresponded to $\lambda_{0,eff}$ = 825 nm. Panels B and C show the simulations of the intensity of SH generation if the sinusoidal function is applied to a non-TL pulse. In panel B, the broken line corresponds to a pulse with a dispersion of 100 fs^2, while the dashed line corresponds to a pulse with a dispersion of 1000 fs^3. Note that the second order dispersion results in unequal peak spacing, while third-order-dispersion results in unequal peak heights. In panel C, the simulations show the intensity as the sinusoidal function is applied to a pulse with both 100 fs^2 and 1000 fs^3 dispersion.

5.3.2. Quantifying Dispersion

To directly quantify the amount of quadratic and cubic dispersion acquired by the pulse as it propagates, a grid of phase functions of the form $\varphi(\phi'', \phi''') = \frac{1}{2}[\phi''(\omega-\omega_0)^2] + 1/6[\phi'''(\omega-\omega_0)^3]$, where ϕ'' and ϕ''' are the quadratic and cubic dispersions, is applied, and intensity of two-photon induced emission from discrete regions on the sample recorded. Assuming that maximum emission from a particular region occurs when the pulse is transform-limited ($\phi''=\phi'''=0$), the chirp introduced by the waveguide can be directly determined: $\phi''_W = -\phi''_{max}$ and $\phi'''_W = -\phi'''_{max}$.

To demonstrate and validate this approach, a control experiment was run in which frequency integrated SHG emission spectra were collected as a function of phase. First, the signal was collected as a function of phases applied to an otherwise transform-limited pulse, and the integrated intensity plotted as a function of ϕ'' and ϕ'''. As expected, the maximum intensity occurred when ϕ'' = 0 and ϕ''' = 0 (results not shown). This experiment was then repeated, with additional quadratic and cubic dispersion (ϕ''_{add} and ϕ'''_{add}) values introduced to mimic the acquisition of chirp during SPP propagation. Results are shown in Figure 5.7. In each case, as expected, the maximum integrated intensity occurs when the applied phase is the negative of the additional introduced phase, which is denoted by the cross in each panel.

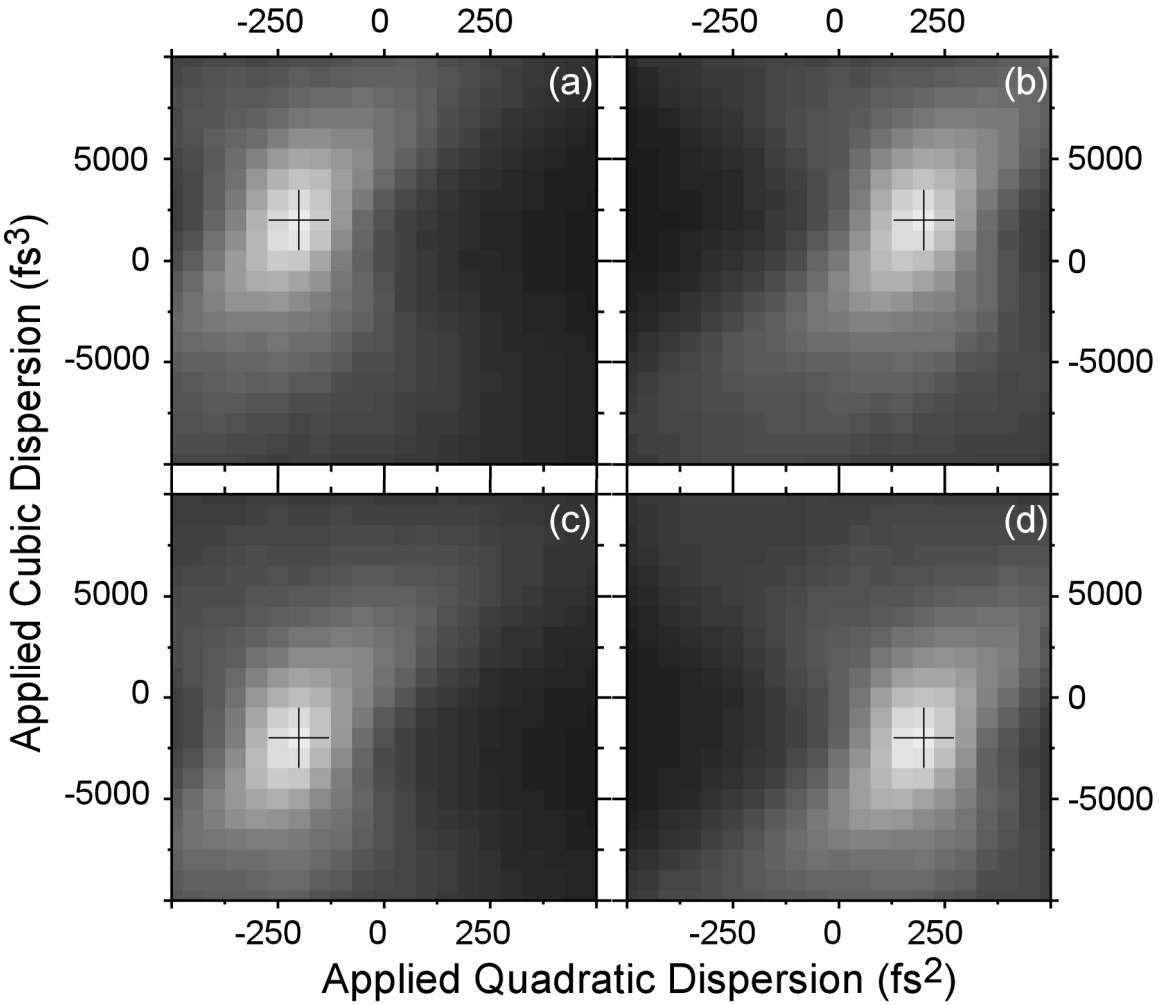

Figure 5.7. SHG Intensity as a function of applied phase. The maximum SHG signal occurs when the applied phase is exactly the negative of the introduced phase. The cross in each panel denotes the expected maximum. Panel a: results when ϕ'' = +200 fs^2 and ϕ''' = -2000 fs^3. Panel b: results when ϕ'' = -200 fs^2 and ϕ''' = -2000 fs^3. Panel c: results when ϕ'' = +200 fs^2 and ϕ''' = +2000 fs^3. Panel d: results when ϕ'' = -200 fs^2 and ϕ''' = +2000 fs^3. In each panel, the cross-hairs denote the expected maximum intensity.

Having validated the measurement method, similar experiments were then run on the silver nanoparticle sample. For each experiment, a collection of 441 images were acquired, each one with values for ϕ'' and ϕ''' defined by the grid discussed above.

Figure 5.8 summarizes the results for these measurements, after tracking the phase dependence of ~200 individual regions of localized emission, plotted as a 2-dimensional histogram of the number of discrete regions of emission for which a given ϕ''_W and ϕ'''_W value are determined.

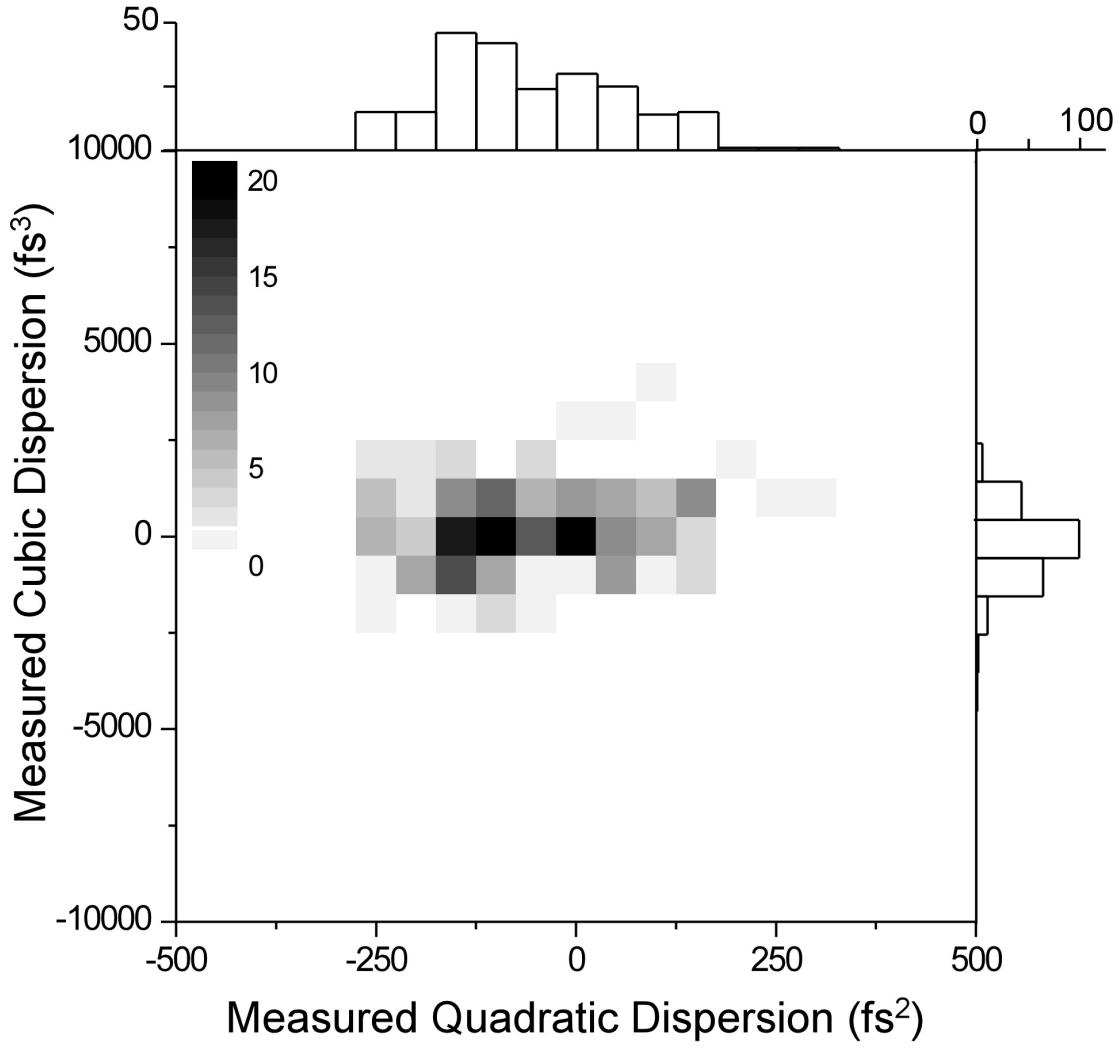

To the top and right are histograms reflecting the total number of points with a given ϕ''_w and ϕ'''_w, respectively. The bins correspond to the step size used (50 fs^2 and 1000 fs^3, respectively), which was chosen based on the estimated experimental error. It is clear that there is a wide range of both quadratic and cubic dispersions introduced by the various surface plasmon waveguides, and that this range encompasses both positive and negative values for each. The magnitude and sign of ϕ''_w and ϕ'''_w for any given regions does not exhibit any dependence on the position of the region in the sample.

5.4. Conclusion

In this chapter, the properties of the energy transport in the silver samples was explored. The two-photon-induced emission, which is observed over 40 μm from the focal spot, is consistent with the reports of tens of micrometers range of propagation of surface plasmons in metals on dielectric surfaces.[16,236] This supports the idea, discussed in Section 2.2.4, that a surface covered by silver nanoparticles can behave as a continuous thin metallic surface under certain conditions. The dynamics of SPP transport on a dielectric surface partially covered by a very thin layer of nanoparticles[87,237,238] and "islandized" metals[239-243] are extensively discussed in literature, and there is also evidence that the presence of relatively large, irregular clusters of nanoparticles is favorable for transition from a delocalized SPP mode to a localized surface plasmon.[48,238,244] While the energy can be transported as either a near-IR wave (~800 nm), or as a second-harmonic wave (~400 nm), the IR SPP wave

has been shown (as in Section 2.1.1) to have less attenuation than its corresponding SH wave.[16,23,208,245,246]

Therefore, it is proposed that silver nanoparticles with dimensions ~20-100 nm, randomly arranged, with numerous interconnections and interparticle distances shorter than the optical wavelength, deposited on a dielectric surface provide a medium for long range surface plasmon propagation. Femtosecond laser pulses with a central wavelength near 800 nm excite a surface plasmon resonance and launch a surface plasmon polariton on the very thin but interconnected layer of nanoparticles. The SPP, with a very long attenuation length, propagates from the excitation spot. The combination of constructive interference and localized surface plasmon resonance induces localized photoluminescence in the visible spectral range at distinct locations, which are observed as bright spots at distances of several tens of microns from the excitation point.

6. CONCLUSION

6.1. Comment on Reported Fluorescent Enhancement

As mentioned briefly in the introduction, this project began with an effort to use thin films of silver nanoparticles to amplify the fluorescence from a dye-doped polymer film. The enhancement of the intensity of emission by one to five orders of magnitude has been reported for a variety of dyes, including Nile Blue,[1] Rhodamine B,[1,5] Rhodamine 6G,[2,4] and others.[5-10] This enhancement in signal has also been reported for both solutions of dye with silver aggregates in the solution,[4-7] chromophoric polymers,[3] dye-doped polymers,[10] and neat dye deposited on non-continuous metallic films.[1,2,8-10]

However, when Melinda Ewald, an undergraduate in the research group, and I performed an experiment to look for enhancement of fluorescence from a rhodamine 590-doped thin film of poly(vinyl alcohol) on a thin film of silver nanoparticles, we found that the amplification observed for rhodamine-590 emission could be attributed directly to the luminescence of the silver nanoparticle clusters themselves. That is, through comparison of average peak intensity of a film of rhodamine-590, a film of silver nanoparticle clusters, and a film of the two together, a simple addition of the signal from the two former leads to the signal of the latter. Corresponding experiments done in solution, where signal from silver nanoparticles, rhodamine 590, and a solution of both was analyzed, yielded similar results: any increase in signal when comparing rhodamine and rhodamine with silver nanoparticles could be attributed to luminescence directly from the silver nanoparticles. Moreover, simply adding the emission spectra of the

individual rhodamine and silver nanoparticles together, with no scaling, results in a spectrum more similar to that of the combined solution (of the same concentrations) than simply scaling the R590 emission.

This suggests that literature in the field of metal-enhanced fluorescence (MEF) needs to be viewed with a particularly critical eye, considering the substantial spectral overlap between the emission spectra of commonly studied dyes, such as rhodamine 590 and rhodamine 6G, and the luminescence of silver. A survey of the literature indicates many papers reporting metal-enhanced fluorescence fail to report a control experiment in which it is shown that the luminescence of the silver nanoparticles is negligible compared to the reported fluorescent enhancement. However, it is worth noting the results of Lakowicz, et al.[199] who reported that metal-enhanced-fluorescence is observed at powers ~1000 times lower than those that generate luminescence from nanoparticles. This indicates that it is possible to strictly study MEF, but that care must be taken to ensure that luminescence from the nanoparticles does not affect the interpretation of the results.

6.2. Future Work

6.2.1. Gold

The surface plasmon properties of gold have been much more extensively studied than those of silver, due to the relative ease of synthesizing monodisperse solutions of nanoparticles of a well-defined size. Therefore, it may be interesting to explore the phenomena associated with surface plasmons on silver structures presented in this dissertation on gold.

In fact, preliminary studies (results not shown) were performed by Scott High, an undergraduate in the research group, using gold nanoparticles synthesized by a citrate reduction,[41] analogous to the synthesis of the silver nanoparticles that made up the bulk of the work presented in this dissertation. However, while intense, local emission was observed, remote emission was not.

There are several possible reasons for the lack of observed remote emission. First, as mentioned in Section 2.1.1, the propagation length of surface plasmons in gold is significantly smaller than that of silver. However, with 800 nm excitation, the propagation length is still potentially a detectable 10 μm. Another explanation is that the density of particles on the substrate appeared to be much higher than most of the silver samples; samples were nearly opaque. As discussed in Section 4.4.2, a correlation between the observed density of particles and lack of remote emission has been observed for silver. Other work has shown that the EM enhancement of two-photon-induced luminescence from rough gold surfaces is significantly lower than that of silver,[184] and that colloid samples of Au[193] and Ag[199] show significant differences in both the conditions required to observe luminescence and the luminescence, itself, as well. Any one, or a combination of these factors could explain the lack of remote emission observed here. However, were the right synthetic approach and found and matched to the right excitation conditions, it remains possible that similar results could be observed.

6.2.2. Correlation of Propagation and Emission with Structure

The interpretation of the results presented in this dissertation has one very significant limitation: the prepared structures were random in nature. Moreover, there

was not a way to map, at the nanoparticle level, the exact sample being irradiated. All images, whether of laser-induced emission, AFM, SEM or TEM, are “typical” samples, as far as the researchers know. However, to be able to map a sample, immediately irradiate the same area, and then map it again would allow much insight into the physics behind the behaviors observed. Changes in emission could be correlated with melting or other changes in sample, and the conditions under which maximum remote emission is observed could be further explored. A set-up that includes an AFM/NSOM coupled to an inverted microscope could potentially be used for such explorations.

A related issue is that of monitoring the actual paths of plasmon propagation. A potentially useful technique would be that presented by Ditlbacher et al.[247] In this work, 1/100th of a monolayer of Rhodamine 6G is deposited over silver structures. The metal-enhanced fluorescence from the dyes allows for optical imaging of the surface plasmon fields. A similar experiment performed on the samples here would allow insight into the paths of propagation. However, it would be most useful in conjunction with the inverted AFM/NSOM setup mentioned above, to observe what structural features optimize propagation.

6.2.3. Synthesis of Well-Defined Structures

After studying the structural conditions that lead to the observations made here, it would then be interesting to construct well-defined samples to explore how plasmon propagation could be optimized. By working with well-defined samples, it could be determined even more precisely what characteristics of the sample lead to the distant propagation and subsequent localization. This would open up doors to being able to

design waveguides to allow control over which path the energy will take as it propagates.

6.3. Potential Applications

This dissertation has shown results indicating that a laser focused to a 1 μm^2 region can cause controllable emission in localized regions around a 10^4 μm^2 area. This four orders-of-magnitude control achieved with phase-shaped and polarized pulses may have great significance in the field of electronics, in which miniaturization of chips is limited by the size of (and subsequent heat loss due to) the wires used to transport electronic information.

One of the greatest potential applications of the work presented here is in the development of plasmonic waveguides designed to bridge the realms of electronics and photonics. The development of such waveguides will allow for controlled transport of optical information in such a way that lowers the size barrier currently faced. While work has been done to develop waveguides to control plasmon propagation, there has been a consistent trade-off between control of the propagation (confinement) and the distance over which propagation can occur. At one end of the spectrum is surface plasmon propagation on infinite smooth surfaces, in which the propagation length of surface plasmons on silver can be as great as 100 μm. However, the ability to localize the energy is limited. At the other end of the spectrum are metal stripe waveguides, with very short propagation lengths, but control over the localization. Metal stripe waveguides are also limited to a linear path. Chains of nanoparticles also allow for control over the direction of propagation, and have been used to guide energy around

corners and split energy down two paths in a “tee” shape,[74] but are still limited by the distance over which propagation can take place.

The work presented in this dissertation shows that structures exist that combine the long propagation length of infinite surfaces with the localization existing for stripes and nanoparticle chains. Moreover, it has been shown here that the localization can be controlled via polarization and/or phase of the excitation laser. Particularly if extensive characterization work were performed, it seems reasonable that structures could be constructed, either though tightly controlled synthesis or more rigorous, artificial means, that would allow for multiple, controlled paths to be mapped onto a single substrate. If this were to be coupled with the work that has been done using metallic nanostructures as beam splitters,[27] and mirrors,[27, 248] a truly all-optical chip could be produced.

6.4. Conclusion

This dissertation has presented studies on the nonlinear optical properties of surface plasmons in films of silver nanoparticles. After presenting an overview of the field in Chapter 1, Chapter 2 focused on the theoretical background behind surface plasmons and their propagation as waves, as well as their ability, as a localized resonance, to enhance the electromagnetic field and contribute to surface-enhanced spectroscopies, while Chapter 3 outlined the experimental approach used in this dissertation, with a detailed discussion of the MIIPS method for compensating for the phase distortions inherent in ultrashort pulses.

After setting up the appropriate background, Chapters 4 and 5 outlined the results obtained over the past several years, in which emission from a thin film of silver nanoparticles is shown to exhibit discrete regions of localized emission more than 100

μm from the focal spot of an ultrafast laser. Chapter 4 focused on the characterization of the observed emission, identifying it as two-photon-induced fluorescence from the silver nanoparticles, with a broad, visible emission spectrum. Chapter 5 proceeded to explore both the nature of the propagation of the surface plasmons, and how the emission could be controlled. It was shown that polarization and spectral phase could be used to modulate the relative intensities of regions of emission. This chapter has concluded by discussing both future work that could extend from that presented in the dissertation, as well as discuss the potential applications of the observations here in plasmonics, where metallic structures capable of sustaining surface plasmons are used to create waveguides, with the hope of further miniaturizing electronics.

The results reported in this dissertation are the result of work at the intersection of multiple fields – most notably that of ultrafast lasers and surface plasmons -- where little other experimental work has been done. These results are particularly intriguing as the literature indicates that propagation,[15-20,62,63] localization,[45,47-51] and luminescence from silver structures[194-202] have each been observed, but not simultaneously, as reported here. It is interesting, therefore, to explore the reasons this might be the case.

One reason these observations may not have been previously made is that little research is being done using ultrafast lasers to study surface plasmons. Of the more than 18,000 results returned by a search for “surface plasmon” on the Web of Science database, only 316 included “ultrafast OR femtosecond,” and only a third of those involved silver. Furthermore, many of those papers were concerned with the study of individual nanoparticles, rather than films and extended structures. Of these systems, it

is unlikely that many would be using detection modalities that would capture wide-field images. It is only once all the components are brought together that such fascinating observations can be made.

REFERENCES

REFERENCES

1. Glass, A. M.; Liao, P. F.; Bergman, J. G.; Olson, D. H., Interaction of Metal Particles with Absorbed Dye Molecules - Absorption and Luminescence. *Optics Letters* **1980,** 5, (9), 368-370.

2. Ritchie, G.; Burstein, E., Luminescence of Dye Molecules Adsorbed at a Ag Surface. *Physical Review B* **1981,** 24, (8), 4843-4846.

3. Wenseleers, W.; Stellacci, F.; Meyer-Friedrichsen, T.; Mangel, T.; Bauer, C. A.; Pond, S. J. K.; Marder, S. R.; Perry, J. W., Five orders-of-magnitude enhancement of two-photon absorption for dyes on silver nanoparticle fractal clusters. *Journal of Physical Chemistry B* **2002,** 106, (27), 6853-6863.

4. Wang, H. Z.; Zhao, F. L.; He, Y. J.; Zheng, X. G.; Huang, X. G.; Wu, M. M., Low-threshold lasing of a Rhodamine dye solution embedded with nanoparticle fractal aggregates. *Optics Letters* **1998,** 23, (10), 777-779.

5. Gryczynski, I.; Malicka, J.; Shen, Y. B.; Gryczynski, Z.; Lakowicz, J. R., Multiphoton excitation of fluorescence near metallic particles: Enhanced and localized excitation. *Journal of Physical Chemistry B* **2002,** 106, (9), 2191-2195.

6. Zhao, J. W.; Huang, L. Q.; Wang, Y. C.; Zhu, J., Two-photon absorption-induced F-4(9/2) -> H-6(15/2) fluorescence. *Physica B-Condensed Matter* **2005,** 362, (1-4), 103-107.

7. Cohanoschi, I.; Hernandez, F. E., Surface plasmon enhancement of two- and three-photon absorption of Hoechst 33 258 dye in activated gold colloid solution. *Journal of Physical Chemistry B* **2005,** 109, (30), 14506-14512.

8. Corrigan, T. D.; Guo, S.; Phaneuf, R. J.; Szmacinski, H., Enhanced fluorescence from periodic arrays of silver nanoparticles. *Journal of Fluorescence* **2005,** 15, (5), 777-784.

9. Lukomska, J.; Gryczynski, I.; Malicka, J.; Makowiec, S.; Lakowicz, J. R.; Gryczynski, Z., Two-photon induced fluorescence of Cy5-DNA in buffer solution and on silver island films. *Biochemical and Biophysical Research Communications* **2005,** 328, (1), 78-84.

10. Neal, T. D.; Okamoto, K.; Scherer, A., Surface plasmon enhanced emission from dye doped polymer layers. *Optics Express* **2005,** 13, (14), 5522-5527.

11. Wong, V.; Ratner, M. A., Geometry dependent features of optically induced forces between silver nanoparticles. *Journal of Physical Chemistry B* **2006,** 110, (39), 19243-19253.

12. Xie, X., Single-molecule spectroscopy and dynamics at room temperature. *Acc. Chem. Res* **1996,** 29, (12), 598-606.

13. Anger, P.; Bharadwaj, P.; Novotny, L., Enhancement and quenching of single-molecule fluorescence. *Physical review letters* **2006,** 96, (11), 113002.

14. Gunn, J. M.; Ewald, M.; Dantus, M., Polarization and phase control of remote surface-plasmon-mediated two-photon-induced emission and waveguiding. *Nano Letters* **2006,** 6, (12), 2804-2809.

15. Weeber, J.; Krenn, J.; Dereux, A.; Lamprecht, B.; Lacroute, Y.; Goudonnet, J., Near-field observation of surface plasmon polariton propagation on thin metal stripes. *Physical Review B* **2001,** 64, (4), 45411.

16. Lamprecht, B.; Krenn, J.; Schider, G.; Ditlbacher, H.; Salerno, M.; Felidj, N.; Leitner, A.; Aussenegg, F.; Weeber, J., Surface plasmon propagation in microscale metal stripes. *Applied physics letters* **2001,** 79, 51.

17. Krenn, J.; Weeber, J., Surface plasmon polaritons in metal stripes and wires. *Philosophical Transactions: Mathematical, Physical and Engineering Sciences* **2004,** 362, (1817), 739-756.

18. Weeber, J.; Lacroute, Y.; Dereux, A., Optical near-field distributions of surface plasmon waveguide modes. *Physical Review B* **2003,** 68, (11), 115401.

19. Dickson, R.; Lyon, L., Unidirectional plasmon propagation in metallic nanowires. *J. Phys. Chem. B* **2000,** 104, (26), 6095-6098.

20. Laroche, T.; Girard, C., Near-field optical properties of single plasmonic nanowires. *Applied Physics Letters* **2006,** 89, (23).

21. Ozbay, E., Plasmonics: Merging photonics and electronics at nanoscale dimensions. *Science* **2006,** 311, (5758), 189-193.

22. Maier, S. A.; Atwater, H. A., Plasmonics: Localization and guiding of electromagnetic energy in metal/dielectric structures. *Journal of Applied Physics* **2005,** 98, (1), 011101.

23. Barnes, W. L.; Dereux, A.; Ebbesen, T. W., Surface plasmon subwavelength optics. *Nature* **2003,** 424, (6950), 824-830.

24. Stockman, M. I., Nanofocusing of optical energy in tapered plasmonic waveguides. *Physical Review Letters* **2004,** 93, (13), 137404.

25. Dionne, J. A.; Sweatlock, L. A.; Atwater, H. A.; Polman, A., Planar metal plasmon waveguides: frequency-dependent dispersion, propagation, localization, and loss beyond the free electron model. *Physical Review B* **2005,** 72, (7), 075405.

26. Charbonneau, R.; Berini, P.; Berolo, E.; Lisicka-Shrzek, E., Experimental observation of plasmon-polariton waves supported by a thin metal film of finite width. *Optics Letters* **2000,** 25, (11), 844-846.

27. Ditlbacher, H.; Krenn, J. R.; Schider, G.; Leitner, A.; Aussenegg, F. R., Two-dimensional optics with surface plasmon polaritons. *Appl. Phys. Lett.* **2002,** 81, (10), 1762-1764.

28. Tong, L. M.; Li, Z. P.; Zhu, T.; Xu, H. X.; Liu, Z. F., Single gold-nanoparticle-enhanced Raman scattering of individual single-walled carbon nanotubes via atomic force microscope manipulation. *Journal of Physical Chemistry C* **2008,** 112, (18), 7119-7123.

29. Chen, J. N.; Martensson, T.; Dick, K. A.; Deppert, K.; Xu, H. Q.; Samuelson, L.; Xu, H. X., Surface-enhanced Raman scattering of rhodamine 6G on nanowire arrays decorated with gold nanoparticles. *Nanotechnology* **2008,** 19, (27).

30. Liu, G. L.; Lu, Y.; Kim, J.; Doll, J. C.; Lee, L. P., Magnetic nanocrescents as controllable surface-enhanced Raman scattering nanoprobes for biomolecular imaging. *Advanced Materials* **2005,** 17, (22), 2683-+.

31. Emery, S. R.; Haskins, W. E.; Nie, S. M., Direct observation of size-dependent optical enhancement in single metal nanoparticles. *Journal of the American Chemical Society* **1998,** 120, (31), 8009-8010.

32. Schatz, G. C.; Van Duyne, R. P., Electromagnetic Mechanism of Surface-Enhanced Spectroscopy. In *Handbook of Vibrational Spectroscopy*, ed.; Chalmers, J. M.; Griffiths, P. R., 'Ed.'^'Eds.' Wiley: New York, 2002; 'Vol.' p^pp 759-774.

33. Nie, S. M.; Emery, S. R., Probing single molecules and single nanoparticles by surface-enhanced Raman scattering. *Science* **1997,** 275, (5303), 1102-1106.

34. Dieringer, J. A.; Lettan, R. B.; Scheidt, K. A.; Van Duyne, R. P., A frequency domain existence proof of single-molecule surface-enhanced Raman Spectroscopy. *Journal of the American Chemical Society* **2007,** 129, (51), 16249-16256.

35. Nie, S.; Emory, S., Probing single molecules and single nanoparticles by surface-enhanced Raman scattering. *Science* **1997,** 275, (5303), 1102.

36. Maruyama, Y.; Futamata, M., Elastic scattering and emission correlated with single-molecule SERS. *Journal of Raman Spectroscopy* **2005,** 36, (6-7), 581-592.

37. Willets, K. A.; Van Duyne, R. P., Localized surface plasmon resonance spectroscopy and sensing. *Annual Review of Physical Chemistry* **2007,** 58, 267-297.

38. McFarland, A. D.; Van Duyne, R. P., Single silver nanoparticles as real-time optical sensors with zeptomole sensitivity. *Nano Letters* **2003,** 3, (8), 1057-1062.

39. Moskovits, M., Surface-Enhanced Spectroscopy. *Reviews of Modern Physics* **1985,** 57, (3), 783-826.

40. Moskovits, M., Surface-Roughness and Enhanced Intensity of Raman-Scattering by Molecules Adsorbed on Metals. *Journal of Chemical Physics* **1978,** 69, (9), 4159-4161.

41. Lee, P. C.; Meisel, D., Adsorption and Surface-Enhanced Raman of Dyes on Silver and Gold Sols. *Journal of Physical Chemistry* **1982,** 86, (17), 3391-3395.

42. Bright, R. M.; Musick, M. D.; Natan, M. J., Preparation and characterization of Ag colloid monolayers. *Langmuir* **1998,** 14, (20), 5695-5701.

43. Kneipp, K.; Kneipp, H.; Itzkan, I.; Dasari, R.; Feld, M., Surface-enhanced non-linear Raman scattering at the single-molecule level. *Chemical Physics* **1999,** 247, (1), 155-162.

44. Leng, W.; Kelley, A., Surface-enhanced hyper-Raman spectra and enhancement factors for three SERS chromophores. SEHRS spectra on Ag films at pulse energies below 2 pJ. *J. Am. Chem. Soc* **2006,** 128, (11), 3492-3493.

45. Tsai, D.; Kovacs, J.; Wang, Z.; Moskovits, M.; Shalaev, V.; Suh, J.; Botet, R., Photon scanning tunneling microscopy images of optical excitations of fractal metal colloid clusters. *Physical review letters* **1994,** 72, (26), 4149-4152.

46. Arya, K.; Su, Z.; Birman, J., Localization of the surface plasmon polariton caused by random roughness and its role in surface-enhanced optical phenomena. *Physical review letters* **1985,** 54, (14), 1559-1562.

47. Bozhevolnyi, S. I.; Vohnsen, B.; Smolyaninov, II; Zayats, A. V., Direct Observation of Surface Polariton Localization Caused by Surface-Roughness. *Optics Communications* **1995,** 117, (5-6), 417-423.

48. Gresillon, S.; Aigouy, L.; Boccara, A. C.; Rivoal, J. C.; Quelin, X.; Desmarest, C.; Gadenne, P.; Shubin, V. A.; Sarychev, A. K.; Shalaev, V. M., Experimental observation of localized optical excitations in random metal-dielectric films. *Physical Review Letters* **1999,** 82, (22), 4520-4523.

49. Marti, O.; Bielefeldt, H.; Hecht, B.; Herminghaus, S.; Leiderer, P.; Mlynek, J., Near-field optical measurement of the surface plasmon field. *Optics Communications* **1993,** 96, (4-6), 225-228.

50. Seal, K.; Nelson, M. A.; Ying, Z. C.; Genov, D. A.; Sarychev, A. K.; Shalaev, V. M., Growth, morphology, and optical and electrical properties of semicontinuous metallic films. *Physical Review B* **2003,** 67, (3).

51. Anceau, C.; Brasselet, S.; Zyss, J.; Gadenne, P., Local second-harmonic generation enhancement on gold nanostructures probed by two-photon microscopy. *Optics Letters* **2003,** 28, (9), 713-715.

52. Xiao, J. J.; Huang, J. P.; Yu, K. W., Optical response of strongly coupled metal nanoparticles in dimer arrays. *Physical Review B* **2005,** 71, (4).

53. Shalaev, V. M.; Poliakov, E. Y.; Markel, V. A., Small-particle composites .2. Nonlinear optical properties. *Physical Review B* **1996,** 53, (5), 2437-2449.

54. Wurtz, G. A.; Im, J. S.; Gray, S. K.; Wiederrecht, G. P., Optical scattering from isolated metal nanoparticles and arrays. *Journal of Physical Chemistry B* **2003,** 107, (51), 14191-14198.

55. Jensen, T.; Kelly, L.; Lazarides, A.; Schatz, G. C., Electrodynamics of noble metal nanoparticles and nanoparticle clusters. *Journal of Cluster Science* **1999,** 10, (2), 295-317.

56. Hao, E.; Schatz, G. C., Electromagnetic fields around silver nanoparticles and dimers. *Journal of Chemical Physics* **2004,** 120, (1), 357-366.

57. Markel, V. A.; Shalaev, V. M.; Stechel, E. B.; Kim, W.; Armstrong, R. L., Small-particle composites .1. Linear optical properties. *Physical Review B* **1996,** 53, (5), 2425-2436.

58. Raether, H., *Surface Plasmons on Smooth and Rough Surfaces and on Gratings*. ed.; Springer: Berlin, 1988; 'Vol.' 111, p 136.

59. Maier, S., *Plasmonics: fundamentals and applications*. ed.; Springer Verlag: 2007; 'Vol.' p.

60. Jackson, J., Classical Electrodynamics, 3rd cd. *New York, Jhon Willey & Sons* **1999**.

61. Johnson, P.; Christy, R., Optical constants of the noble metals. *Physical Review B* **1972,** 6, (12), 4370-4379.

62. Poulton, C.; Schmidt, M.; Pearce, G.; Kakarantzas, G.; Russell, P., Numerical study of guided modes in arrays of metallic nanowires. *Optics letters* **2007,** 32, (12), 1647-1649.

63. Alu, A.; Belov, P. A.; Engheta, N., Parallel-chain optical transmission line for a low-loss ultraconfined light beam. *Physical Review B* **2009,** 80, (11).

64. Bouhelier, A.; Wiederrecht, G., Surface plasmon rainbow jets. *Optics letters* **2005,** 30, (8), 884-886.

65. Gersten, J.; Nitzan, A., Electromagnetic theory of enhanced Raman scattering by molecules adsorbed on rough surfaces. *The Journal of Chemical Physics* **1980,** 73, 3023.

66. Liao, P.; Wokaun, A., Lightning rod effect in surface enhanced Raman scattering. *The Journal of Chemical Physics* **1982,** 76, 751.

67. Mock, J. J.; Barbic, M.; Smith, D. R.; Schultz, D. A.; Schultz, S., Shape effects in plasmon resonance of individual colloidal silver nanoparticles. *Journal of Chemical Physics* **2002,** 116, (15), 6755-6759.

68. Kelly, K. L.; Coronado, E.; Zhao, L. L.; Schatz, G. C., The optical properties of metal nanoparticles: The influence of size, shape, and dielectric environment. *Journal of Physical Chemistry B* **2003,** 107, (3), 668-677.

69. Kuwata, H.; Tamaru, H.; Esumi, K.; Miyano, K., Resonant light scattering from metal nanoparticles: Practical analysis beyond Rayleigh approximation. *Applied Physics Letters* **2003,** 83, 4625.

70. Encina, E. R.; Coronado, E. A., Resonance conditions for multipole plasmon excitations in noble metal nanorods. *Journal of Physical Chemistry C* **2007,** 111, (45), 16796-16801.

71. Chu, H.; Ewe, W.; Li, E.; Vahldieck, R., Analysis of sub-wavelength light propagation through long double-chain nanowires with funnel feeding. *Materials today* **2006,** 9, 20-27.

72. Quinten, M.; Leitner, A.; Krenn, J. R.; Aussenegg, F. R., Electromagnetic energy transport via linear chains of silver nanoparticles. *Optics Letters* **1998,** 23, (17), 1331-1333.

73. Brongersma, M. L.; Hartman, J. W.; Atwater, H. A., Electromagnetic energy transfer and switching in nanoparticle chain arrays below the diffraction limit. *Physical Review B* **2000,** 62, (24), R16356-R16359.

74. Maier, S.; Brongersma, M.; Kik, P.; Meltzer, S.; Requicha, A.; Atwater, H., PlasmonicsÐA Route to Nanoscale Optical Devices*. *Adv. Mater* **2001,** 13, (19), 2.

75. Maier, S.; Kik, P.; Atwater, H.; Meltzer, S.; Harel, E.; Koel, B.; Requicha, A., Local detection of electromagnetic energy transport below the diffraction limit in metal nanoparticle plasmon waveguides. *Nature Materials* **2003,** 2, (4), 229-232.

76. Weber, W. H.; Ford, G. W., Propagation of optical excitations by dipolar interactions in metal nanoparticle chains. *Physical Review B* **2004,** 70, (12).

77. Park, S. Y.; Stroud, D., Surface-plasmon dispersion relations in chains of metallic nanoparticles: An exact quasistatic calculation. *Physical Review B* **2004,** 69, (12).

78. Citrin, D. S., Coherent excitation transport in metal-nanoparticle chains. *Nano Letters* **2004,** 4, (9), 1561-1565.

79. Citrin, D. S., Plasmon polaritons in finite-length metal-nanoparticle chains: The role of chain length unravelled. *Nano Letters* **2005,** 5, (5), 985-989.

80. Sweatlock, L. A.; Maier, S. A.; Atwater, H. A.; Penninkhof, J. J.; Polman, A., Highly confined electromagnetic fields in arrays of strongly coupled Ag nanoparticles. *Physical Review B* **2005,** 71, (23).

81. Pinchuk, A. O.; Schatz, G. C., Nanoparticle optical properties: Far- and near-field electrodynamic coupling in a chain of silver spherical nanoparticles. *Materials Science and Engineering B-Advanced Functional Solid-State Materials* **2008,** 149, (3), 251-258.

82. Zou, S. L.; Schatz, G. C., Metal nanoparticle array waveguides: Proposed structures for subwavelength devices. *Physical Review B* **2006,** 74, (12), 125111.

83. Baer, R.; Lopata, K.; Neuhauser, D., Properties of phase-coherent energy shuttling on the nanoscale. *Journal of Chemical Physics* **2007,** 126, (1).

84. Crozier, K. B.; Togan, E.; Simsek, E.; Yang, T., Experimental measurement of the dispersion relations of the surface plasmon modes of metal nanoparticle chains. *Optics Express* **2007,** 15, (26), 17482-17493.

85. Citrin, D.; Wang, Y.; Zhou, Z., Far-field optical coupling to semi-infinite metal-nanoparticle chains. *Journal of the Optical Society of America B* **2008,** 25, (6), 937-944.

86. Backes, T.; Citrin, D., Excitation of nonradiative surface-plasmon-polariton beams in nanoparticle arrays. *Physical Review B* **2008,** 78, (15), 153407.

87. Murray, W. A.; Astilean, S.; Barnes, W. L., Transition from localized surface plasmon resonance to extended surface plasmon-polariton as metallic nanoparticles merge to form a periodic hole array. *Physical Review B* **2004,** 69, (16).

88. Oates, T.; Mücklich, A., Evolution of plasmon resonances during plasma deposition of silver nanoparticles. *Nanotechnology* **2005,** 16, 2606-2611.

89. Trebino, R.; Kane, D. J., Using phase retrieval to measure the intensity and phase of ultrashort pulses - frequency-resolved optical gating. *J. Opt. Soc. Am. A* **1993,** 10, (5), 1101-1111.

90. Kane, D. J.; Trebino, R., Characterization of arbitrary femtosecond pulses using frequency-resolved optical gating. *IEEE J Quantum Elect* **1993,** 29, (2), 571-579.

91. DeLong, K. W.; Trebino, R.; Hunter, J.; White, W. E., Frequency-resolved optical gating with the use of 2nd-harmonic generation. *J. Opt. Soc. Am. B* **1994,** 11, (11), 2206-2215.

92. DeLong, K. W.; Fittinghoff, D. N.; Trebino, R.; Kohler, B.; Wilson, K., Pulse retrieval in frequency-resolved optical gating based on the method of generalized projections. *Opt. Lett.* **1994,** 19, (24), 2152-2154.

93. Taft, G.; Rundquist, A.; Murnane, M. M.; Christov, I. P.; Kapteyn, H. C.; DeLong, K. W.; Fittinghoff, D. N.; Krumbugel, M. A.; Sweetser, J. N.; Trebino, R., Measurement of 10-fs laser pulses. *IEEE J Sel Top Quant* **1996,** 2, (3), 575-585.

94. Trebino, R.; DeLong, K. W.; Fittinghoff, D. N.; Sweetser, J. N.; Krumbugel, M. A.; Richman, B. A.; Kane, D. J., Measuring ultrashort laser pulses in the time-frequency domain using frequency-resolved optical gating. *Rev. Sci. Instrum.* **1997,** 68, (9), 3277-3295.

95. Trebino, R., *Frequency-resolved optical gating : the measurement of ultrashort laser pulses*. ed.; Kluwer Academic: Boston, 2000; 'Vol.' p xvii, 425 p.

96. Iaconis, C.; Walmsley, I. A., Spectral phase interferometry for direct electric-field reconstruction of ultrashort optical pulses. *Opt. Lett.* **1998,** 23, (10), 792-794.

97. Iaconis, C.; Walmsley, I. A., Self-referencing spectral interferometry for measuring ultrashort optical pulses. *IEEE J Quantum Elect* **1999,** 35, (4), 501-509.

98. Gallmann, L.; Sutter, D. H.; Matuschek, N.; Steinmeyer, G.; Keller, U.; Iaconis, C.; Walmsley, I. A., Characterization of sub-6-fs optical pulses with spectral phase interferometry for direct electric-field reconstruction. *Opt. Lett.* **1999,** 24, (18), 1314-1316.

99. Dorrer, C.; de Beauvoir, B.; Le Blanc, C.; Ranc, S.; Rousseau, J. P.; Rousseau, P.; Chambaret, J. P., Single-shot real-time characterization of chirped-pulse amplification systems by spectral phase interferometry for direct electric-field reconstruction. *Opt. Lett.* **1999,** 24, (22), 1644-1646.

100. Dudovich, N.; Oron, D.; Silberberg, Y., Single-pulse coherently controlled nonlinear Raman spectroscopy and microscopy. *Nature* **2002,** 418, (6897), 512-514.

101. Oron, D.; Dudovich, N.; Silberberg, Y., Single-pulse phase-contrast nonlinear Raman spectroscopy. *Physical Review Letters* **2002,** 89, (27).

102. Oron, D.; Dudovich, N.; Yelin, D.; Silberberg, Y., Quantum control of coherent anti-Stokes Raman processes. *Physical Review A* **2002,** 65, (4), Art. No. 043408.

103. Li, H. W.; Harris, D. A.; Xu, B.; Wrzesinski, P. J.; Lozovoy, V. V.; Dantus, M., Coherent mode-selective Raman excitation towards standoff detection. *Optics Express* **2008,** 16, (8), 5499-5504.

104. Li, H. W.; Harris, D. A.; Xu, B.; Wrzesinski, P. J.; Lozovoy, V. V.; Dantus, M., Standoff and arms-length detection of chemicals with single-beam coherent anti-Stokes Raman scattering. *Applied Optics* **2009,** 48, B17-B22.

105. Li, H. W.; Harris, D. A.; Xu, B.; Wrzesinski, P. J.; Lozovoy, V. V.; Dantus, M., Single-Beam Coherent Anti-Stokes Raman Scattering for Standoff Detection. *Optics & Photonics News* **2008,** 19, 46.

106. Weiner, A. M., Programmable shaping of femtosecond optical pulses by use of 128-element liquid-crystal phase modulator. *IEEE J. Quantum Elect.* **1992,** 28, (4), 908-920.

107. Assion, A.; Baumert, T.; Bergt, M.; Brixner, T.; Kiefer, B.; Seyfried, V.; Strehle, M.; Gerber, G., Control of chemical reactions by feedback-optimized phase-shaped femtosecond laser pulses. *Science* **1998,** 282, (5390), 919-922.

108. Levis, R. J.; Menkir, G. M.; Rabitz, H., Selective bond dissociation and rearrangement with optimally tailored, strong-field laser pulses. *Science* **2001,** 292, 709-713.

109. Bardeen, C. J.; Yakovlev, V. V.; Squier, J. A.; Wilson, K. R.; Carpenter, S. D.; Weber, P. M., Effect of pulse shape on the efficiency of multiphoton processes: Implications for biological microscopy. *J. Biomed. Opt.* **1999,** 4, (3), 362-367.

110. Neogi, A.; Yoshida, H.; Mozume, T.; Wada, O., Enhancement of interband optical nonlinearity by manipulation of intersubband transitions in an undoped semiconductor quantum well. *Opt. Commun.* **1999,** 159, (4-6), 225-229.

111. Ahn, J.; Weinacht, T. C.; Bucksbaum, P. H., Information storage and retrieval through quantum phase. *Science* **2000,** 287, 463-465.

112. Lozovoy, V. V.; Dantus, M., Photon echo pulse sequences with femtosecond shaped laser pulses as a vehicle for molecule-based quantum computation. *Chem. Phys. Lett.* **2002,** 351, (3-4), 213-221.

113. Yasuno, Y.; Nakama, M.; Sutoh, Y.; Itoh, M.; Mori, M.; Yatagai, T., Optical coherence tomography by spectral interferometric joint transform correlator. *Opt. Commun.* **2000,** 186, (1-3), 51-56.

114. Judson, R. S.; Rabitz, H., Teaching lasers to control molecules. *Phys. Rev. Lett.* **1992,** 68, (10), 1500-1503.

115. Bardeen, C. J.; Yakovlev, V. V.; Wilson, K. R.; Carpenter, S. D.; Weber, P. M.; Warren, W. S., Feedback quantum control of molecular electronic population transfer. *Chem. Phys. Lett.* **1997,** 280, (1-2), 151-158.

116. Meshulach, D.; Yelin, D.; Silberberg, Y., Adaptive ultrashort pulse compression and shaping. *Opt. Commun.* **1997,** 138, (4-6), 345-348.

117. Yelin, D.; Meshulach, D.; Silberberg, Y., Adaptive femtosecond pulse compression. *Opt. Lett.* **1997,** 22, (23), 1793-1795.

118. Meshulach, D.; Yelin, D.; Silberberg, Y., Adaptive real-time femtosecond pulse shaping. *J. Opt. Soc. Am. B* **1998,** 15, (5), 1615-1619.

119. Baumert, T.; Brixner, T.; Seyfried, V.; Strehle, M.; Gerber, G., Femtosecond pulse shaping by an evolutionary algorithm with feedback. *Appl. Phys. B- Lasers and Optics* **1997,** 65, (6), 779-782.

120. Brixner, T.; Strehle, M.; Gerber, G., Feedback-controlled optimization of amplified femtosecond laser pulses. *Appl. Phys. B- Lasers and Optics* **1999,** 68, (2), 281-284.

121. Brixner, T.; Oehrlein, A.; Strehle, M.; Gerber, G., Feedback-controlled femtosecond pulse shaping. *Appl. Phys. B- Lasers and Optics* **2000,** 70, S119-S124.

122. Efimov, A.; Moores, M. D.; Beach, N. M.; Krause, J. L.; Reitze, D. H., Adaptive control of pulse phase in a chirped-pulse amplifier. *Opt. Lett.* **1998,** 23, (24), 1915-1917.

123. Efimov, A.; Reitze, D. H., Programmable dispersion compensation and pulse shaping in a 26-fs chirped-pulse amplifier. *Opt. Lett.* **1998,** 23, (20), 1612-1614.

124. Efimov, A.; Moores, M. D.; Mei, B.; Krause, J. L.; Siders, C. W.; Reitze, D. H., Minimization of dispersion in an ultrafast chirped pulse amplifier using adaptive learning. *Appl. Phys. B- Lasers and Optics* **2000,** 70, S133-S141.

125. Rundquist, A.; Efimov, A.; Reitze, D. H., Pulse shaping with the Gerchberg-Saxton algorithm. *J. Opt. Soc. Am. B* **2002,** 19, (10), 2468-2478.

126. Ohno, K.; Tanabe, T.; Kannari, F., Adaptive pulse shaping of phase and amplitude of an amplified femtosecond pulse laser by direct reference to frequency-resolved optical gating traces. *J. Opt. Soc. Am. B* **2002,** 19, (11), 2781-2790.

127. Tanabe, T.; Ohno, K.; Okamoto, T.; Yamanaka, M.; Kannari, F., Feedback control for accurate shaping of ultrashort optical pulses prior to chirped pulse amplification. *Jpn. J. Appl. Phys. 1* **2004,** 43, (4A), 1366-1375.

128. Zeek, E.; Maginnis, K.; Backus, S.; Russek, U.; Murnane, M.; Mourou, G.; Kapteyn, H.; Vdovin, G., Pulse compression by use of deformable mirrors. *Opt. Lett.* **1999,** 24, (7), 493-495.

129. Zeek, E.; Bartels, R.; Murnane, M. M.; Kapteyn, H. C.; Backus, S.; Vdovin, G., Adaptive pulse compression for transform-limited 15-fs high-energy pulse generation. *Opt. Lett.* **2000,** 25, (8), 587-589.

130. Zeidler, D.; Hornung, T.; Proch, D.; Motzkus, M., Adaptive compression of tunable pulses from a non-collinear-type OPA to below 16 fs by feedback-controlled pulse shaping. *Appl. Phys. B- Lasers and Optics* **2000,** 70, S125-S131.

131. Armstrong, M. R.; Plachta, P.; Ponomarev, E. A.; Miller, R. J. D., Versatile 7-fs optical parametric pulse generation and compression by use of adaptive optics. *Opt. Lett.* **2001,** 26, (15), 1152-1154.

132. Armstrong, M.; Plachta, P.; Ponomarev, E. A.; Ogilvie, J. P.; Nagy, A. M.; Miller, R. J. D., Versatile seven-femtosecond pulse compressor of parametrically amplified pulses using adaptive optics: studies of the primary events in protein dynamics. *Appl. Phys. B- Lasers and Optics* **2002,** 74, S127-S132.

133. Baltuska, A.; Fuji, T.; Kobayashi, T., Visible pulse compression to 4 fs by optical parametric amplification and programmable dispersion control. *Opt. Lett.* **2002,** 27, (5), 306-308.

134. Baltuska, A.; Kobayashi, T., Adaptive shaping of two-cycle visible pulses using a flexible mirror. *Appl. Phys. B- Lasers and Optics* **2002,** 75, (4-5), 427-443.

135. Legare, F. L.; Fraser, J. M.; Villeneuve, D. M.; Corkum, P. B., Adaptive compression of intense 250-nm-bandwidth laser pulses. *Appl. Phys. B- Lasers and Optics* **2002,** 74, S279-S282.

136. Baum, P.; Lochbrunner, S.; Gallmann, L.; Steinmeyer, G.; Keller, U.; Riedle, E., Real-time characterization and optimal phase control of tunable visible pulses with a flexible compressor. *Appl. Phys. B- Lasers and Optics* **2002,** 74, S219-S224.

137. Gallmann, L.; Steinmeyer, G.; Imeshev, G.; Meyn, J. P.; Fejer, M. M.; Keller, U., Sub-6-fs blue pulses generated by quasi-phase-matching second-harmonic generation pulse compression. *Appl. Phys. B- Lasers and Optics* **2002,** 74, S237-S243.

138. Siegner, U.; Haiml, M.; Kunde, J.; Keller, U., Adaptive pulse compression by two-photon absorption in semiconductors. *Opt. Lett.* **2002,** 27, (5), 315-317.

139. Monmayrant, A.; Joffre, M.; Oksenhendler, T.; Herzog, R.; Kaplan, D.; Tournois, P., Time-domain interferometry for direct electric-field reconstruction by use of an acousto-optic programmable filter and a two-photon detector. *Opt. Lett.* **2003,** 28, (4), 278-280.

140. Broers, B.; Vandenheuvell, H. B. V.; Noordam, L. D., Large interference effects of small chirp observed in 2-photon absorption. *Opt. Commun.* **1992,** 91, (1-2), 57-61.

141. Walowicz, K. A.; Pastirk, I.; Lozovoy, V. V.; Dantus, M., Multiphoton intrapulse interference. 1. Control of multiphoton processes in condensed phases. *J. Phys. Chem. A* **2002,** 106, (41), 9369-9373.

142. Lozovoy, V. V.; Pastirk, I.; Walowicz, K. A.; Dantus, M., Multiphoton intrapulse interference. II. Control of two- and three-photon laser induced fluorescence with shaped pulses. *J. Chem. Phys.* **2003,** 118, (7), 3187-3196.

143. Hacker, M.; Netz, R.; Roth, M.; Stobrawa, G.; Feurer, T.; Sauerbrey, R., Frequency doubling of phase-modulated, ultrashort laser pulses. *Appl. Phys. B-Lasers O* **2001,** 73, (3), 273-277.

144. Dela Cruz, J. M.; Pastirk, I.; Lozovoy, V. V.; Walowicz, K. A.; Dantus, M., Multiphoton intrapulse interference 3: Probing microscopic chemical environments. *J. Phys. Chem. A* **2004,** 108, (1), 53-58.

145. Pastirk, I.; Dela Cruz, J. M.; Walowicz, K. A.; Lozovoy, V. V.; Dantus, M., Selective two-photon microscopy with shaped femtosecond pulses. *Opt. Express* **2003,** 11, (14), 1695-1701.

146. Xi, P.; Andegeko, Y.; Pestov, D.; Lovozoy, V. V.; Dantus, M., Two-photon imaging using adaptive phase compensated ultrashort laser pulses. *Journal of Biomedical Optics* **2009,** 14, (1), 014002.

147. Xi, P.; Andegeko, Y.; Weisel, L. R.; Lozovoy, V. V.; Dantus, M., Greater signal, increased depth, and less photobleaching in two-photon microscopy with 10 fs pulses. *Optics Communications* **2008,** 281, (7), 1841-1849.

148. Dela Cruz, J. M.; Pastirk, I.; Comstock, M.; Dantus, M., Multiphoton intrapulse interference 8. Coherent control through scattering tissue. *Opt. Express* **2004,** 12, (17), 4144-4149.

149. Dela Cruz, J. M.; Pastirk, I.; Comstock, M.; Lozovoy, V. V.; Dantus, M., Use of coherent control methods through scattering biological tissue to achieve functional imaging. *P. Natl. Acad. Sci. USA* **2005,** 101, (49), 16996-17001.

150. Pastirk, I.; Kangas, M.; Dantus, M., Multidimensional analytical method based on binary phase shaping of femtosecond pulses. *J. Phys. Chem. A* **2005,** 109, 2413-2416.

151. Xu, B. W.; Coello, Y.; Nogueira, G. T.; Cruz, F. C.; Dantus, M., Asynchronous encrypted information transmission with sub-6 fs laser system at 2.12 GHz repetition rate. *Optics Express* **2008,** 16, (19), 15109-15114.

152. Weiner, A. M., Femtosecond pulse shaping using spatial light modulators. *Rev. Sci. Instrum.* **2000,** 71, (5), 1929-1960.

153. Xu, B.; Gunn, J.; Cruz, J.; Lozovoy, V.; Dantus, M., Quantitative investigation of the multiphoton intrapulse interference phase scan method for simultaneous phase measurement and compensation of femtosecond laser pulses. *Journal of the Optical Society of America B* **2006,** 23, (4), 750-759.

154. Baltuska, A.; Pshenichnikov, M. S.; Wiersma, D. A., Amplitude and phase characterization of 4.5-fs pulses by frequency-resolved optical gating. *Opt. Lett.* **1998,** 23, (18), 1474-1476.

155. Baltuska, A.; Pshenichnikov, M. S.; Wiersma, D. A., Second-harmonic generation frequency-resolved optical gating in the single-cycle regime. *IEEE J. Quantum Elect.* **1999,** 35, (4), 459-478.

156. Gallmann, L.; Sutter, D. H.; Matuschek, N.; Steinmeyer, G.; Keller, U., Techniques for the characterization of sub-10-fs optical pulses: a comparison. *Appl. Phys. B- Lasers O.* **2000,** 70, (Suppl.), S67-S75.

157. Schlup, P.; Bartels, R. A., Impact of Measurement Noise in Tomographic Ultrafast Retrieval of Transverse Light ${mmb E} $-Fields (TURTLE) Ultrashort Polarization Characterization. *Photonics Journal, IEEE* **2009,** 1, (2), 163-171.

158. Diddams, S.; Diels, J. C., Dispersion measurements with white-light interferometry. *J. Opt. Soc. Am. B* **1996,** 13, (6), 1120-1129.

159. Malitson, I. H., Interspecimen comparison of the refractive index of fused silica. *J. Opt. Soc. Am.* **1965,** 55, (10), 1205-1209.

160. OharaCorp. Optical glass catalog data. http://www.oharacorp.com/swf/catalog.htm (May 2,2005),

161. Jasapara, J.; Rudolph, W., Characterization of sub-10-fs pulse focusing with high-numerical-aperture microscope objectives. *Opt. Lett.* **1999,** 24, (11), 777-779.

162. Amat-Roldan, I.; Cormack, I. G.; Loza-Alvarez, P.; Artigas, D., Starch-based second-harmonic-generated collinear frequency-resolved optical gating pulse characterization at the focal plane of a high-numerical-aperture lens. *Opt. Lett.* **2004,** 29, (19), 2282-2284.

163. Fittinghoff, D. N.; Millard, A. C.; Squier, J. A.; Muller, M., Frequency-resolved optical gating measurement of ultrashort pulses passing through a high numerical aperture objective. *IEEE J. Quantum Elect.* **1999,** 35, (4), 479-486.

164. Muller, M.; Squier, J.; Wolleschensky, R.; Simon, U.; Brakenhoff, G. J., Dispersion pre-compensation of 15 femtosecond optical pulses for high-numerical-aperture objectives. *J. Microsc-Oxford* **1998,** 191, 141-150.

165. Fittinghoff, D. N.; Squier, J. A.; Barty, C. P. J.; Sweetser, J. N.; Trebino, R.; Muller, M., Collinear type II second-harmonic-generation frequency-resolved optical gating for use with high-numerical-aperture objectives. *Opt. Lett.* **1998,** 23, (13), 1046-1048.

166. Gunn, J. M.; High, S. H.; Lozovoy, V. V.; Dantus, M., Measurement and Control of Ultrashort Optical Pulse Propagation in Metal Nanoparticle-Covered Dielectric Surfaces. *Journal of Physical Chemistry C* **2010,** 114, (29), 12375-12381.

167. Turkevich, J.; Stevenson, P. C.; Hillier, J., A Study of the Nucleation and Growth Processes in the Synthesis of Colloidal Gold. *Discuss. Faraday Soc.* **1951**, (11), 55-&.

168. Smith, S. L.; Nissamudeen, K. M.; Philip, D.; Gopchandran, K. G., Studies on surface plasmon resonance and photoluminescence of silver nanoparticles. *Spectrochimica Acta Part a-Molecular and Biomolecular Spectroscopy* **2008,** 71, (1), 186-190.

169. Kim, W.; Safonov, V. P.; Shalaev, V. M.; Armstrong, R. L., Fractals in microcavities: Giant coupled, multiplicative enhancement of optical responses. *Physical Review Letters* **1999,** 82, (24), 4811-4814.

170. Hao, E.; Schatz, G. C.; Hupp, J. T., Synthesis and optical properties of anisotropic metal nanoparticles. *Journal of Fluorescence* **2004,** 14, (4), 331-341.

171. Zhai, X.; Efrima, S., Reduction of Silver Ions to a Colloid by Eriochrome Black T. *J. Phys. Chem* **1996,** 100, (5), 1779-1785.

172. Jin, R. C.; Cao, Y. C.; Hao, E. C.; Metraux, G. S.; Schatz, G. C.; Mirkin, C. A., Controlling anisotropic nanoparticle growth through plasmon excitation. *Nature* **2003,** 425, (6957), 487-490.

173. Jin, R.; Cao, Y.; Mirkin, C.; Kelly, K.; Schatz, G.; Zheng, J., Photoinduced conversion of silver nanospheres to nanoprisms. *Science* **2001,** 294, (5548), 1901.

174. Link, S.; Burda, C.; Mohamed, M. B.; Nikoobakht, B.; El-Sayed, M. A., Laser photothermal melting and fragmentation of gold nanorods: Energy and laser pulse-width dependence. *Journal of Physical Chemistry A* **1999,** 103, (9), 1165-1170.

175. Link, S.; Burda, C.; Nikoobakht, B.; El-Sayed, M., Laser-induced shape changes of colloidal gold nanorods using femtosecond and nanosecond laser pulses. *J. Phys. Chem. B* **2000,** 104, (26), 6152-6163.

176. Wenzel, T.; Bosbach, J.; Goldmann, A.; Stietz, F.; Trager, F., Shaping nanoparticles and their optical spectra with photons. *Applied Physics B-Lasers and Optics* **1999,** 69, (5-6), 513-517.

177. Link, S.; Burda, C.; Nikoobakht, B.; El-Sayed, M. A., How long does it take to melt a gold nanorod? A femtosecond pump-probe absorption spectroscopic study. *Chemical Physics Letters* **1999,** 315, (1-2), 12-18.

178. Link, S.; El-Sayed, M., Spectroscopic determination of the melting energy of a gold nanorod. *The Journal of Chemical Physics* **2001,** 114, 2362.

179. Lin, H. Y.; Chen, Y. F., Giant enhancement of luminescence induced by second-harmonic surface plasmon resonance. *Applied Physics Letters* **2006,** 88, (10).

180. Chen, C.; De Castro, A.; Shen, Y., Surface-enhanced second-harmonic generation. *Physical Review Letters* **1981,** 46, (2), 145-148.

181. Bozhevolnyi, S. I.; Pedersen, K., Second harmonic generation due to surface plasmon localization. *Surface Science* **1997,** 377, (1-3), 384-387.

182. Stockman, M. I., Giant fluctuations of second harmonic generation on nanostructured surfaces. *Chemical Physics* **2005,** 318, (1-2), 156-162.

183. Poliakov, E. Y.; Markel, V. A.; Shalaev, V. M.; Botet, R., Nonlinear optical phenomena on rough surfaces of metal thin films. *Physical Review B* **1998,** 57, (23), 14901-14913.

184. Apell, P.; Monreal, R.; Lundqvist, S., Photoluminescence of noble metals. *Physica Scripta* **1988,** 38, 174-179.

185. Varnavski, O.; Goodson III, T.; Mohamed, M.; El-Sayed, M., Femtosecond excitation dynamics in gold nanospheres and nanorods. *Physical Review B* **2005,** 72, (23), 235405.

186. Mooradian, A., Photoluminescence of metals. *Physical Review Letters* **1969,** 22, (5), 185-187.

187. Huang, T.; Murray, R., Visible luminescence of water-soluble monolayer-protected gold clusters. *J. Phys. Chem. B* **2001,** 105, (50), 12498-12502.

188. Zheng, J.; Petty, J.; Dickson, R., High quantum yield blue emission from water-soluble Au8 nanodots. *J. Am. Chem. Soc* **2003,** 125, (26), 7780-7781.

189. Bigioni, T.; Whetten, R.; Dag, O., ARTICLES-PHYSICAL CHEMISTRY OF MATERIALS: FROM NANOPARTICLES TO MACROMOLECULES-Near-Infrared Luminescence from Small Gold Nanocrystals. *Journal of Physical Chemistry B-Condensed Phase* **2000,** 104, (30), 6983-6986.

190. Wang, G.; Huang, T.; Murray, R.; Menard, L.; Nuzzo, R., Near-IR luminescence of monolayer-protected metal clusters. *J. Am. Chem. Soc* **2005,** 127, (3), 812-813.

191. Varnavski, O.; Mohamed, M.; El-Sayed, M.; Goodson, T., Relative enhancement of ultrafast emission in gold nanorods. *Journal of Physical Chemistry B* **2003,** 107, (14), 3101-3104.

192. Prodi, L.; Battistini, G.; Dolci, L.; Montalti, M.; Zaccheroni, N., Luminescence of Gold Nanoparticles. *Frontiers in Surface Nanophotonics* **2007**, 99-128.

193. Geddes, C.; Parfenov, A.; Gryczynski, I.; Lakowicz, J., Luminescent blinking of gold nanoparticles. *Chemical Physics Letters* **2003,** 380, (3-4), 269-272.

194. Zheng, J.; Dickson, R., Individual water-soluble dendrimer-encapsulated silver nanodot fluorescence. *J. Am. Chem. Soc* **2002,** 124, (47), 13982-13983.

195. Mihalcea, C.; Buchel, D.; Atoda, N.; Tominaga, J., Intrinsic fluorescence and quenching effects in photoactivated reactively sputtered silver oxide layers. *J. Am. Chem. Soc* **2001,** 123, (29), 7172-7173.

196. Peyser, L. A.; Vinson, A. E.; Bartko, A. P.; Dickson, R. M., Photoactivated fluorescence from individual silver nanoclusters. *Science* **2001,** 291, (5501), 103-106.

197. Peyser, L. A.; Lee, T. H.; Dickson, R. M., Mechanism of Ag-n nanocluster photoproduction from silver oxide films. *Journal of Physical Chemistry B* **2002,** 106, (32), 7725-7728.

198. Gleitsmann, T.; Stegemann, B.; Bernhardt, T. M., Femtosecond-laser-activated fluorescence from silver oxide nanoparticles. *Applied Physics Letters* **2004,** 84, (20), 4050-4052.

199. Geddes, C.; Parfenov, A.; Gryczynski, I.; Lakowicz, J., Luminescent blinking from silver nanostructures. *J. Phys. Chem. B* **2003,** 107, (37), 9989-9993.

200. Andersen, P. C.; Jacobson, M. L.; Rowlen, K. L., Flashy silver nanoparticles. *Journal of Physical Chemistry B* **2004,** 108, (7), 2148-2153.

201. Zhang, A. P.; Zhang, J. Z.; Fang, Y., Photoluminescence from colloidal silver nanoparticles. *Journal of Luminescence* **2008,** 128, (10), 1635-1640.

202. Stranik, O.; Iacopino, D.; Nooney, R.; McDonagh, C.; MacCraith, B. D., Optical Properties of Micro-patterned Silver Nanoparticle Substrates. *Journal of Fluorescence* 20, (1), 215-223.

203. Kneipp, K.; Wang, Y.; Kneipp, H.; Perelman, L. T.; Itzkan, I.; Dasari, R.; Feld, M. S., Single molecule detection using surface-enhanced Raman scattering (SERS). *Physical Review Letters* **1997,** 78, (9), 1667-1670.

204. Xu, H.; Bjerneld, E.; Käll, M.; Börjesson, L., Spectroscopy of single hemoglobin molecules by surface enhanced Raman scattering. *Physical review letters* **1999,** 83, (21), 4357-4360.

205. Eliel, E.; Van Der Ham, E.; Vrehen, Q., Enhancing the yield in surface sum-frequency generation by the use of surface polaritons. *Applied Physics B: Lasers and Optics* **1999,** 68, (3), 349-353.

206. Michaels, A.; Jiang, J.; Brus, L., Ag nanocrystal junctions as the site for surface-enhanced Raman scattering of single rhodamine 6G molecules. *J. Phys. Chem. B* **2000,** 104, (50), 11965-11971.

207. Johnson, R. C.; Li, J. T.; Hupp, J. T.; Schatz, G. C., Hyper-Rayleigh scattering studies of silver, copper, and platinum nanoparticle suspensions. *Chemical Physics Letters* **2002,** 356, (5-6), 534-540.

208. Barnes, W., Surface plasmon-polariton length scales: a route to sub-wavelength optics. *J. Opt. A: Pure Appl. Opt* **2006,** 8, S87-S93.

209. Boyd, G. T.; Yu, Z. H.; Shen, Y. R., Photoinduced luminescence from the noble metals and its enhancement on roughened surfaces. *Physical Review B* **1986,** 33, (12), 7923 LP - 7936.

210. Lamprecht, B.; Krenn, J. R.; Leitner, A.; Aussenegg, F. R., Resonant and off-resonant light-driven plasmons in metal nanoparticles studied by femtosecond-resolution third-harmonic generation. *Physical Review Letters* **1999,** 83, (21), 4421-4424.

211. Bouhelier, A.; Beversluis, M. R.; Novotny, L., Characterization of nanoplasmonic structures by locally excited photoluminescence. *Applied Physics Letters* **2003,** 83, (24), 5041-5043.

212. Schuck, P.; Fromm, D.; Sundaramurthy, A.; Kino, G.; Moerner, W., Improving the Mismatch between Light and Nanoscale Objects with Gold Bowtie Nanoantennas. *Physical Review Letters* **2005,** 94, (1), 17402.

213. Bouhelier, A.; Bachelot, R.; Lerondel, G.; Kostcheev, S.; Royer, P.; Wiederrecht, G. P., Surface plasmon characteristics of tunable photoluminescence in single gold nanorods. *Physical Review Letters* **2005,** 95, (26), 267405.

214. Wang, H.; Huff, T.; Zweifel, D.; He, W.; Low, P.; Wei, A.; Cheng, J., In vitro and in vivo two-photon luminescence imaging of single gold nanorods. *Proceedings of the National Academy of Sciences of the United States of America* **2005,** 102, (44), 15752.

215. Imura, K.; Nagahara, T.; Okamoto, H., Near-field two-photon-induced photoluminescence from single gold nanorods and imaging of plasmon modes. *Journal of Physical Chemistry B* **2005,** 109, (27), 13214-13220.

216. Ueno, K.; Juodkazis, S.; Mizeikis, V.; Sasaki, K.; Misawa, H., Clusters of closely spaced gold nanoparticles as a source of two-photon photoluminescence at visible wavelengths. *Advanced Materials* **2008,** 20, (1), 26-26.

217. Bouhelier, A.; Beversluis, M.; Novotny, L., Characterization of nanoplasmonic structures by locally excited photoluminescence. *Applied Physics Letters* **2003,** 83, 5041.

218. Imura, K.; Nagahara, T.; Okamoto, H., Plasmon mode imaging of single gold nanorods. *Journal of the American Chemical Society* **2004,** 126, (40), 12730.

219. Zolotavin, P.; Permenova, E.; Sarkisov, O.; Nadtochenko, V.; Azouani, R.; Portes, P.; Chhor, K.; Kanaev, A., Two-photon luminescence enhancement of silver nanoclusters photodeposited onto mesoporous TiO2 film. *Chemical Physics Letters* **2008,** 457, (4-6), 342-346.

220. Kempa, T.; Farrer, R. A.; Giersig, M.; Fourkas, J. T., Photochemical synthesis and multiphoton luminescence of monodisperse silver nanocrystals. *Plasmonics* **2006,** 1, 45-51.

221. Itoh, T.; Ozaki, Y.; Yoshikawa, H.; Ihama, T.; Masuhara, H., Hyper-Rayleigh scattering and hyper-Raman scattering of dye-adsorbed silver nanoparticles induced by a focused continuous-wave near-infrared laser. *Applied Physics Letters* **2006,** 88, 084102.

222. Shalaev, V. M.; Botet, R.; Mercer, J.; Stechel, E. B., Optical properties of self-affine thin films. *Physical Review B* **1996,** 54, (11), 8235-8242.

223. Bakker, R. M.; Boltasseva, A.; Liu, Z. T.; Pedersen, R. H.; Gresillon, S.; Kildishev, A. V.; Drachev, V. P.; Shalaev, V. M., Near-field excitation of nanoantenna resonance. *Optics Express* **2007,** 15, (21), 13682-13688.

224. Zou, S. L.; Janel, N.; Schatz, G. C., Silver nanoparticle array structures that produce remarkably narrow plasmon lineshapes. *Journal of Chemical Physics* **2004,** 120, (23), 10871-10875.

225. Aizpurua, J.; Bryant, G. W.; Richter, L. J.; de Abajo, F. J. G.; Kelley, B. K.; Mallouk, T., Optical properties of coupled metallic nanorods for field-enhanced spectroscopy. *Physical Review B* **2005,** 71, (23).

226. von Vacano, B.; Buckup, T.; Motzkus, M., Shaper-assisted collinear SPIDER: fast and simple broadband pulse compression in nonlinear microscopy. *Journal of the Optical Society of America B-Optical Physics* **2007,** 24, (5), 1091-1100.

227. Galler, A.; Feurer, T., Pulse shaper assisted short laser pulse characterization. *Applied Physics B-Lasers and Optics* **2008,** 90, (3-4), 427-430.

228. Roberti, T.; Smith, B.; Zhang, J., Ultrafast electron dynamics at the liquid–metal interface: Femtosecond studies using surface plasmons in aqueous silver colloid. *The Journal of Chemical Physics* **1995,** 102, 3860.

229. Klar, T.; Perner, M.; Grosse, S.; von Plessen, G.; Spirkl, W.; Feldmann, J., Surface-plasmon resonances in single metallic nanoparticles. *Physical Review Letters* **1998,** 80, (19), 4249-4252.

230. Lehmann, J.; Merschdorf, M.; Pfeiffer, W.; Thon, A.; Voll, S.; Gerber, G., Surface plasmon dynamics in silver nanoparticles studied by femtosecond time-resolved photoemission. *Physical Review Letters* **2000,** 85, (14), 2921-2924.

231. Kubo, A.; Onda, K.; Petek, H.; Sun, Z. J.; Jung, Y. S.; Kim, H. K., Femtosecond imaging of surface plasmon dynamics in a nanostructured silver film. *Nano Letters* **2005,** 5, (6), 1123-1127.

232. Aeschlimann, M.; Bauer, M.; Bayer, D.; Brixner, T.; de Abajo, F. J.; Pfeiffer, W.; Rohmer, M.; Spindler, C.; Steeb, F., Adaptive subwavelength control of nano-optical fields. *Nature* **2007,** 446, (7133), 301-304.

233. Fecher, G. H.; Schmidt, O.; Hwu, Y.; Schonhense, G., Multiphoton photoemission electron microscopy using femtosecond laser radiation. *Journal of Electron Spectroscopy and Related Phenomena* **2002,** 126, (1-3), 77-87.

234. Comstock, M.; Lozovoy, V. V.; Pastirk, I.; Dantus, M., Multiphoton intrapulse interference 6; binary phase shaping. *Optics Express* **2004,** 12, (6), 1061-1066.

235. Lozovoy, V. V.; Dantus, M., Coherent control in femtochemistry. *Chemphyschem* **2005,** 6, (10), 1970-2000.

236. Craig, A.; Olson, G.; Sarid, D., Experimental observation of the long-range surface-plasmon polariton. *Optics letters* **1983,** 8, (7), 380-382.

237. Collier, C.; Saykally, R.; Shiang, J.; Henrichs, S.; Heath, J., Reversible tuning of silver quantum dot monolayers through the metal-insulator transition. *Science* **1997,** 277, (5334), 1978.

238. Zayats, A.; Smolyaninov, I.; Maradudin, A., Nano-optics of surface plasmon polaritons. *Physics reports* **2005,** 408, (3-4), 131-314.

239. Yang, F.; Sambles, J.; Bradberry, G., Long-range surface modes supported by thin films. *Physical Review B* **1991,** 44, (11), 5855-5872.

240. Wu, Z.; Arakawa, E.; Inagaki, T.; Thundat, T.; Schowalter, L., Experimental observations of a long-range surface mode in metal island films. *Physical Review B* **1994,** 49, (11), 7782-7785.

241. Takabayashi, M.; Haraguchi, M.; Fukui, M., Propagation length of long-range surface optic waves in islandized silver films. *Journal of Modern Optics* **1997,** 44, (1), 119-125.

242. Salomon, L.; Bassou, G.; Aourag, H.; Dufour, J.; de Fornel, F.; Carcenac, F.; Zayats, A., Local excitation of surface plasmon polaritons at discontinuities of a metal film: Theoretical analysis and optical near-field measurements. *Physical Review B* **2002,** 65, (12), 125409.

243. Berini, P.; Charbonneau, R.; Lahoud, N.; Mattiussi, G., Characterization of long-range surface-plasmon-polariton waveguides. *Journal of Applied Physics* **2005,** 98, 043109.

244. Jiang, J.; Bosnick, K.; Maillard, M.; Brus, L., Single molecule Raman spectroscopy at the junctions of large Ag nanocrystals. *J. Phys. Chem. B* **2003,** 107, (37), 9964-9972.

245. Burke, J.; Stegeman, G.; Tamir, T., Surface-polariton-like waves guided by thin, lossy metal films. *Physical Review B* **1986,** 33, (8), 5186-5201.

246. Maier, S. A.; Atwater, H. A., Plasmonics: Localization and guiding of electromagnetic energy in metal/dielectric structures. *Journal of Applied Physics* **2005,** 98, (1).

247. Ditlbacher, H.; Krenn, J. R.; Felidj, N.; Lamprecht, B.; Schider, G.; Salerno, M.; Leitner, A.; Aussenegg, F. R., Fluorescence imaging of surface plasmon fields. *Applied Physics Letters* **2002,** 80, (3), 404-406.

248. Bozhevolnyi, S.; Pudonin, F., Two-dimensional micro-optics of surface plasmons. *Physical review letters* **1997,** 78, (14), 2823-2826.